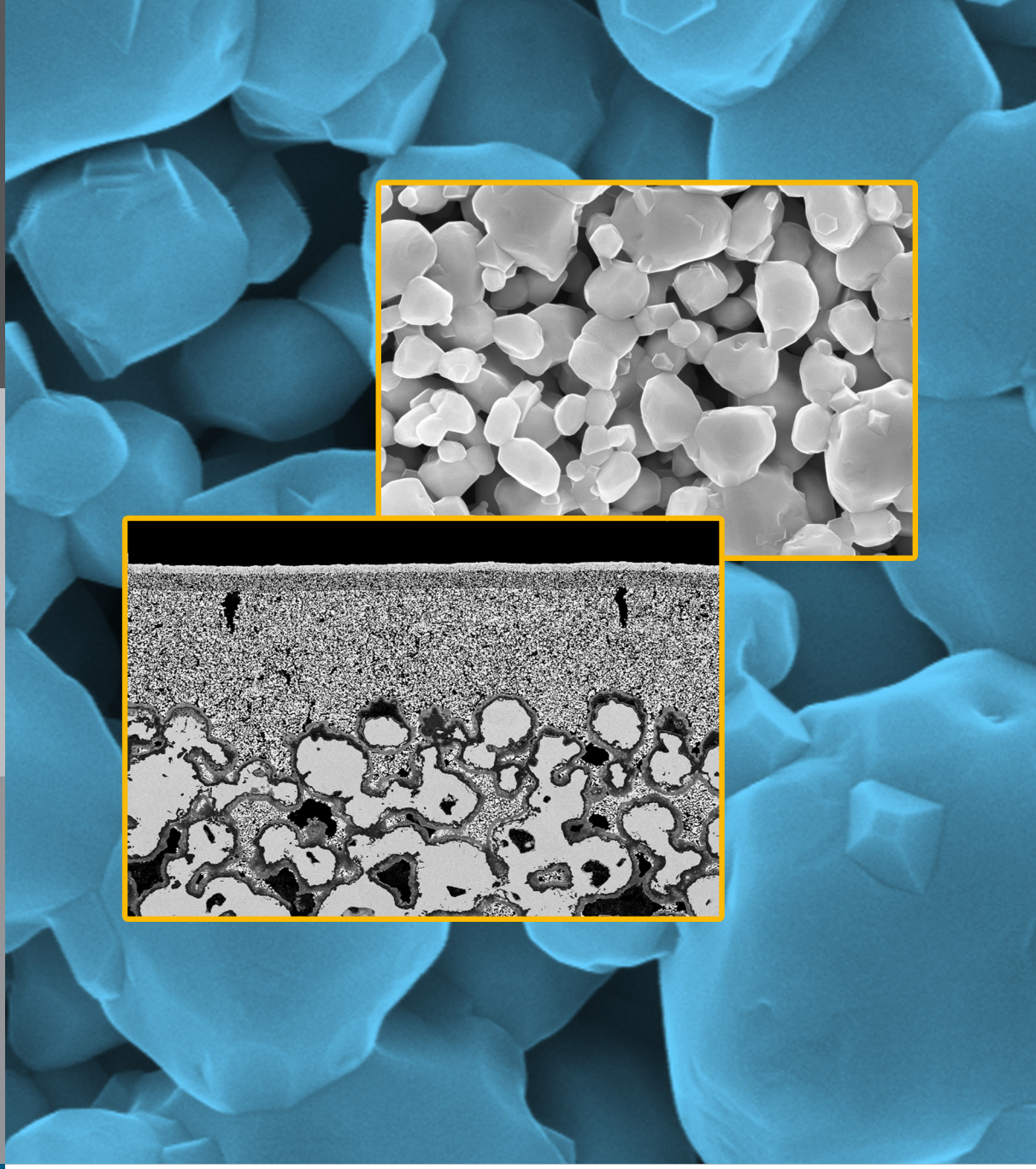

Development of Thin Film Oxygen Transport Membranes on Metallic Supports

Ye Xing

Mitglied der Helmholtz-Gemeinschaft

JÜLICH
FORSCHUNGSZENTRUM

Schriften des Forschungszentrums Jülich
Reihe Energie & Umwelt / Energy & Environment Band / Volume 130

Forschungszentrum Jülich GmbH
Institute of Energy and Climate Research (IEK)
Materials Synthesis and Processing (IEK-1)

Development of Thin Film Oxygen Transport Membranes on Metallic Supports

Ye Xing

Schriften des Forschungszentrums Jülich
Reihe Energie & Umwelt / Energy & Environment Band / Volume 130

ISSN 1866-1793 ISBN 978-3-89336-765-8

Bibliographic information published by the Deutsche Nationalbibliothek.
The Deutsche Nationalbibliothek lists this publication in the Deutsche Nationalbibliografie; detailed bibliographic data are available in the Internet at http://dnb.d-nb.de.

Publisher and Distributor:	Forschungszentrum Jülich GmbH Zentralbibliothek 52425 Jülich Phone +49 (0) 24 61 61-53 68 · Fax +49 (0) 24 61 61-61 03 e-mail: zb-publikation@fz-juelich.de Internet: http://www.fz-juelich.de/zb
Cover Design:	Grafische Medien, Forschungszentrum Jülich GmbH
Printer:	Grafische Medien, Forschungszentrum Jülich GmbH
Copyright:	Forschungszentrum Jülich 2012

Schriften des Forschungszentrums Jülich
Reihe Energie & Umwelt / Energy & Environment Band / Volume 130

D 294 (Diss., Bochum, Univ., 2011)

ISSN 1866-1793
ISBN 978-3-89336-765-8

The complete volume is freely available on the Internet on the Jülicher Open Access Server (JUWEL) at http://www.fz-juelich.de/zb/juwel

Abstract

Asymmetric membrane structure has an attractive potential in the application of O_2/N_2 gas separation membrane for the future membrane-based fossil fuel power plant using oxyfuel technology, which will reduce the carbon dioxide emission. The aim of this study is the development of a metal supported multi-layer membrane structure with a thin film top membrane layer and porous ceramic interlayers.

Four perovskite materials were studied as candidate membrane materials. Material properties of these perovskite materials were investigated and compared. $La_{0.58}Sr_{0.4}Co_{0.2}Fe_{0.8}O_{3-\delta}$ (LSCF58428) showed sufficient oxygen permeability, an acceptable thermal expansion coefficient and a moderate sintering temperature. Alternatively, $Ba_{0.5}Sr_{0.5}Co_{0.8}Fe_{0.2}O_{3-\delta}$ (BSCF5582) is considered obtaining very high oxygen permeability but a higher thermal expansion and a lower thermal stability than LSCF58428.

Four different Ni-based alloys were studied as candidate substrate materials in the asymmetric membrane structure. The chromia-scale alloys (Hastelloy X, Inconel 600 and Haynes 214) caused Cr poisoning of the membrane layer material LSCF58428 during high-temperature co-firing in air. NiCoCrAlY with a high Al content (12.7 wt%) was found to be the most promising substrate material. It showed a good chemical compatibility with perovskite materials at high temperatures.

In order to bridge the highly porous substrate and the thin top membrane layer interlayers were developed. Two interlayers were coated by screen printing on the porous NiCoCrAlY substrate which was sintered at 1225°C in flowing H_2 atmosphere. Screen printing pastes were optimized by investigating various solvent and binder combinations and various ceramic powder contents. The first interlayer significantly improved the surface quality and the surface pore size has been reduced from 30-50µm on the substrate to few µm on the first interlayer, though it comprised some cracks. The second interlayer had a crack-free and porous structure. The top membrane layer was deposited by physical vapor deposition (magnetron sputtering) with a thickness of 3.8 µm improving the gas-tightness considerably but showing still reasonable air-leakage. Summarizing, the successful development of a metal-perovskite-composite could be shown, which acts as a basis for a further development of a gas-tight metal supported oxygen transport asymmetric membrane structure.

Kurzfassung

Asymmetrische Membranenstrukturen besitzen ein hohes Potenzial die Abtrennung von Sauerstoff aus der Luft in einem fossilen Oxyfuel-Kraftwerk mit geringen Wirkungsgradverlusten zu realisieren. Das Ziel dieser Arbeit ist die Entwicklung einer metallgestützten mehrlagigen Membranstruktur die eine gasdichte sauerstoffinenleitende Dünnschichtmembran, poröse Zwischenschichten und ein poröses metallisches Substrat umfasst.

Als potenzielle Membranmaterialen wurden vier unterschiedliche Perowskite untersucht. Die Materialeigenschaften dieser Perowskite wurden bestimmt und verglichen. $La_{0.58}Sr_{0.4}Co_{0.2}Fe_{0.8}O_{3-\delta}$(LSCF58428) zeigte eine ausreichende Sauerstoffpermeation, einen akzeptablen thermischen und chemischen Ausdehnungskoeffizienten und eine moderate Sintertemperatur. Alternativ wurde $Ba_{0.5}Sr_{0.5}Co_{0.8}Fe_{0.2}O_{3-\delta}$(BSCF5582) berücksichtigt, wodurch im Vergleich zu LSCF58428 sehr hohe Sauerstoffpermeation aber auch ein höherer Ausdehnungskoeffizient und geringere thermische Stabilität erreicht wird.

Für das Substrat wurden vier verschiedene Ni-Basis Legierungen untersucht. Die Chromoxidschichtbildner Hastelloy X, Inconel 600 und Haynes 214 verursachen starke Reaktionen mit dem Membranmaterial LSCF58428 während der gemeinsamen Sinterung. Als vielversprechendsten Substratmaterial wurde NiCoCrAlY mit hohem Al-Gehalt identifiziert. Es zeigte eine gute chemische Verträglichkeit mit Perowskit Materialien bei hohen Temperaturen.

Zur Optimierung der Membranstruktur wurden zwischen Substrat und Funktionsschicht poröse Zwischenschichten entwickelt. Die Zwischenschichten wurden mittels Siebdruck auf dem porösen Substrat NiCoCrAlY aufgebracht das vorher bei 1225°C in reinem H_2 gesintert wurde. Die Zusammensetzung der Siebdruck Pasten wurde durch Verwendung unterschiedlicher Lösungsmittel und Bindemittel-Kombinationen sowie verschiedener Feststoffanteile optimiert. Die erste Zwischenschicht verbesserte deutlich die Oberflächenqualität und führte zur Reduzierung der Porengröße von 30-50 µm auf dem Substrat zu einigen µm in der Zwischenschicht. Da trotz der verbesserten Qualität immer noch Risse in der ersten Schicht auftraten, wurde eine zweite poröse Schicht rissfrei aufgetragen. Die Top-Schicht wurde schließlich mittels physikalischer Gasphasenabscheidung (magnetron sputtering) mit einer Dicken von 3,8 µm abgeschieden. Zusammenfassend konnte die erfolgreiche Entwicklung eines Metall-Perowskitverbundes aufgezeigt und somit eine Basis für zukünftige Weiterentwicklungen einer gasdichten metallgestützten Sauerstofftrennmembran gelegt werden.

Content

1. Introduction and motivation

Global warming is becoming the problem that has attracted the attention of the entire world. One of the main reasons for global warming is the emission of greenhouse gases due to Human being activities. CO_2 is one of greenhouse gases that contribute significantly to the global climate warming. Fossil fuel power plants are the biggest point sources of CO_2-production, which contribute more than 40% of the worldwide anthropogenic CO_2 emissions [IEA04]. Therefore, reduction of CO_2 emissions from electricity production is one of the global challenges for the next decades. Carbon capture and storage (CCS) is an approach to mitigate global warming by capturing carbon dioxide (CO_2) from large point sources such as fossil fuel power plants and storing it instead of releasing it into the atmosphere. CCS is a promising emission reduction option with potentially important environmental, economic and energy supply security benefits [IEA04]. CCS method involves three distinct processes: first, capturing CO_2 from the gas streams emitted during electricity production, industrial processes or fuel processing; second, transporting the captured CO_2 by pipeline or in tankers; and third, storing CO_2 underground in deep saline aquifers, depleted oil and gas reservoirs or unmineable coal seams [IEA04].

In this study the membrane system, which is supposed to be applied for CO_2 capture in fossil fuel power plants, is the research topic. The membrane layer material should have a high oxygen conductivity, which can separate the oxygen from air. Then the fuel in power plant is burned in the oxygen instead of air. After the combustion, the exhaust gas mainly consists of CO_2 and H_2O, which can be condensed to a CO_2 gas stream. Perovskite structure materials exhibit mixed ionic and electronic conductivities, which are the most promising membrane layer materials. Oxygen ions can be transported with an oxygen partial pressure gradient through the bulk membrane by diffusion and surface exchange.

The oxygen permeation flux through a mixed-conducting membrane is increased by reducing the thickness of the membrane. Therefore, it is expected that the oxygen flux can be improved by producing a thin perovskite membrane on a porous substrate, which is called asymmetric membrane structure. The porous substrate strongly influences properties of the whole membrane assembly. Metallic materials show a lot of advantages

as the substrate material compared to other materials, e.g. easy module construction, easy sealing and suitable mechanical properties. Ni-based alloys were studied as candidate substrate material because withstanding a wide variety of severe operating conditions involving corrosive environments, high temperatures, high stresses, and combinations of these factors. However, there are also many challenges, like the thermal expansion mismatch and the interaction with the membrane layer material, the coarse surface for thin film layer coating techniques because of large surface pores and the reduction of the corrosion resistance at high temperatures due to the porous structure, etc, which have to be considered. Therefore, the goal of this study is the development of an asymmetric membrane structure with a top gas-tight thin film perovskite membrane layer on a porous metallic substrate.

2. Fundamentals and background

2.1 Membrane-based fossil fuel power plant concepts

Three different types of CO_2 capture concepts exist: post-combustion capture, oxyfuel combustion, and pre-combustion capture [FIG08] (Figure 2.1), where different membranes can be applied.

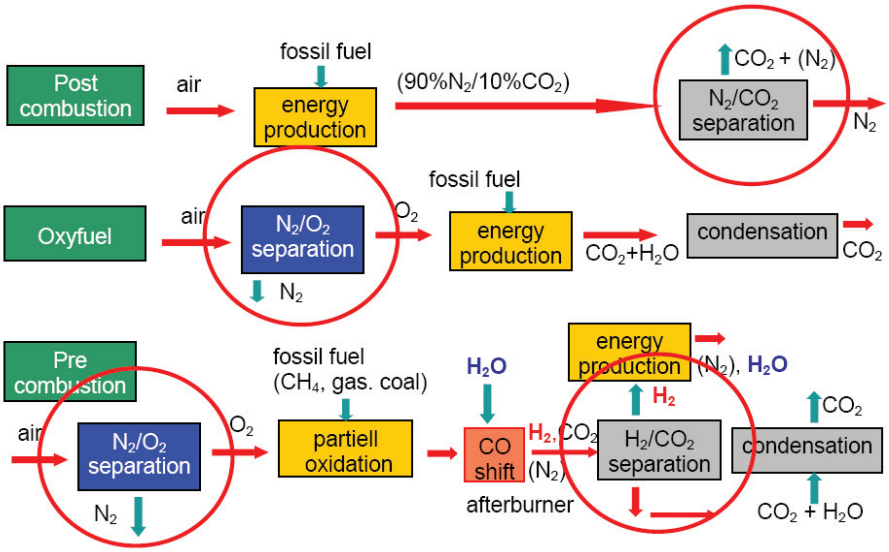

Figure 2.1: Three different types of CO_2 capture concepts

The principle of post-combustion capture is to remove CO_2 from the exhaust gas after combustion. After the energy production in the combustion space, the exhaust gas is passed through the separation membrane, which separates CO_2 from N_2. Post-combustion capture provides a means of CO_2 capture in the near-term for new and existing fossil fuel power plants [THI09]. The membrane based post-combustion capture which can remove selectively CO_2 from N_2 has also an important disadvantage. A membrane unit should process very large volumes of the exhaust gas and since there is no CO_2 pressure difference as a driving force at the membrane location, membranes with very high gas

permeation are needed or an enormous membrane unit has to be installed [GES10]. Zeolite membrane was reported to have a promising performance of N_2/CO_2 separation [SEB07] and different kinds of polymer membrane, e.g. PAMAM dendrimer membranes also have been reported [ZHA08].

In oxyfuel combustion the fuel is burned in the oxygen instead of air. After the combustion, the exhaust gas mainly consists of CO_2 and H_2O, which can be condensed to a CO_2 gas stream. The oxygen separation membrane is required to separate the O_2 from air. Desired properties of a membrane for this application would include the high oxygen permeability, long term phase stability at high temperature (700-900°C) and a chemical stability under CO_2-containing atmosphere. Dense ceramic membranes made of mixed ionic and electronic conducting (MIEC) materials [CZY10] are possible candidates, e.g. $La_{1-x}Sr_xCo_{1-y}Fe_yO_{3-\delta}$ (LSCF) [SUN08].

For pre-combustion capture the O_2 separated from air by an oxygen separation membrane is carried out for the partial oxidation of the fossil fuel. The resulting syngas (CO and H_2) is shifted into CO_2 and H_2. The CO_2 is separated from H_2 through a CO_2/H_2 membrane and captured in a relatively pure exhaust stream. The H_2 can now be used as the fuel, which results in an exhaust gas that consists of water. This technology is often considered as a technology for new-build power plants. Advantages are that multiple fuels can be used and the plant can be used for the production electricity, hydrogen or chemicals. A disadvantage in comparison with the former concepts is the need to construct new power plants. Desired properties of a membrane for this application would include the ability to withstand operating temperatures in the range 200–350°C, operating pressures in excess of 20 bar and components of the shifted gas stream, e.g. CO, CO_2, H_2, H_2O, H_2S. Further, membranes must combine a high H_2 permeability with a sufficient H_2/CO_2 selectivity at temperatures in excess of 200°C [GES10]. Some groups [BER06, OBR09] demonstrated that PBI membranes exhibited higher H_2 permeability and H_2/CO_2 selectivity than commercial membranes. Judkins [JUD01] reported that the porous zirconia membrane on a porous stainless steel support tube showed high permeance and separation factors at elevated temperatures.

This study focuses on the oxygen separation membrane applied for N_2/O_2 separation in oxyfuel combustion. The advantage of oxyfuel combustion is a resulting exhaust gas mainly consisting of CO_2 and H_2O as mentioned before, which can easily be purified by condensation to a gas stream with a high CO_2 content (>90%). This stream can be compressed for transportation and storage [ENG10]. The state of the art oxygen production is cryogenic air separation, which brings in approximate 8.4–10.4%-points efficiency losses for an oxyfuel power plant [PFA09, DIL05]. Mixed ionic and electronic conducting (MIEC) membranes have a high selectivity for the oxygen separation and significantly lower efficiency penalties than cryogenic air separation.

Vattenfall is presently taking an experimental large-scale pilot test facility into operation for the detailed investigation of the oxyfuel combustion process. The plant is located southeast of Berlin in Germany in the vicinity of the existing lignite-fired power plant Schwarze Pumpe. A cryogenic air separation unit located at the site will supply gaseous oxygen with a minimum purity of 99.5% needed for the combustion [STR09].

2.2 Oxygen transport through mixed conducting membranes

The oxygen separation membrane is applied to separate the oxygen from air, which has mixed ionic and electronic conductivities (MIEC). In this chapter the oxygen transport mechanism is described. In principle oxygen transport through a dense MIEC membrane involves three progressive steps (Figure 2.2) [CAO94, LIN94, SUN08]: (i) the surface-exchange reaction on the surface of the membrane at the high P_{O_2} side; (ii) the simultaneous bulk diffusion of oxygen ions and electrons/electron holes in the bulk phase; and (iii) the surface-exchange reaction on the surface of the membrane at the low P_{O_2} side. In an asymmetric membrane assembly the gas transport through the porous substrate has to be considered additionally. The driving force for the overall oxygen transport is the oxygen partial pressure gradient between two sides of the membrane. Dissociation and ionization of the oxygen occur at the feed side (high pressure side), where electrons are picked up from accessible surface electronic states. Oxygen ions migrate via vacancies in the sub lattice through the membrane. Upon arrival at the sweep side (low pressure side), individual oxygen ions with their electrons recombine again to form oxygen molecules, which are released in the permeate stream. The flux of oxygen ions is charge compensated by a simultaneous flux of electronic charge carriers [BOU96].

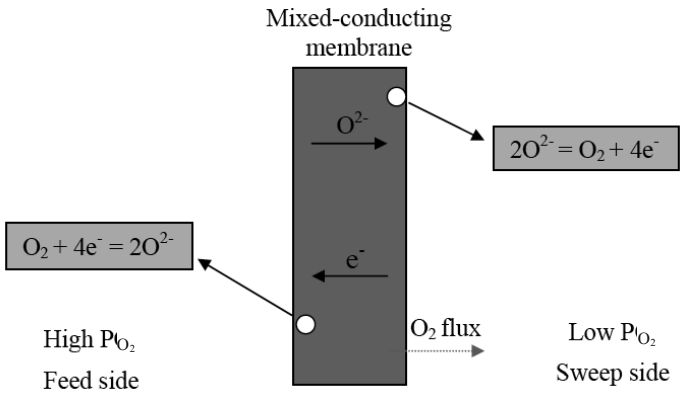

Figure 2.2: Oxygen transport through the MIEC membrane

2.2.1 Bulk transport

The oxygen transport is achieved by the move of oxygen ions and electrons through the bulk membrane. Oxygen ions move takes place by a vacancy transport mechanism, which is compensated by electrons move via hopping of small polarons from elements with multivalence. The transport of oxygen vacancies through the bulk material is obtained by chemical potential gradients. The relationship of each component's chemical potential is given in Equation 2.1 [BOU96].

$$\frac{1}{2}\nabla\mu_{O_2} + \nabla\mu_{V_O^{\bullet\bullet}} + 2\nabla\mu_{e'} = 0 \tag{2.1}$$

$$\nabla\mu_{e'} + \nabla\mu_{h^{\bullet}} = 0 \tag{2.2}$$

where $\mu_{V_O^{\bullet\bullet}}$ denotes the chemical potential of the oxygen vacancy, $\mu_{e'}$ and $\mu_{h^{\bullet}}$ denoting the chemical potential of electrons and electron holes, respectively. The flux of charge carriers j_k can be given by σ_k the conductivity of charge carrier k, z_k the valence of charge carrier k, F the Faraday constant and $\nabla\eta_k$ the gradient of the electrochemical potential (Equation 2.3) [BOU96]. $\nabla\eta_k$ comprises a gradient in chemical potential $\nabla\mu_k$ and a gradient in electrical potential $\nabla\phi$ (Equation 2.4) [BOU96].

$$j_k = -\frac{\sigma_k}{z_k^2 F^2}\nabla\eta_k \tag{2.3}$$

$$\nabla\eta_k = \nabla\mu_k + z_k F\nabla\phi \tag{2.4}$$

At steady state, no charge accumulation occurs. Fluxes of ionic and electronic defects are therefore related to each other by the charge balance (Equation 2.5) [BOU96].

$$2j_{V_O^{\bullet\bullet}} = j_{e'} - j_{h^{\bullet}} \tag{2.5}$$

The flux of oxygen through the membrane can be derived (in Equation 2.7) [BOU96] by combining Equations (2.1)-(2.5), using the relationship (in Equation 2.6).

$$j_{O_2} = -\frac{1}{2} j_{V_O^{\bullet\bullet}} \tag{2.6}$$

$$j_{O_2} = -\frac{1}{16F^2}\left[\frac{(\sigma_{e'} + \sigma_{h^\bullet})\sigma_{V_O^{\bullet\bullet}}}{(\sigma_{e'} + \sigma_{h^\bullet}) + \sigma_{V_O^{\bullet\bullet}}}\right]\nabla\mu_{O_2} \tag{2.7}$$

$$\nabla\mu_{O_2} = RT\frac{\partial \ln P_{O_2}}{\partial x} \tag{2.8}$$

R is the gas constant, L is the thickness of membrane, T is the temperature, P_{O_2} is the oxygen partial pressure and x is distance coordinate. The Wagner equation (Equation 2.9) [WAG75, GEL97] gives the oxygen flux.

$$j_{O_2} = -\frac{RT}{16F^2L}\int_{\ln P'_{O_2}}^{\ln P''_{O_2}} \frac{\sigma_{el}\cdot\sigma_{ion}}{\sigma_{el}+\sigma_{ion}} d\ln P_{O_2} \tag{2.9}$$

where $\sigma_{ion} = \sigma_{V_O^{\bullet\bullet}}$ and $\sigma_{el} = \sigma_{h^\bullet} + \sigma_{e'}$ are the ionic and electronic conductivity, respectively and P'_{O_2} and P''_{O_2} are the oxygen partial pressure of the feed side and the sweep side. The ionic (σ_{ion}) and electronic (σ_{el}) conductivities are dependent on an intrinsic material property, which will be described in chapter 2.3. Operating temperature T and oxygen partial pressure in both sides (P'_{O_2} and P''_{O_2}) are process parameters, which are limited in the application. According to Wagner equation (Equation 2.9), an oxygen flux J_{O_2} through a dense membrane is inversely proportional to the thickness of the membrane L.

This behavior is proved experimentally in numerous publications. Teraoka [TER02] measured oxygen permeation fluxes of $SrCo_{0.8}Fe_{0.2}O_{3-\delta}$ (SCF82) membranes with three different thicknesses at temperatures from 750°C to 900°C. It increased as the thickness decreased and values are given in Figure 2.3a. Li [LI99] measured the oxygen permeation fluxes of $La_{0.2}Sr_{0.8}Co_{0.2}Fe_{0.8}O_{3-\delta}$ (LSCF2828) with different thicknesses (Figure 2.3b). J_{O_2} is proportional to 1/L in the limited range of L.

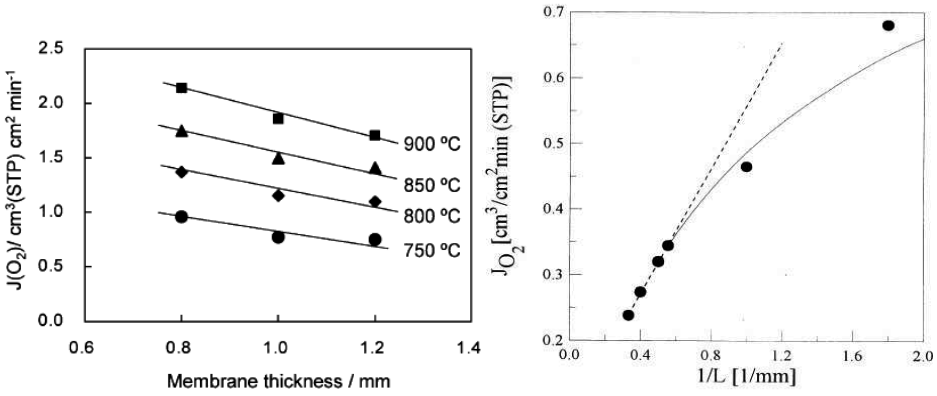

a) SCF82 [TER02] b) LSCF2828 [LI99]

Figure 2.3: Oxygen permeation fluxes of the membrane with different thicknesses

Hong et al. [HON10] reported oxygen permeation fluxes of $Ba_{0.5}Sr_{0.5}Co_{0.8}Fe_{0.2}O_{3-\delta}$ (BSCF5582) plotted as a function of membrane thicknesses (L = 0.5, 0.75, 1 and 1.5mm) at 800°C, 850°C and 900°C. As the thickness of BSCF5582 decreased, the value of oxygen flux increased.

2.2.2 Surface exchange process

Surface exchange is another importance factor impacting the oxygen transport through the membrane. According to the Wagner equation (Equation 2.9), the oxygen flux through the bulk membrane is inversely proportional to the membrane thickness. If the thickness further reduces, the oxygen flux leaves from this inverse relationship, which means that the surface exchange starts to impact the oxygen transport (Figure 2.3b). In the actual application the surface reaction may exert a partial control on the rate of oxygen permeation. The gradient in the oxygen chemical potential will be consumed partly by the surface exchange kinetics. The oxygen permeation will be controlled by diffusion if the membrane is made sufficiently thick. A mixed type of control is encountered upon

decreasing the thickness. Ultimately the surface exchange will become rate determining for very thin membranes [BOU94].

When the oxygen flux is at conditions near to equilibrium, it can be represented by the Onsager equation [GEL97],

$$j_{O_2} = -j_{ex}^{o} \cdot \frac{\Delta\mu_{O_2}^{\text{int}}}{RT} \tag{2.10}$$

$$j_{ex}^{o} = \frac{1}{4} k_s c_o \tag{2.11}$$

where $\Delta\mu_{O_2}^{\text{int}}$ is the chemical potential difference drop across the gas/solid interface. j_{ex}^{o} denotes the balanced exchange rate in the absence of oxygen potential gradients and is accessible from the measurement of ^{18}O-^{16}O isotopic exchange. k_s is the surface exchange coefficient and c_o is the volume concentration of oxygen anions at equilibrium.

For a membrane under the mixed controlled kinetics (bulk diffusion and surface exchange) it is appropriate to define a characteristic membrane thickness L_c, at which point the transition occurs from predominant control by diffusion to that by surface exchange [GEL97]:

$$L_c = \frac{RT}{16F^2} \cdot \frac{\sigma_{el} \cdot \sigma_{ion}}{\sigma_{el} + \sigma_{ion}} \cdot \frac{1}{j_{ex}^{o}} \tag{2.12}$$

If it combines with Equation 2.10, the oxygen flux through the membrane is given by:

$$j_{O_2} = \frac{1}{L \cdot (1 + 2L_c / L)} \cdot \frac{RT}{16F^2} \cdot \frac{\sigma_{el} \cdot \sigma_{ion}}{\sigma_{el} + \sigma_{ion}} \Delta\mu_{O_2}^{total} \tag{2.13}$$

The influence of the membrane thickness on the oxygen flux is described by Gellings [GEL97]. When $L \gg L_c$, the oxygen flux varies inversely with L, in agreement with Wagner equation (Equation 2.9). Departures from this inverse relationship are observed when the oxygen flux becomes partly governed by the surface exchange kinetics. If $L \ll L_c$, a further reduction of membrane thickness will not bring the significant elevation of oxygen flux.

When the electronic conduction predominates, with the classical Nernst–Einstein relationship Equation 2.12 can be simplified as [GEL97]

$$L_c = \frac{D_s}{k_s} = \frac{D^*}{k_s} \tag{2.14}$$

where D_s is the self-diffusion coefficient of oxygen anions with valence charge z_o (=-2) and k_s is the surface exchange coefficient. If correlation effects can be neglected, the tracer diffusion coefficient, D^*, is equal to the self-diffusion coefficient, D_s [GEL97]. D^* can be obtained by the measurement of ^{18}O-^{16}O isotopic exchange. Both D* and k_s for a given material are a function of its specific defect chemistry. Table 2.1 gives the characteristic thickness of different membrane materials from literatures. In general, L_c is a function of process parameters P_{O_2} and temperature.

Haar [HAA01] measured oxygen fluxes of $La_{0.5}Sr_{0.5}CoO_{3-\delta}$ with different thicknesses, i.e. 2.08mm, 0.44 mm, 20 µm and 7.5 µm. At 750°C the oxygen flux increased with a factor 25 from a 20µm thick membrane to a 2.08mm thick membrane. The bulk diffusion dominated the oxygen transport. However, the increase of oxygen flux has been not observed with further reduction from 20µm to 7.5µm, which means the surface exchange is the limiting step.

Table 2.1: Characteristic thickness values of membrane materials from literatures

Perovskite	T (°C)	P_{O_2} (kPa)	L_c[a] (cm)	Ref.
$La_{0.8}Sr_{0.2}CoO_{3-\delta}$	700	70	3×10^{-3}	CAR92
	800		4×10^{-3}	
	900		2×10^{-3}	
$La_{0.6}Ca_{0.4}Co_{0.8}Fe_{0.2}O_{3-\delta}$	700	70	5×10^{-3}	CAR92
	800		5×10^{-3}	
	900		7×10^{-3}	
$La_{0.6}Sr_{0.4}Co_{0.8}Ni_{0.2}O_{3-\delta}$	700	70	2×10^{-2}	FTI93
	800		5×10^{-2}	
	900		2×10^{-1}	
$La_{0.6}Sr_{0.4}Co_{0.4}Ni_{0.6}O_{3-\delta}$	700	70	3×10^{-2}	FTI93
	800		3×10^{-2}	
	900		3×10^{-1}	
$La_{0.6}Sr_{0.4}FeO_{3-\delta}$	1000	6.5	5×10^{-2}	ISH88

2.3 Mixed ionic-electronic conducting materials

The oxygen separation membrane has mixed ionic and electronic conductivities (MIEC). In this chapter the structure of potential materials, doping strategies and common MIEC membrane materials are described.

2.3.1 Perovskite structure

Perovskite is the name for a structural family, in addition to being the name for a particular mineral with the composition, $CaTiO_3$ [BHA00]. Nowadays it means one group materials which have such an ABO_3 structure extensively. The most potential MIEC membrane materials applied for the oxygen separation normally have perovskite structure.

Figure 2.4 shows an ideal perovskite structure. The ideal perovskite structure ABO_3 consists of a cubic array of corner-sharing BO_6 octahedra, where B is a transition metal cation. The A-site ion, interstitial between the BO_6 octahedra, may be occupied by an alkali, an alkaline earth or a rare earth ion. In many cases the BO_6 octahedra are distorted, due to the presence of the A cation, which is generally larger in size than the B cation. The perovskite structure may be regarded as a cubic close-packing of layers AO_3 with B cations placed in the interlayer octahedral interstices [BOU96]. An ideal perovskite is represented by the compositional formula of $A^{2+}B^{4+}O_3$ ($A^{1+}B^{5+}O_3$ or $A^{3+}B^{3+}O_3$ are also possible) with a large A cation and medium sized B cation [BHA00].

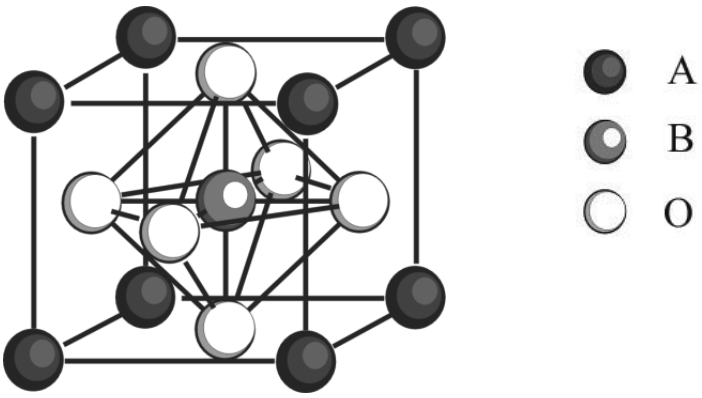

Figure 2.4: Ideal perovskite structure

Tolerance limits of the cationic radii in the A and B sites are defined by the Goldschmidt factor, which is based on geometric considerations (Equation 2.15). R_A, R_B and R_O are the radii of respective ions and t is the tolerance factor [BOU96, GOL26].

$$t = \frac{R_A + R_B}{\sqrt{2}\left(R_B + R_O\right)} \tag{2.15}$$

When the distortion becomes too large, other crystal symmetries such as orthorhombic and rhombohedral appear. Nominally, the perovskite structure should be stable between $0.75 < t < 1.0$. The ideal perovskite lattice exists only for a tolerance factor t very close to one. It is the stability of the perovskite structure that allows for large departures from an ideal stoichiometry, resulting from the substitution with aliovalent cations on the A or B-site or from redox processes associated with the presence of transition metal atoms which can adopt different formal oxidation states. Oxygen vacancies are free to move among energetically equivalent crystallographic sites as long as the perovskite structure exhibits an ideal cubic symmetry. The onset of electronic conductivity mainly depends on the nature of the B-site cation. The total electrical conductivity can be either predominantly ionic as in the acceptor-doped rare earth aluminates or predominantly electronic as in the late transition metal containing perovskites, e.g. Fe, Co and Mn [BOU96].

A perovskite with the ideal structure does not appear to have the capability to conduct oxide ions; there must be a certain amount of imperfections or defects produced according to the non-stoichiometry for the conduction or diffusion to take place [LIU06]. The mixed conductivities of perovskite materials are normally introduced from the doping of A-site and B-site elements. The perovskite material with general formula $La_{1-x}A_xFe_{1-y}B_yO_{3-\delta}$ (A = Sr, Ba, Ca and B = Co, Cu, Ni) are ranked among the most promising materials for oxygen separation membrane. For instance, if Sr^{2+} is doped in a $LaBO_3$ lattice,

$$La^{3+}B^{3+}O_3 + xSr^{2+} \rightarrow La^{3+}_{1-x}Sr^{2+}_{x}B^{3+}_{1-x}B^{4+}_{x}O_3 \tag{2.16}$$

Strontium has a valence of 2+ whereas lanthanum exists in the 3+ form. Thus, as strontium is substituted for lanthanum, there arises a need to charge compensation. Charge

compensation takes place through an increase in the net valence of the transition metal at the B-site (Equation 2.16). Electronic conductivity is typically introduced into the material via multivalent transition metals on the B-site.

Another compensation mechanism involves the oxygen vacancies formation, which results in the nonstoichiometry for these perovskites. The oxygen content in the nonstoichiometric oxides can be adjusted by shifting the temperature and/or oxygen partial pressure, and also the change of the oxygen content within a particular range of temperature and oxygen partial pressure is still reversible and does not change its perovskite structure [SUN08, YIN07]. The creation of lattice oxygen vacancies is indicated by the 3-δ oxygen nonstoichiometry. Figure 2.5 [DAL09] and Figure 2.6 [HAS10] give the oxygen content of $La_{1-x}A_xCo_{1-y}B_yO_{3-\delta}$ at different temperature and under different oxygen partial pressure from literatures, respectively.

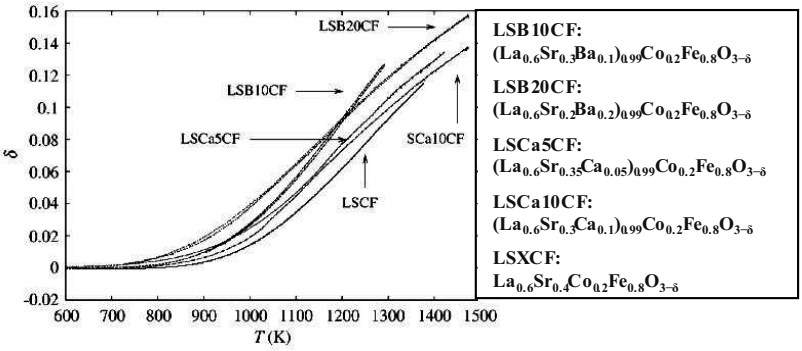

Figure 2.5: δ versus temperature measured in air [DAL09]

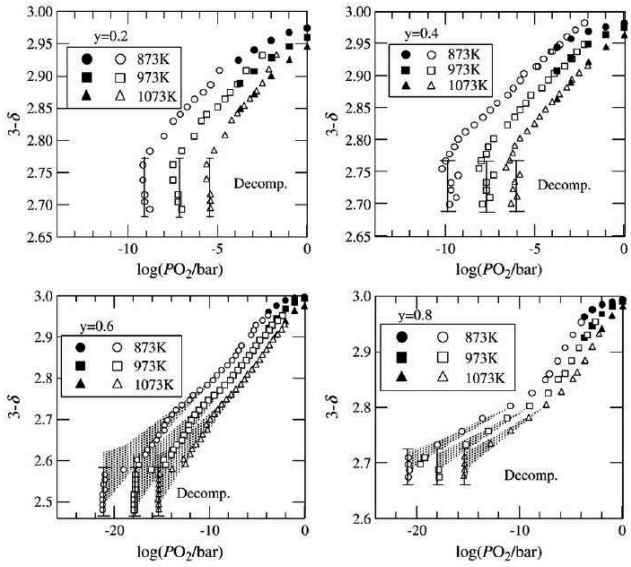

Figure 2.6: Oxygen nonstoichiometry of $La_{0.6}Sr_{0.4}Co_{1-y}Fe_yO_{3-\delta}$ (y=0.2, 0.4, 0.6, 0.8) as a function of P_{O_2}[HAS10]

The ionic (O^{2-}) conductivity is achieved by doping-in acceptor cations of a lower charge than the cation they are replacing. The lower charge is compensated by O^{2-} vacancies, which at sufficiently high temperatures in an oxygen-containing atmosphere provide a vehicle for oxygen-ion conductivity through the lattice. For oxygen anion transport in mixed conducting membranes, higher oxygen fluxes would be in principle favored by a cubic structure, since in preceding from cubic to orthorhombic structures the number of crystallographically equivalent sites favoring ionic transport decreases [SIR06]. Oxygen ionic conductivity, σ, is given by the relationship [KIL00]:

$$\sigma T = A\exp(-\Delta H_m / kT) \tag{2.17}$$

Where:

$$A = N\frac{q^2 A_0^2}{6k} zfc(1-c)\upsilon_0 \exp(\Delta S_m / k) \tag{2.18}$$

And $-\Delta H_m$ (equivalent to E_A) and ΔS_m are, respectively, enthalpies an entropies for the activation, N the equivalent sites per unit volume, q the electronic charge, A_0 the jump distance, z the number of equivalent near neighbour sites, f a correlation factor (representing deviation from randomness), c the fraction of occupied sites, 1-c the fraction of unoccupied sites, υ_0 the lattice vibration frequency, k Boltzmann constant, and T the absolute temperature. From Equation 2.17, it can be seen that the overall ionic conductivity is influenced by the pre-exponential factor A, which is related to the number of lattice sites available for ionic transport [SIR06]. Therefore, an increase in lattice oxygen vacancies leads to an increase in conductivity, but too many vacancies will adversely affect the structure as the lattice becomes unstable resulting in more facile phase changes [THU04].

2.3.2 Doping strategies

Properties of ABO_3 perovskite materials are strongly controlled by dopant elements. When considering materials for oxygen separation, the most important properties are: ionic conductivity, electron conductivity, thermal expansion, chemical stability, chemical expansion, oxygen surface exchange rate, CO_2 tolerance, sinterability and absence of phase transitions within the operating temperature range [SIR06]. The following discussions of material properties will focus on the group of $La_{1-x}A_xFe_{1-y}B_yO_{3-\delta}$ which are the most promising materials for the oxygen separation membrane.

The choice of alkaline earth mixed with La in the $La_{1-x}A_xFe_{1-y}B_yO_{3-\delta}$ perovskite has much impact on the properties. There is also large influence created by altering the ratio x of lanthanum and alkaline earth. The alkaline earths are typically selected from calcium, strontium and barium. In order to facilitate comparison, the ratio y of B-site is set to 0, i.e. $La_{1-x}A_xFeO_{3-\delta}$. Comparison of the impact of composition on some of the important

membrane properties is listed in Table 2.2 [SIR06]. (The number 4 represents the highest value and 1 represents the lowest).

Table 2.2: Effect of A-site doping on perovskite material properties, 1 is lowest, 4 is highest [SIR06]

Composition	Ionic conductivity	Electronic conductivity	Thermal expansion	Oxygen surface exchange	CO_2 tolerance
$La_{0.6}Ca_{0.4}FeO_{3-\delta}$	3	3	3	3	3
$La_{0.6}Ba_{0.4}FeO_{3-\delta}$	4	3	3	3	2
$La_{0.9}Sr_{0.1}FeO_{3-\delta}$	1	1	2	1	3
$La_{0.8}Sr_{0.2}FeO_{3-\delta}$	1	1	2	1	3
$La_{0.6}Sr_{0.4}FeO_{3-\delta}$	3	3	3	3	3
$La_{0.4}Sr_{0.6}FeO_{3-\delta}$	2	2	3	3	3
$La_{0.2}Sr_{0.8}FeO_{3-\delta}$	4	4	3	3	2
$La_{0.1}Sr_{0.9}FeO_{3-\delta}$	4	4	3	4	2

Calcium, strontium and barium each have different impacts on the properties of the perovskite. This is due to the difference in ionic radii of the ions. Calcium has a radius of 1.36 Å, whereas the radii of strontium and barium are 1.44 Å and 1.65 Å, respectively. Thus barium-containing perovskites have a more open crystal lattice and have a higher ionic conductivity compared to strontium- and calcium-based materials. However, barium is more reactive towards CO_2-containing gas mixtures and forms barium carbonate very readily [SIR06]. The doping of the strontium with lanthanum in different amounts has great impact on the ionic and electronic conductivities. Because strontium (and calcium or barium) has a valence of 2+ whereas lanthanum exists in the 3+ form, when strontium is substituted for lanthanum, it is necessary to equilibrate the charge of the cations and oxygen anions in the perovskite. This is achieved through a combination of creating oxygen vacancies in the lattice and changing the valence on the transition metal cation. As more Sr^{2+} replaces La^{3+} the iron cation will change from Fe^{3+} to Fe^{4+} and more oxygen anion vacancies will form. It has also been shown that the electronic conductivity of La_{1-}

$_xA_xFe_{1-y}B_yO_{3-\delta}$ is always very high; therefore, the oxygen permeation rate is limited by the oxygen ionic conductivity [TAS98, TER88a].

A lot of literatures reported conductivities of perovskites. In Tsai's study [TAS98] oxygen ionic conductivities of $La_{1-x}A_xCo_{0.2}Fe_{0.8}O_{3-\delta}$ were measured at 850°C. The order is A_x= $Ba_{0.8}$ > $Ba_{0.6}$ > $Ca_{0.6}$ > $Sr_{0.6}$. When the Sr doping ratio elevates, ionic conductivities of perovskites increase in Stevenson's report [STE96]. Table 2.3 gives values of ionic conductivities from literatures [TAS98, STE96].

Table 2.3: Ionic conductivities of $La_{1-x}A_xCo_{0.2}Fe_{0.8}O_{3-\delta}$ [TAS98, STE96]

Composition	Temperature °C	Ionic conductivity $(\Omega \cdot cm)^{-1}$
$La_{0.2}Ba_{0.8}Co_{0.2}Fe_{0.8}O_{3-\delta}$	850	0.16
$La_{0.4}Ba_{0.6}Co_{0.2}Fe_{0.8}O_{3-\delta}$	850	0.079
$La_{0.4}Ca_{0.6}Co_{0.2}Fe_{0.8}O_{3-\delta}$	850	0.013
$La_{0.4}Sr_{0.6}Co_{0.2}Fe_{0.8}O_{3-\delta}$	850	0.0075
$La_{0.6}Sr_{0.4}Co_{0.2}Fe_{0.8}O_{3-\delta}$	800	0.23
$La_{0.4}Sr_{0.6}Co_{0.2}Fe_{0.8}O_{3-\delta}$	800	0.40
$La_{0.2}Sr_{0.8}Co_{0.2}Fe_{0.8}O_{3-\delta}$	800	0.62

The selection of transition metal cations as B-site elements plays an important role for material properties. Sirman [SIR06] gives one summary that the effect of B-site on material properties (Table 2.4). A cobalt-based perovskite could have high ionic and electronic conductivities and an oxygen surface exchange rate, but the thermal and chemical expansion coefficient is very high. The most common method is the addition of iron with cobalt as B-site elements. Though the doping of Fe lowers ionic and electronic conductivities, it also reduces the thermal and chemical expansion which is beneficial for the practicability. Ullmann [ULL00] reported that ionic and electronic conductivities increase as the amount of Fe decreases (Table 2.5).

Table 2.4: Effect of B-site ion on material properties, first element has the highest property [SIR06]

Properties	Elements
Oxygen ion conductivity	Co, Fe, Ga, Mn, Cr, Ti
Electronic conductivity	Co, Fe, Mn, Cr, Ga, Ti
Oxygen surface exchange rate	Co, Fe, Ga, Mn, Cr, Ti
Thermal expansion coefficient	Co, Fe, Mn, Cr, Ga, Ti
Chemical expansion coefficient	Co, Fe, Mn, Cr, Ga, Ti

Table 2.5: Ionic and electronic conductivities of $La_{0.8}Sr_{0.2}Co_xFe_{1-x}O_{3-\delta}$ at 800°C [ULL00]

Composition	Ionic conductivity σ_o (S/cm) σ_o	Electronic conductivity σ (S/cm) log σ
$La_{0.8}Sr_{0.2}Co_{0.1}Fe_{0.9}O_{3-\delta}$	2.2×10^{-3}	1.50
$La_{0.8}Sr_{0.2}Co_{0.2}Fe_{0.8}O_{3-\delta}$	2.3×10^{-3}	1.94
$La_{0.8}Sr_{0.2}Co_{0.8}Fe_{0.2}O_{3-\delta}$	4.0×10^{-2}	3.00

Thermal expansion coefficient (TEC) of perovskites is one of the most important material properties for a multi-layer structure. The thermal expansion depends on the electrostatic attraction forces within the lattice, which are a function of the concentration of positive and negative charges and their distances within the lattice. The thermal expansion increases if attraction forces decrease. The thermal expansion of a lattice is only caused by thermal lattice vibrations. According to Figure 2.5, δ is increasing as the temperature increases. Therefore, for perovskite materials there is another mechanism attributed to the expansion at high temperatures, called chemical expansion, which is caused by the oxygen loss from the structure with the creation of oxygen vacancies. In most of literatures measured TECs contained the thermal expansion and chemical expansion. Doping elements and doping ratio give a lot of impact on the TEC. Table 2.4 shows that different B-site elements give a strong impact on the thermal expansion and chemical expansion [SIR06]. Petric et al. [PER00] reported thermal expansion coefficients of different La-Sr-

Co-Fe-O perovskites. For the system $La_{1-x}A_xCo_{0.2}O_{3-\delta}$ (Figure 2.7a) a trend of increasing TEC with increasing Sr content can be found. In the system $La_{0.3}Sr_{0.7}Co_{1-y}Fe_yO_{3-\delta}$ (Figure 2.7b) a trend of decreasing TEC with increasing Fe content appears. For a multi-layer structure, the mismatch of TEC is one of the main reasons which lead to the layer cracking or even layer delamination.

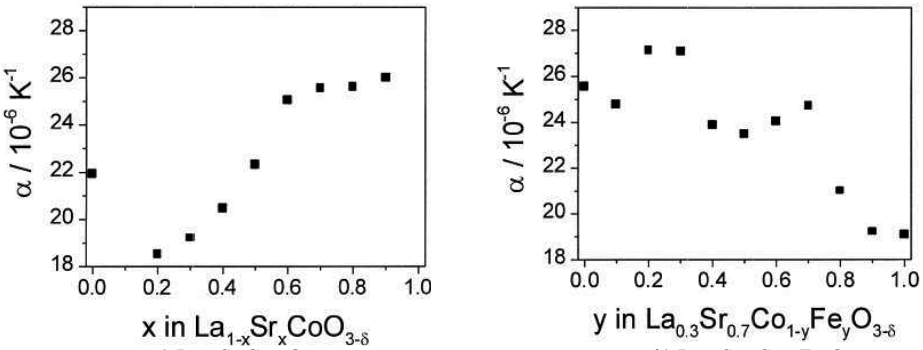

a) $La_{1-x}Sr_xCo_{0.2}O_{3-\delta}$ b) $La_{0.3}Sr_{0.7}Co_{1-y}Fe_yO_{3-\delta}$

Figure 2.7: Thermal expansion coefficients from 30°C to 1000°C of $La_{1-x}Sr_xCo_{1-y}Fe_yO_{3-\delta}$ [PER00]

2.3.3 Perovskite membrane materials

A-Sr-Co-Fe-O group perovskites exhibit high oxygen permeability due to their high ionic and electronic conductivities and high structural stability at high temperatures. These materials have attracted the interest for the application in oxygen separation membrane. Figure 2.8 [SUN08] shows oxygen permeation fluxes of different composition materials. Perovskite materials have obviously higher fluxes than other materials.

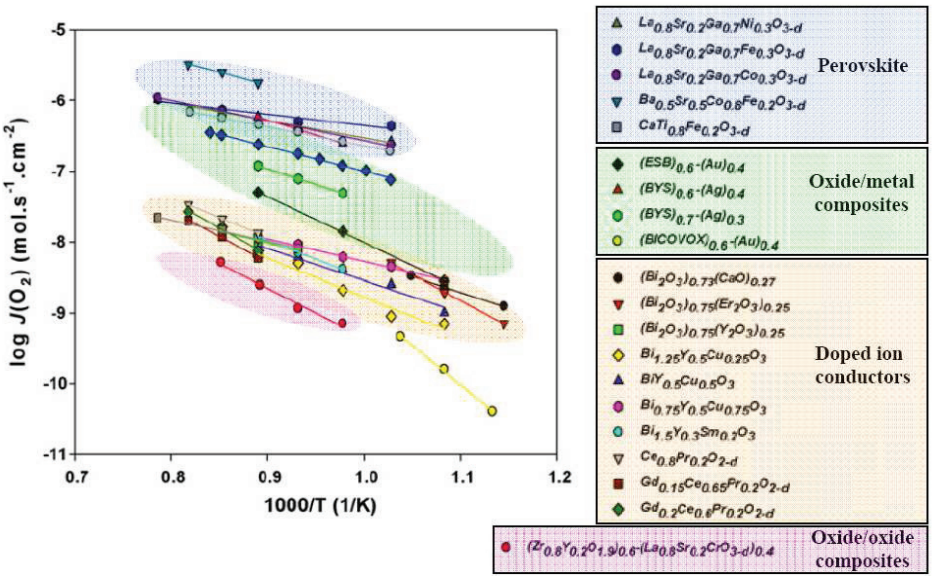

Figure 2.8: Oxygen permeation fluxes of different composition materials [SUN08]

Teraoka et al. [TER85, TER88b] were the first to report high oxygen permeation flux through several $La_{1-x}Sr_xCo_{1-y}Fe_yO_{3-\delta}$ perovskite membranes. The oxygen permeation flux through a membrane increases with increasing Sr and Co contents and the composition $SrCo_{0.8}Fe_{0.2}O_{3-\delta}$ (SCF82) was found to exhibit the largest oxygen permeation flux of ca. 1×10^{-6}mol/s cm^2 at 1173K. Unfortunately, it was found that this material had very limited chemical and structural stability in a low oxygen partial pressure atmosphere [MCI06]. Oxygen vacancy concentration in SCF82 is very sensitive, the chemical expansion causes damage to membranes, especially in the case of thicker membranes [HEN00, PEI95]. However, this issue can be avoided by choosing materials, such as $La_{0.6}Sr_{0.4}Co_{0.2}Fe_{0.8}O_{3-\delta}$ (LSCF6428), whose oxygen nonstoichiometry is less sensitive to an oxygen partial pressure [HEN00]. LSCF6428 has lower oxygen permeability than SCF82, but exhibits excellent stability and consequently is more suitable for a long-term oxygen separation in industrial applications [XU98, SCO02, WAN11].

$La_{0.58}Sr_{0.4}Co_{0.2}Fe_{0.8}O_{3-\delta}$ (LSCF58428) is the primary membrane material performed in this study. It is A-site deficient perovskite material, which means that A/B cation ratio<1 in

ABO_3 structure. Such A-site deficiency can be caused by many factors. It has observed that this A/B nonstoichiometry could affect many properties of perovskite materials, including conductivity, phase transition, and microstructure, etc. The compensation mechanism for electrical neutrality due to the A-site deficiency could be the creation of additional oxygen vacancies and/or the increase of valence state of B-site cations [GE07].

Kharton et al. [KHA00] have studied the conductivity of A-site deficient perovskite $Sr_{1-y}Ti_{0.6}Fe_{0.4}O_{3-\delta}$. An increase in the ionic conductivity was observed with an increasing A-site deficiency. Such improvement of conductivity was attributed in part to an increased oxygen-vacancy concentration from the A-site deficiency. Kostogloudis et al. [KOS99] reported that thermal expansion coefficients of perovskites $La_{0.6-z}Sr_{0.4}Co_{0.2}Fe_{0.8}O_{3-\delta}$ decreased for z=0.05, and then increased slightly with increasing z (Figure 2.9).

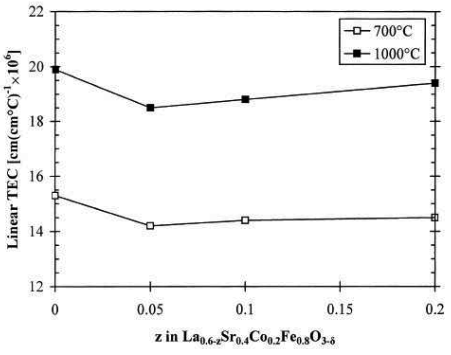

Figure 2.9: TECs of $La_{0.6-z}Sr_{0.4}Co_{0.2}Fe_{0.8}O_{3-\delta}$ [KOS99]

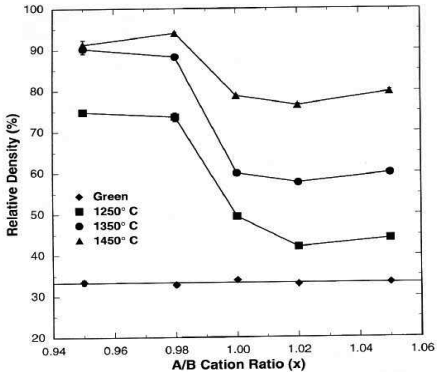

Figure 2.10: Relative densities vs A/B ratio of $(La_{0.7}Sr_{0.3})_xMnO_{3-\delta}$ [STE95]

The A-site deficiency gives an impact on the sintering behavior of perovskites. The sintering of some perovskites was dominated by the diffusion of A-site cations during the densification, and A-site cation vacancies could assist the diffusion of A-site cations. In Stevenson's study [STE95] relative densities of samples after sintering were highly dependent on the A/B ratio, with A-site deficiency resulting in a significant increase in densities (Figure 2.10).

LSCF58428 is one A-site deficient perovskite which has much better properties than LSCF6428 with A/B ratio=1. Literature values of different properties for both La-Sr-Co-Fe-O perovskites are compared. LSCF58428 showed a lower thermal expansion coefficient than LSCF6428, which is 14.9 (10^{-6} K^{-1}) [BÜC07] and 17.5 (10^{-6} K^{-1}) [PET00] at 800°C respectively. LSCF58428 densifies at a lower temperature than LSCF6428, which is 1200°C [BÜC07] and 1350°C [PET00]. The oxygen permeation flux of 1 mm membrane disk made from LSCF58428 showed 0.15ml cm^{-2} min^{-1} at 800°C [SCH10]. The LSCF6428 disk with a thickness of 0.96mm showed 0.05 ml cm^{-2} min^{-1} at 800°C [LAN99]. Schlehuber [SCH10] reported that LSCF58428 has stable oxygen permeation during nearly 3000h of operation at 800°C in an air/argon gradient. The oxygen permeation flow was constant at 0.15 ml cm^{-2} min^{-1}.

$Ba_{0.5}Sr_{0.5}Co_{0.8}Fe_{0.2}O_{3-\delta}$ (BSCF5582) is another membrane material performed in some cases in this study. However, as described before, the BSCF5582 has a very high oxygen permeation flux, but it has a very high thermal expansion coefficient and no CO_2 tolerance.

Shao et al. [SHA00] firstly reported that very high oxygen permeability was observed for the BSCF5582 membrane at 950°C. In another study from Shao [SHA01] a higher oxygen permeation flux than that of SCF82 was observed for BSCF5582. At 850°C, a permeation flux of 1.1ml/cm^2 min was achieved under air/He oxygen gradient for the BSCF5582 membrane.

Barium-based perovskite is more reactive towards CO_2-containing atmosphere and forms barium carbonate. The poisoning effect of CO_2 on the oxygen permeation flux as well as on changes in the microstructure of BSCF5582 membranes was investigated in Arnold's study [ARN07]. Using pure CO_2 as the sweep gas causes an immediate stop of the oxygen permeation flux.

2.4 Asymmetric membranes

According to the Wagner equation (Equation 2.9), the oxygen permeation flux through a mixed-conducting dense membrane can be increased by reducing the thickness of the membrane. When the thickness becomes very low, a porous support is needed for the mechanical stability. Therefore, it is expected that the oxygen flux can be improved by producing thin perovskite membrane on a porous substrate, which is called asymmetric membrane structure.

Some experimental results have already been reported. In Vente et al.'s [VEN06] study the oxygen flux increases by a factor of ~3 from a dense 200µm thick LSCF6428 membrane to a 200µm porous substrate supported 6µm thick LSCF58428 membrane. In Haar et al.'s study [HAA01] they manufactured a 20µm $La_{0.5}Sr_{0.5}CoO_{3-\delta}$ layer on a 0.5mm porous $La_{0.5}Sr_{0.5}CoO_{3-\delta}$ substrate. It showed that the oxygen flux was 10 times higher than a 0.44 mm thick membrane at 800°C. Table 2.6 gives the overview of literature data for asymmetric membranes.

Table 2.6: Overview of literature data for asymmetric membranes

Membrane material	Layer thickness	$j^{asymmetric}$	$j^{asymmetric} / j^{bulk}$	$L^{bulk} / L^{asymmetric}$	T	Source
	µm	ml $min^{-1} cm^{-2}$	-	-	°C	
$La_{0.6}Sr_{0.4}Co_{0.2}Fe_{0.8}O_{3-\delta}$	6	1.2	3.3	33.3	850	[VEN06]
$La_{0.5}Sr_{0.5}CoO_{3-\delta}$	20	1.0	10	22.0	800	[HAA01]
$La_{0.6}Sr_{0.4}Co_{0.2}Fe_{0.8}O_{3-\delta}$	200	0.2	3.3	10.0	800	[JIN01]
$La_{0.58}Sr_{0.4}Co_{0.2}Fe_{0.8}O_{3-\delta}$	20	0.1	1.9	50.0	900	[BÜC07]
$SrCo_{0.4}Fe_{0.5}Zr_{0.1}O_{3-\delta}$	200	1.0	1.9	7.5	900	[CHA08]
$La_{0.6}Ca_{0.4}CoO_{3-\delta}$	10	1.5	4.4	100	900	[WAT08]
$Ba_{0.5}Sr_{0.5}Co_{0.8}Fe_{0.2}O_{3-\delta}$	120	1.94	1.3	8.3	900	[BET10]
$Ba_{0.5}Sr_{0.5}Co_{0.8}Fe_{0.2}O_{3-\delta}$	70	5.1	3.9	14.2	900	[BAU11]

In an asymmetric membrane structure the porous substrate strongly influences the properties of the thin layer, regardless of which coating technology is applied. Generally, a porous substrate should meet the following requirements.

- Sufficient chemical stability at production temperature (higher than application temperature) and in the production atmosphere
- Similar thermal expansion coefficient to membrane layer materials
- Sufficient chemical stability in long term at membrane application temperature (800°C-850°C) and in the application atmosphere
- Sufficient permeability that does not dominate the rate of permeation
- Sufficient mechanical strength at membrane application temperature

2.4.1 Substrate materials

In recent literatures, some candidate materials have been reported as substrate materials of thin film mixed ionic and electronic conducting membrane for oxygen separation. Each material has both advantages and disadvantages.

Some groups reported classic ceramic materials as the substrate material. Middleton [MID04] reported a thin $LaSrCoFeO_3$ layer on a porous MgO support by co-casting and co-sintering. Two layers were co-cast in one production step using aqueous based slurry. The green co-cast layer was then dried and co-sintered at 1400°C for 5h to form the ceramic membrane. The obtained membrane was not fully dense and had some pin holes and cracks. Yin [YIN06] reported that an asymmetric tubular membrane which composed of the porous CeO_2 support and the dense $La_{0.2}Sr_{0.8}CoO_{3-\delta}/CeO_2$ composite membrane (~10μm). The porosity of CeO_2 support is 23.2% and the average pore radius is 1.5μm. Liu [LIU03] applied MgO and ZrO_2 as the porous support for (Pd/Ag)-$La_{0.2}Sr_{0.8}CoO_{3-\delta}$

(LSCO-80) composite membrane. Pd/Ag alloy phase was introduced into the LSCO-80 membrane through a non-powder-blending technique. The MgO support has 43% porosity and 1.7μm mean pore radius, while the YSZ support has 7% porosity and 1.8μm mean pore radius. Classic ceramic materials have low costs and do not require a complex manufacturing process. However, thermal expansion coefficients of classic ceramic materials largely differ from that of perovskite materials, leading to high thermally induced tensile stresses in the membrane layer. In order to solve this problem, another composition is always introduced into perovskite, like ceramic oxide [YIN06] or metallic phase [LIU03], which can lower the TEC mismatch, but also lowers the oxygen permeability.

Some researchers have reported that the thin film membrane layer was coated on a perovskite ceramic substrate. Büchler [BÜC07] mixed LSCF58428 and $Ce_{0.8}Gd_{0.2}O_{1.9}$ (CGO) with different amount as substrate materials, which have porosity from 39% to 57% and around 1.0 μm mean pore radius. LSCF58428 layer was coated by screen printing as a thin film membrane. The fact of using a very similar material for substrate and thin-layer warranties the thermal expansion match and therefore the absence of tensile cracks in the top-layer. Jin [JIN01] reported the LSCF6428 thin layer coated by slip casting on a porous LSCF6428 substrate. Thin layer was coated on the green substrate and then co-sintered at 1573K for 2h in air. It showed dense and crack-free top layer. Baumann [BAU11] reported that both the membrane layer and the support were manufactured by tape casting using BSCF5582. When perovskite materials are produced for porous substrates, compatibility and TEC mismatch problems are avoided. However, they still have some drawbacks, such as joining problems, high brittleness, low strength and a high cost.

Even more interesting although challenging is the potential use of metallic substrates coated with thin perovskite films due to easy module construction, sealing and suitable mechanical properties [BÜC07]. Chen [CHE03] plasma sprayed $La_{0.2}Sr_{0.8}Cr_{0.2}Fe_{0.79}Mg_{0.01}O_{3-\delta}$ (LSCFM) on stainless steel substrates. However, the oxidation resistance of commercial stainless steels within the membrane application

temperature range of 800-850 °C was inadequate [COO08]. The thermal expansion coefficient was also mismatched with perovskite materials.

2.4.2 Ni-based alloys as the substrate material

Ni-based alloys have a lot of applications because of their properties withstand a wide variety of severe operating conditions involving corrosive environments, high temperatures, high stresses, and combinations of these factors. Pure nickel is ductile and tough because it possesses a face-centered crystal structure up to its melting point. Nickel offers very useful corrosion resistance itself and provides an excellent base for developing specialized alloys. Intermetallic phases can be formed between nickel and some of its alloying element, e.g. Cr, Co, Al and etc, which enables the formulation of very high strength and high corrosion resistance alloys for both low- and high-temperature applications [EZU03].

The Ni-based alloys normally generate a two-phase equilibrium microstructure, consisting of gamma (γ) and gamma-prime (γ'). The continuous matrix (called gamma γ) is a face-centered-cubic (fcc) Ni-based austenitic phase that usually contains a high percentage of solid-solution elements such as Co, Cr, Mo, and W. The primary strengthening phase in Ni-based alloys is $Ni_3(B)$, e.g. B=Al or Ti, and is called gamma prime (γ′). It is a coherently precipitating phase (i.e. crystal planes of the precipitate are in registry with the gamma matrix) with an ordered $L1_2$ (fcc) crystal structure. The close match in matrix/precipitate lattice parameter (~0-1%) combined with the chemical compatibility allows the γ′ to precipitate homogeneously throughout the matrix and have long-time stability [BOW00].

Commercial Ni-based alloys contain different elements. Chromium and aluminium are essential for oxidation resistance and small quantities of yttrium help the oxide scale to cohere to the substrate. Polycrystalline alloys may contain grain boundary strengthening

elements such as boron and zirconium, which segregate to the boundaries. The resulting reduction in grain boundary energy is associated with better creep strength and ductility when the mechanism of failure involves grain decohesion. Another possibility is the addition of the carbide formers (C, Cr, Mo, W, C, Nb, Ta, Ti and Hf). The carbides tend to precipitate at grain boundaries and hence reduce the tendency for grain boundary sliding. Elements such as cobalt, iron, chromium, niobium, tantalum, molybdenum, tungsten, vanadium, titanium and aluminium are also solid-solution strengtheners, both in γ and γ' [BHA03].

The primary uses of Ni-based alloys are in: (i) aircraft gas turbines, e.g. disks, combustion chambers, bolts, castings, shaft exhaust systems, blades, vanes, etc.; (ii) steam turbine power plants, e.g. bolts, blades, stack gas reheaters; (iii) reciprocating engines, e.g. turbocharger, exhaust valves, hot plugs, etc.; (iv) metal processing, e.g. hot work tool and dies, casting dies; (v) medical applications, e.g. dentistry uses, prosthetic devices; (vi) space vehicles; (vii) heat-treating equipment; (viii) nuclear power systems; (ix) chemical and petrochemical industries; (x) pollution control equipment; and (xi) coal gasification and liquefaction systems [LIU10].

Inconel alloys belong to the Ni–Cr-based alloys family which covers a wide range of compositions and mechanical properties, which are intented for heat treatment recipients, turbines, aviation, nuclear power plants, and so on. They have good cryogenic properties, good fatigue and mechanical strength at high temperatures and relatively good creep behavior. Ni and Cr provide resistance to corrosion, oxidation, carburizing and other damage mechanism acting at high temperatures. Usually, Inconel alloys are extra-alloyed with Al, Ti, Nb, Co, Cu and W to increase mechanical and corrosion resistance. Fe can also be present in amounts ranging 1–20% [THO06].

Haynes 230, Hastelloy S and Haynes 242 were evaluated as interconnect materials for solid oxide fuel cell (SOFC). The SOFC is operated at temperature from 650°C to 800°C and interconnects are exposed simultaneously to an oxidizing gas (air) at the cathode side and a reducing gas (e.g. H_2) at the anode side during operation. Three of Ni–Cr-based alloys, which are mechanically stronger than ferritic stainless steels, demonstrate excellent oxidation resistance and satisfactory scale electrical conductivity for SOFC interconnect

applications if they contain enough Cr. However, TEC mismatch to cell components should be addressed [YAN06].

MCrAlY (M=Ni, Co), which comprises a high aluminum content, is applied as the bondcoat in the thermal barrier coating (TBC) coated internally cooled metallic-superalloy components for the high-efficiency gas-turbines and aircraft-engines due to the hot corrosion and oxidation resistance at high temperature [SEO08, SUB08].

In this study Ni-based alloys were studied as substrate materials, benefiting from a number of advantages, such as excellent high temperature mechanical properties, easy joining, high-temperature chemical stability and closer thermal expansion coefficients in relation to selected perovskite materials than ceramics such as alumina or zirconia. The membrane structure operates in an oxidizing atmosphere at temperature 750°C-850°C and during the manufacture process even higher temperature may be reached. At high temperatures, Ni-based alloys rely on the thermal growth of an oxide scale on their surfaces to protect the rest of material from the further environmental attack. In terms of composition, the oxide scale can be either a chromia layer, called chromia scale alloys, or an alumina, called alumina scale alloys, depending on the concentration of the scale forming elements in the metallic substrate.

2.5 Coating techniques

2.5.1 Screen printing

Screen printing is a relative simple coating method, which is used in a lot of applications. In this study it is applied for coating the interlayer, which is directly on the metallic substrate. In screen printing a quantity of paste is squeezed through a sieve and the thin layer is coated on the substrate. The pattern and thickness of the layer is controlled by the sieve. Figure 2.11 [HOB97] is the schematic picture of the screen printing process.

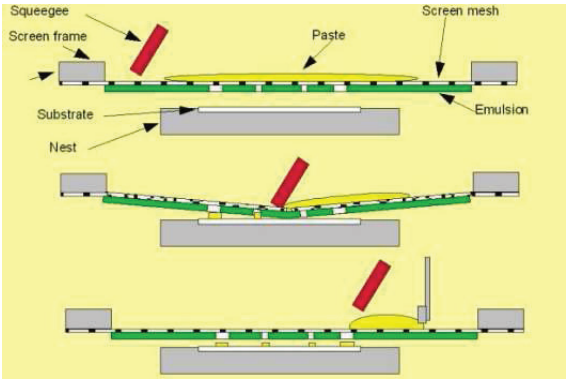

Figure 2.11: Schematic picture of the screen printing process [HOB97]

The screen printing paste gives a strong impact on the screen printing layer. The paste is normally mixed by the aimed material powder, solvent and chemical additives. The rheological behavior and green density of paste are the most important properties in this study. During the co-firing process the mismatch of shrinkage between the screen printed layer and the substrate may lead to the cracks or even the layer delamination. The shrinkage of screen printed layer can be reduced by increasing the layer green density which resulting from the paste optimization (Equation 2.21).

$$\rho_{green} \cdot d_0^3 = \rho_{th} \cdot (d_0 - \Delta d)^3 \tag{2.19}$$

$$s = \frac{\Delta d}{d_0} \tag{2.20}$$

ρ_{green} is the green density of screen printing paste. ρ_{th} is the theoretical density of paste material. d_0 is the original length. Δd is the variance of the length. s is the linear shrinkage. Based on Equation 2.19 and 2.20, the lineal shrinkage s is given by ρ_{green} (Equation 2.21).

$$s = 1 - \sqrt[3]{\frac{\rho_{green}}{\rho_{th}}} \tag{2.21}$$

2.5.2 Physical vapor deposition (PVD)

Physical vapor deposition (PVD) is carried out for the deposition of the top membrane layer in this study. PVD is one classic deposition method for thin film layer fabrication. In PVD processes the material to be deposited is transformed into a gaseous state by a physical process. Generally PVD processes are carried out under vacuum conditions. The process involved four steps: Evaporation) the material to be deposited is converted into vapor by physical means like heating or attacking by a high energy source, e.g. Argon ion beam. Transport) this process simply consists of the movement of vaporized atoms from the target to the substrate to be coated. Reaction) in some cases coatings will consist of metal oxides, nitrides, carbides and other such materials. In these cases, the target will consist of the metal. The atoms of metal will then react with the appropriate gas during the transport stage. The reactive gases may be oxygen, nitrogen and methane. Deposition) this is the process of coating build up on the substrate surface. Depending on the actual process, some reactions between target materials and the reactive gases may also take place at the substrate surface simultaneously with the deposition process [JOH07].

The most common PVD processes nowadays are electron beam physical vapor deposition (EB-PVD) and sputtering. EB-PVD is a process in which a focused high energy electron

beam is directed to melt the target materials in a vacuum chamber. The evaporating material condenses on the surface of the substrates or components resulting in the formation of deposit [SIN05]. In sputtering, a gas discharge, typically argon, creates plasma that is used to eject atoms from the target. In a truly physical process, accelerated ions collide with the material that is to be deposited thus releasing the atoms from the bulk. There atoms then make the journey across the chamber where they finally condense onto a substrate [JOH07]. Magnetron sputtering was developed to increase the deposition rates. In normal sputtering systems, not all of the electrons contribute toward ionization. The wasted electrons fly around the chamber causing excess radiation and colliding with the chamber walls and target causing unwanted heating. The magnetron is a magnetically assisted discharge that traps electrons near the target surface. This locally increases the ionization of the argon gas thereby enhancing the ion bombardment and sputtering rates [JOH07].

In this study the top membrane layer was coated by magnetron sputtering on the interlayer, which is aimed to be gas-tight layer. Advantages of PVD technology for the top layer deposition in this study include the relatively low process temperature and no further shrinkage of the layer.

3. Experimental

3.1 Membrane materials synthesis

$La_{1-x}Sr_xCo_{1-y}Fe_yO_{3-\delta}$ (LSCF) and $Ba_{0.5}Sr_{0.5}Co_{0.8}Fe_{0.2}O_{3-\delta}$ (BSCF5582) were studied as membrane materials because of their promising properties. The ratios x and y in LSCF play a very important role on the properties of materials. Proper x and y lead a moderate thermal expansion coefficient, a high oxygen permeation flux and a high long-term stability. In this study $La_{1-x}Sr_xCo_{1-y}Fe_yO_{3-\delta}$ with different x and y ratios were evaluated from the oxygen permeability and the thermal expansion coefficient to search the best performance material. BSCF5582 is added for the comparison.

LSCF powders with different compositions were synthesized, i.e. $La_{0.58}Sr_{0.4}Co_{0.2}Fe_{0.8}O_{3-\delta}$ (LSCF58428), $La_{0.58}Sr_{0.4}Co_{0.8}Fe_{0.2}O_{3-\delta}$ (LSCF58482) and $La_{0.2}Sr_{0.8}Co_{0.8}Fe_{0.2}O_{3-\delta}$ (LSCF2882). LSCF58428 powder was synthesized in large amount using the spray-drying technique. It started from nitrate precursors, which were dissolved into water. The mixing ratio was dependent on the aimed stoichiometry. The solution was sprayed through the nozzle where the temperature of the air flow was around 300°C and the water in the solution evaporated immediately. It created fine spherical shaped particle with a particle size from 2µm to 50µm and different cations distributed homogenously. The powder was calcined at 900°C in order to develop the perovskite phase. LSCF58482 and LSCF2882 powders were synthesized by pechini method [PEC67]. The process procedure is given in Figure 3.1. Nitrates with desired amounts of cations and water were added into quartz glass which has a diameter of 10cm and a height of 50cm and stirred at 70°C until all nitrates were dissolved. Then the citric acid was added into the solution and continued to stir for approx. 30min. The amount of citric acid was 4 times the total cations mol amount. Finally the ethylene glycol with 2 times the total cations mol amount was added and the temperature was increased to 170°C. When the water was evaporated completely from the mixture, Gel was formed. The pre-calcination temperature was 650°C and the powder was calcined at 900°C for 5h to achieve the perovskite phase finally. Pechini method is a very simple powder synthesis method, but the production amount is relatively low, which is suitable for different composition study in laboratory scale.

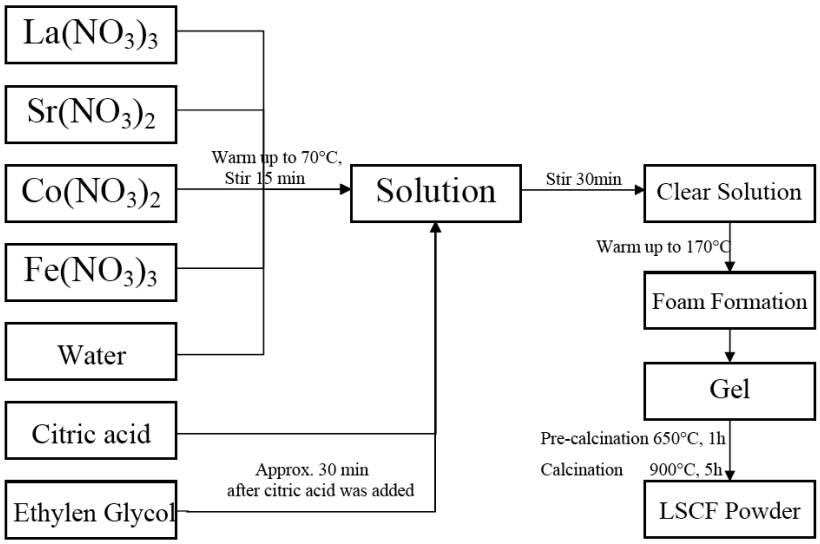

Figure 3.1: Pechini method for the powder synthesis [PEC67]

The BSCF5582 powder was provided by Treibacher (Treibacher Industrie AG, Althofen, Austria). It was manufactured by solid state reaction with BaO, SrO, Co_3O_4 an Fe_2O_3.

The stoichiometry of the powder was confirmed by inductively coupled plasma-optical emission spectrometer (ICP-OES), while the phase composition was determined by X-ray diffraction. All of the powders were milled with zirconia balls in ethanol to obtain the desired particle size distribution.

3.2 Substrate materials

Since Ni-based alloys have excellent high temperature mechanical properties, excellent high temperature corrosion resistance in oxidizing atmosphere and close thermal expansion coefficients in relation to selected perovskite membrane materials, they were studied as candidate substrate materials.

Hastelloy X and Inconel 600 were provided by GKN (SIKA R0.5AX, GKN Sinter Metals Filters GmbH, Radevormwald, Germany). They were manufactured by co-axial pressing. The powder was filled into the appropriate dies and compacted in an axial direction by means of an upper and a lower ram. Then the compacted part was sintered in the furnace to form a rigid part.

Haynes 214 and NiCoCrAlY were provided by PLANSEE SE (PLANSEE SE, Reutte, Austria). Both substrates were manufactured by tape casting. Particle size distributions of metallic powders are shown in Figure 3.2. Haynes 214 was sintered at 1150°C for 3h under the flowing hydrogen atmosphere. NiCoCrAlY was sintered at different temperatures, i.e. 1150°C, 1200°C, 1225°C and 1250°C, for 3h under the flowing hydrogen atmosphere.

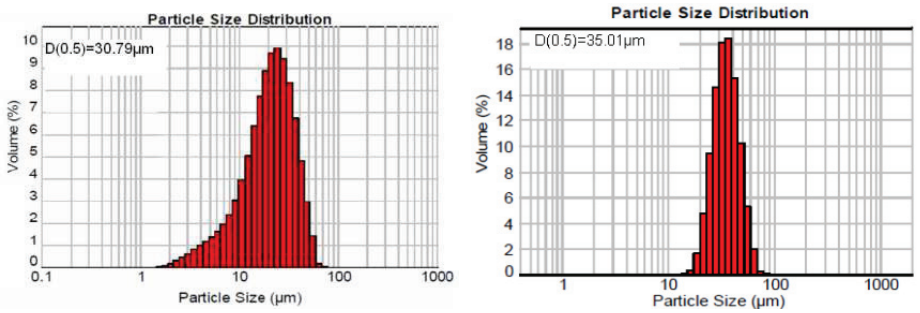

a) Haynes 214 b) NiCoCrAlY

Figure 3.2: Particle size distributions of metallic powders provided by PLANSEE SE

3.3 Layer fabrication

3.3.1 Screen printing

In this study screen printing is applied for coating the interlayer, which is directly coated on the metallic substrate. Figure 3.3 shows the manual screen printing device. The screen printing paste was mixed by ceramic powder, solvent, binder and dispersant. Perovskite materials with desired particle size were as ceramic powder. Terpineol (FLUKA) or BCA (2-(2-Butoxyethoxy)ethyl acetate, 99.2+%) (SIGMA ALDRICH) was mixed as the solvent and ethylcellulose (SIGMA ALDRICH) or Mowital SB 20H (Kuraray Specialisties Europe) was added as the binder. NUOSPERSE® FX 9086 (Elementis Specialties) was applied as the dispersant. Then the three roll mill EXAKT 80E (EXAKT, Norderstedt, Germany) was applied for removing the agglomerate and homogenizing pastes, which is shown in Figure 3.4. The screen printed layer was dried at 60°C and then co-fired with the substrate.

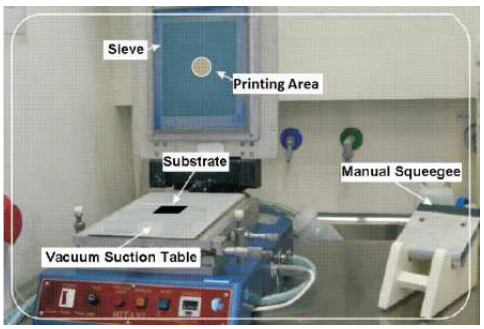

Figure 3.3 Manual screen printing device

Figure 3.4 EXAKT 80E three roll mill

Different pastes were evaluated after manufacture. Rheological behavior of pastes was investigated by Rheometer Physica MCR 301 (Anton Paar). The CyberScan®CT200 Laser topography (Cyber Technologies) gave images of pastes screen printed on polished steel substrates and measured volumes of screen printed layer, which were applied for the calculation of green density with the mass of layer.

3.3.2 Physical vapor deposition (PVD)

The top membrane layer was deposited by PVD Magnetron sputtering. The sputtering was carried out by cluster system CS 400 ES (Ardenne, Dresden, Germany), which are shown in Figure 3.5. This facility consists of four vacuum chambers. Several sample holders can be simultaneously introduced from outside into the central transfer chamber (TC). PC1 is the chamber with sputtering etching ISE 200 and PC2 is the electron beam evaporation chamber. PC3 is the sputtering chamber for the magnetron sputtering PPS-A 250.

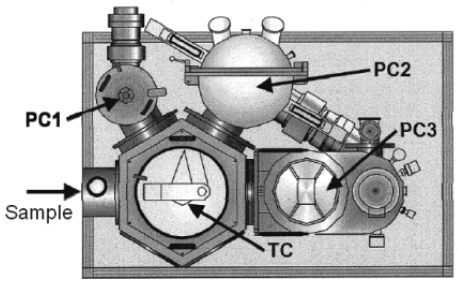

Figure 3.5: Cluster system CS 400ES

Figure 3.6: Perovskite target for sputtering [WEI11]

Before coating sputter etching was carried out for cleaning the sample surface in Ar atmosphere (5.0×10^{-3} mbar) for 10 minutes. The substrate was firstly heated to around 800°C with 5K/min heating rate. After cleaning and heating the substrate, Ar was introduced with the flow rate of 30 sccm (during the coating process the pressure of Ar was kept to 6.0×10^{-3} mbar) and DC-generator was started with power of 500 W. The layer was coated by DC-sputtering with perovskite powder used as the target. The shutter between the substrate and the target was closed until the input energy reached 10 Wh in order to avoid potential contamination from the target surface.

3.4 Characterization methods

3.4.1 Chemical composition analysis

The chemical composition analysis was carried out in Central Division of Analytical Chemistry (ZCH) Forschungszentrum Jülich. Chemical compositions of samples were measured using an inductively coupled plasma-optical emission spectrometer (ICP-OES). The sample is first dissolved in HCl and HNO_3. The ICP source produces a plasma, which is a stream of high-energy ionised gas by inductively coupling argon with a high-frequency field. The sample is injected through the plasma, which results in emission of light of unique frequencies for the given elements. This light is proportional to the concentration of elements in the sample and is measured by an emission spectrometer. The spectrometer is capable of separating the unique frequencies into discrete wavelengths and quantifying the results. The relative error is for the content >1% ±3%, for the content <0.1% ±20% and others ±10%.

3.4.2 Particle size distribution

The particle size distribution of the powder was characterized by Particle Analyzer HORIBA LA-950 (Horiba Europe GmbH, Germany). The LA-950 uses a static laser light scattering, resulting in light scattering patterns characteristic for the particle size with the interaction of the laser light with particles. It is able to measure the particle size over a range of 0.01µm-3000µm.

3.4.3 Dilatometry

Thermal expansion coefficients (TECs) of different materials were investigated. For a multi-layer structure, TECs of different materials play an important role during the

processing and application at high temperature. The TEC describes by how much a material will expand for each degree of temperature increase around a given temperature T, e.g. 1000°C, as given by the formula:

$$\alpha_{1000} = \frac{1}{l_0} \cdot \frac{dl}{dT} \tag{3.1}$$

l_0 is the initiative length of the sample. dl is the change in length of material and dT is the change in temperature.

TECs were measured with a dilatometer DIL 402C (Netzsch) in air. Samples were heated up to 1000°C or 1100°C with 3K/min in air and then held for 30mins. The cooling rate was 3K/min.

3.4.4 X-ray diffraction (XRD)

Phase compositions of materials were characterized by X-ray diffraction with Siemens D5000 diffractometer (Siemens AG, Karlsruhe, Germany) using Cu Kα radiation. The step size was 0.02° and the step time was 2.5s. The acceleration voltage was 40kV and the emission current was 40mA.

Bragg's Law provides the conditions under which a constructive interference of reflected X-ray beams is given. If equation 3.2 is fulfilled, a reflection can be measured:

$$n \cdot \lambda = 2d \cdot \sin\theta \tag{3.2}$$

n is an integer. λ is the wavelength of X-ray and d is the spacing between the planes in the atomic lattice, and θ is the angle between the incident X-ray and the scattering planes. The diffractometer can make a diffraction pattern for the sample. With a diffraction pattern the crystal structure of the sample can be identified.

3.4.5 SEM and EDS

Microstructures of samples were investigated by scanning electron microscopy (SEM) using a Zeiss Ultra 55 scanning electron microscope (Carl Zeiss NTS GmbH, Oberkochen, Germany) and a Tabletop Microscope TM3000 (HITACHI, Tokyo, Japan). The scanning electron microscope (SEM) uses a focused beam of high-energy electrons to generate a variety of signals at the surface of solid specimens. The signals that derive from electron-sample interactions reveal the information about the sample microstructure. The elemental analysis was carried out with energy-dispersive X-ray spectroscopy (EDS) using an INCA energy-dispersive X-ray analysis system (Oxford Instruments, Uedem, Germany). EDS is a chemical microanalysis technique used in conjunction with scanning electron microscopy (SEM). The EDS technique detects X-rays emitted from the sample during bombardment by an electron beam to characterize the elemental composition of the analyzed volume.

3.4.6 Oxygen permeation flux measurement of membrane disks

Oxygen permeation fluxes of membrane disks made from different materials were measured in order to compare the oxygen permeability of materials. Membrane disks were uniaxially pressed with a pressure of 100MPa for 2mins. Then they were densified at high temperatures.

The principle configuration of permeator for oxygen permeation flux measurement is shown in Figure 3.7. The sintered membrane disk was ground to 1mm and then mounted on a glass tube. Two gold rings whose diameters were 15mm were applied as the sealing material, which is a ductile element with a melting point of 1064°C, has inertness to glass as well as membrane materials. Air was introduced into the permeator (Figure 3.8) as the feed gas. Ar was used as the sweep gas. The flow rate of air was 100Nml/min and the flow rate of Ar was 50Nml/min, respectively. The mass spectrometer (Omni Star, Pfeiffer Vacuum, US) measured the gas content in permeate. The oxygen permeation flux J_{O_2} was

calculated from the oxygen concentration $x(O_2)$ of permeate gas F measured by the mass spectrometer divided by A the area of the membrane disk (Equation 3.3). The leakage correction was made by measuring the N_2 amount, and then the corresponding amount of O_2 was subtracted.

$$j_{O_2} = x(O_2) \cdot \frac{F}{A} \tag{3.3}$$

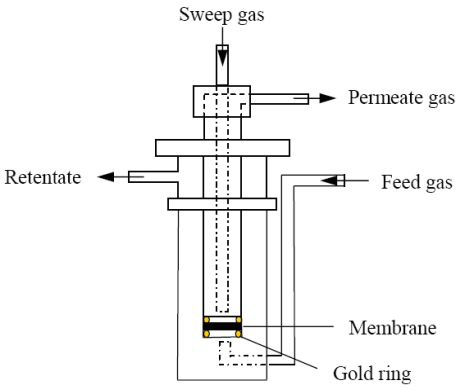

Figure 3.7: Configuration of the oxygen permeator

Figure 3.8: Photo of permeator

3.4.7 Mercury intrusion

Mercury intrusion was applied to measure the porosity-related characteristics of a material. It provides the information including the porosity, the pore size distribution and the surface area. Since mercury does not wet most substances and will not spontaneously penetrate pores by capillary action, it must be forced into pores by the application of external pressure. The required equilibrated pressure is inversely proportional to the size of the pores, only slight pressure being required to intrude mercury into large macrospores, whereas much higher pressures are required to force mercury into small pores. From the collected pressure versus intrusion data, the porosimeter Pascal 440 (THERMO

SCIENTIFIC) generated the volume and size distributions using the Washburn equation (Equation 3.4). p is the applied pressure. γ is the surface tension. θ is the contact angle and r is pore radius.

$$p = -2\gamma \cdot \cos(\theta) / r \tag{3.4}$$

3.4.8 Nitrogen flow permeability of the porous substrate

For the asymmetric membrane the gas permeability of the porous substrate is one of the most important properties, which was measured by nitrogen with the following permeation module (Figure 3.9) [BET10] in this study. The substrate was installed in the metallic module and sealed with silicon rings. The nitrogen with defined pressure was introduced into permeation module from one side and on the other side the flow flux was measured by a flow rate meter ADM 2000 (AGILENT TECHNOLOGIES) under such pressure. The permeation module was connected with the gas reservoir and the flow rate meter. The measurement was carried out at room temperature.

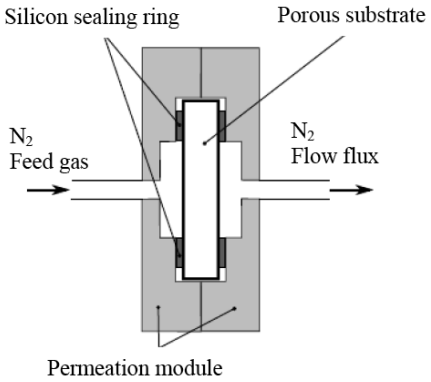

Figure 3.9: Configuration of the nitrogen permeation module [BET10]

3.4.9 Rheological behavior of screen printing pastes

The rheological behavior is one of the most important properties for screen printing pastes, which influences strongly on the performance of screen printed layer. Rheology describes the deformation of a matter under the influence of stresses. Ideal solids can deform elastically. The energy required for the elastic deformation is fully recovered when stresses are removed. Ideal fluids such as liquids and gases deform irreversibly. The energy required for the deformation is dissipated within the fluid in the form of heat and can't be recovered by removing the stresses. Pastes show a rheological behavior that classifies them to a region somewhere between the liquids and the solids: they are in varying extents both elastic and viscous and may therefore be named "visco-elastic" [SCH98]. Viscosity is the resistance of a fluid against shear-induced flow. The Rheometer Physica MCR 301 (Anton Paar) was applied for evaluating the rheological behavior of pastes. The paste was placed between two flat plates and the upper plate was oscillating with a defined velocity during the measurement. The Rheometer gives the flow curve showing the correlation between shear stress and shear rate. The relationship among viscosity η, shear stress τ and shear rate γ is given in Equation 3.5. Viscosity is one property depended on several factors, e.g. temperature, pressure and shear rate.

$$\tau = \eta \cdot \gamma \tag{3.5}$$

The term " complex modulus G* " is introduced to represent the total resistance of a substance against the applied strain. G* (Equation 3.6) [SCH98] is comprised by two parts, one is storage or elastic modulus G' indicating the stress energy temporarily stored during the deformation that is can be recovered afterwards and the other is viscous or loss modulus G" indicating the energy which has been used to initiate flow is irreversibly lost having been transformed into the shear heat [SCH98]. The intersection of storage modulus and loss modulus is named as the flow limit of the paste. During the visco-elastic behavior, the materials flow only after the shearing stress becomes equal or bigger than the flow limit.

$$G^* = G' + iG'' \tag{3.6}$$

4. Results and discussion

The asymmetric membrane structure includes a thin top membrane layer, interlayer and a porous substrate (Figure 4.1). The study started from material characterizations. Four perovskite materials were studied as candidate membrane materials and the substrate material was selected from Ni-based alloys. Then the interlayer was developed on the substrate and the material of interlayer was the same material as the membrane layer material in order to avoid the new contamination and compatibility problems. Finally the thin film membrane layer was deposited on the interlayer by physical vapor deposition (PVD).

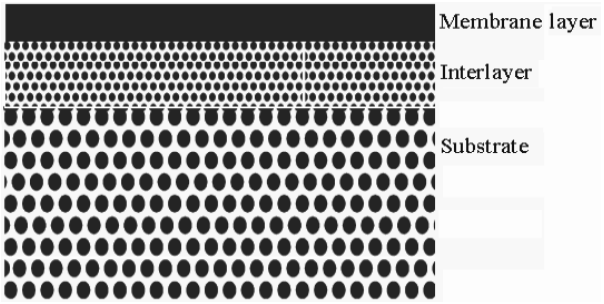

Figure 4.1: Asymmetric membrane structure

4.1 Material Properties

4.1.1 Membrane materials

Four perovskite materials were studied as candidate membrane materials, i.e. LSCF58428, LSCF58482, LSCF2882 and BSCF5582. The stoichiometry of synthesized powder was investigated by ICP-OES. The results with relative errors are given in Table 4.1. The powders showed good agreement with the expected stoichiometry. The phase compositions of these powders after calcination were investigated using X-ray diffraction

and XRD patterns are shown in Figure 4.2. Four materials showed cubic perovskite structures. All three LSCF showed the reflexes at the same θ and BSCF5582 showed the reflexes with slightly lower θ.

Table 4.1: Chemical compositions of candidate membrane materials measured by ICP-OES (error ± 3%)

Expected composition	Abbreviation	Chemical analyses
$La_{0.58}Sr_{0.4}Co_{0.2}Fe_{0.8}O_{3-\delta}$	LSCF58428	$La_{0.58\pm0.02}Sr_{0.40\pm0.02}Co_{0.18\pm0.02}Fe_{0.82\pm0.01}O_{3-\delta}$
$La_{0.58}Sr_{0.4}Co_{0.8}Fe_{0.2}O_{3-\delta}$	LSCF58482	$La_{0.58\pm0.01}Sr_{0.40\pm0.02}Co_{0.78\pm0.02}Fe_{0.22\pm0.02}O_{3-\delta}$
$La_{0.2}Sr_{0.8}Co_{0.8}Fe_{0.2}O_{3-\delta}$	LSCF2882	$La_{0.20\pm0.02}Sr_{0.80\pm0.01}Co_{0.79\pm0.02}Fe_{0.21\pm0.02}O_{3-\delta}$
$Ba_{0.5}Sr_{0.5}Co_{0.8}Fe_{0.2}O_{3-\delta}$	BSCF5582	$Ba_{0.50\pm0.02}Sr_{0.50\pm0.02}Co_{0.79\pm0.02}Fe_{0.21\pm0.01}O_{3-\delta}$

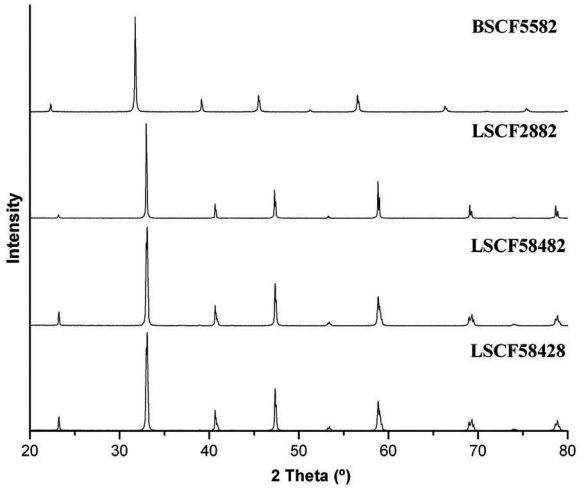

Figure 4.2: XRD patterns of candidate membrane materials

Membrane disks with 1mm thickness for oxygen permeation measurements were manufactured by uniaxial pressing and then sintered at various temperatures from 1100°C

to 1250°C in air in order to investigate the densification temperature. Figure 4.3 gives the cross section microstructures of membrane disks sintered at individual densification temperature. LSCF58428 and LSCF2882 were sintered at 1200°C for 5h. LSCF58482 was sintered at 1250°C for 5h. BSCF5582 was sintered at 1120°C for 5h. These four samples showed the homogenous and dense microstructures with small amount of closed pores.

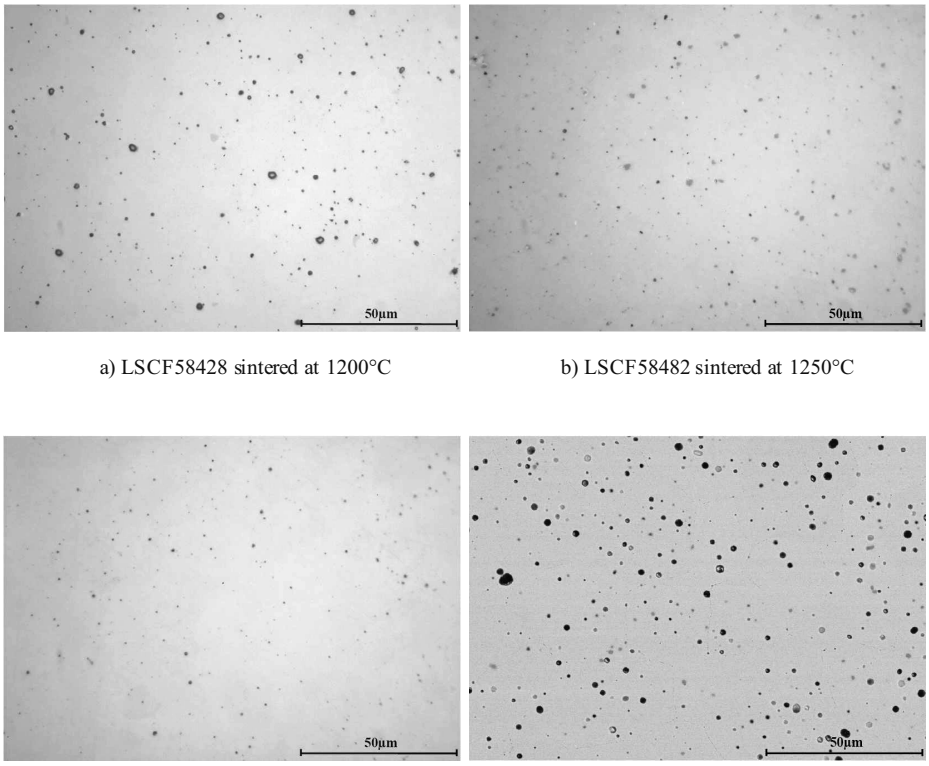

a) LSCF58428 sintered at 1200°C

b) LSCF58482 sintered at 1250°C

c) LSCF2882 sintered at 1200°C

d) BSCF5582 sintered at 1120°C

Figure 4.3: Cross section microstructures of sintered membrane disks

Oxygen permeation fluxes of 1mm membrane disks made from four perovskite materials were measured from 700°C to 900°C. Air with the flow rate of 100Nml/min was introduced as the feed gas. Ar with the flow rate of 50Nml/min was applied as the sweep

gas. Oxygen permeation fluxes are shown in Figure 4.4. Thermal expansion coefficients (TECs) of LSCF58428 and BSCF5582 were measured (Figure 4.5) and TEC of LSCF58482 and LSCF2882 were given by the literature [PET00]. LSCF58428 was considered as the standard material for the comparison. When Co content was elevated as LSCF58482, it showed the similar permeation flux as LSCF58428, but it had a higher densification temperature and a higher TEC. If Sr content and Co content were elevated as LSCF2882, a higher permeation flux was obtained as well as a higher TEC. BSCF5582 had a higher permeation flux than all the three LSCF as can be expected from literatures. Though the standard composition LSCF58428 had a lower permeation flux than LSCF2882, LSCF2882 had a much higher TEC than candidate substrate materials Ni-based alloys (16-19×10^{-6}·K^{-1}), which is unacceptable for a multi-layer structure. If the high permeation flux is pursued, BSCF5582 is better candidate with slightly higher TEC than candidate substrate materials. But the chemical stability at high temperature under CO_2-containing atmosphere should be considered. Table 4.2 summarizes properties of candidate membrane materials.

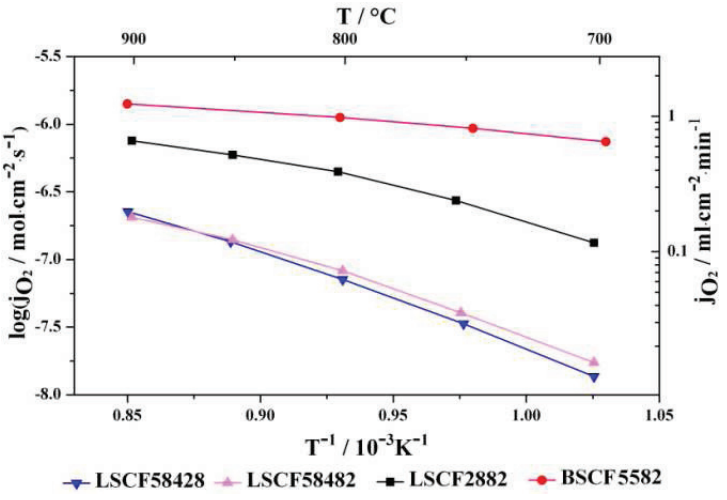

Figure 4.4: Oxygen permeation fluxes of membrane disks with 1mm thickness

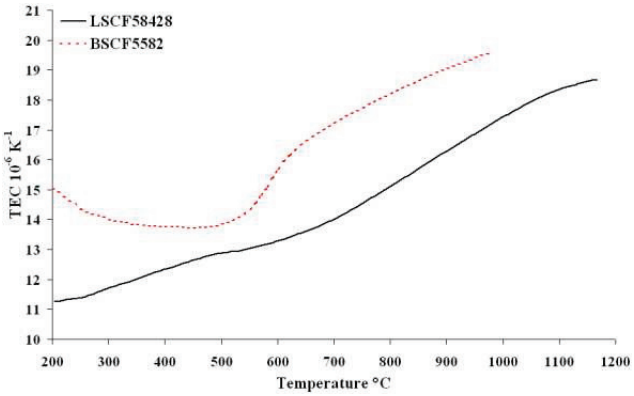

Figure 4.5: Thermal expansion coefficients of LSCF58428 and BSCF5582

Table 4.2: Property comparisons of candidate membrane materials

Materials	Sintering temperature	Permeation flux at 900°C (ml/cm^2·min)	TEC α30-1000°C (10^{-6}·K^{-1})	Element content
LSCF58428	1200°C	0.33	17.3	Standard
LSCF58482	1250°C	0.30	21.4*	High Co
LSCF2882	1200°C	1.11	>27.1*	High Sr and Co
BSCF5582	1120°C	2.09	19.6	Ba content

* [PET00]

Since LSCF58428 and BSCF5582 are the most promising materials for the membrane layer, sintering behaviors of LSCF58428 and BSCF5582 at high temperature were investigated and Figure 4.6 gives the sintering curves of pressed disks. The LSCF58428 and BSCF5582 samples were pressed with 100MPa and had 55%-60% green densities. The sintering behavior of LSCF58428 was measured from room temperature to 1200°C and BSCF5582 was measured from room temperature to 1100°C. LSCF58428 started to shrink from 750°C and the main shrinkage was observed between 1000°C to 1200°C. The shrinkage of BSCF5582 occurred between 850°C and 1100°C. The sintering curve helps to determine the firing temperature of the porous interlayer, which should have a sufficient stability for the further coating process and an open porous structure for the gas permeation.

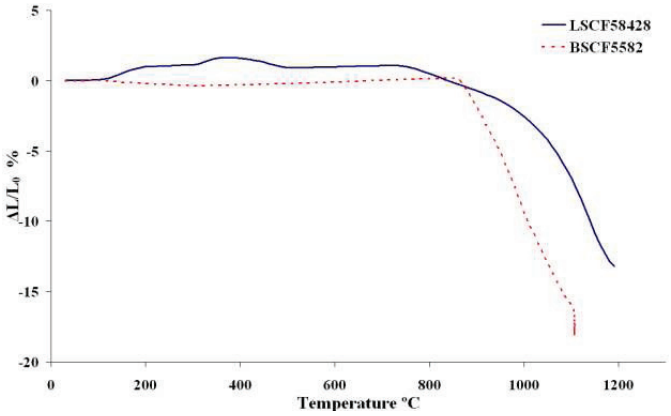

Figure 4.6: Sintering curves of LSCF58428 and BSCF5582

4.1.2 Substrate materials

Four Ni-based alloys were studied as candidate substrate materials, i.e. Hastelloy X, Inconel 600, Haynes 214 and NiCoCrAlY. Chemical compositions of substrates were investigated by ICP-OES. The results are given in Table 4.3. Hastelloy X and Inconel 600 had a high Cr and Fe content beside Ni but consisted of no Al. Haynes 214 and NiCoCrAlY consisted of Al beside Ni and Cr, but the NiCoCrAlY had a much higher Al content than Haynes 214. Al-containing alloys firstly form alumina surface layer at high temperature in an oxidizing atmosphere. If the Al content depletes, other elements like Cr start to oxidize instead of Al.

Table 4.3: Chemical compositions of substrate materials measured by ICP-OES wt% (error ± 3%)

	Ni	Cr	Mo	Al	Co	Fe	Mn	Si	Others
Hastelloy X	48.7	20.6	9.4	< 0.1	1.1	18.5	0.1	0.8	W 0.6
Inconel 600	74.9	15.3	< 0.1	< 0.1	< 0.1	7.4	< 0.1	2.4	~
Haynes 214	72.1	17.3	2.8	3.4	0.9	2.3	0.6	0.6	W 0.2
NiCoCrAlY	45.9	17.3	< 0.1	12.7	22.8	< 0.1	< 0.1	< 0.1	Y 0.6

Having a close TEC to selected membrane materials is one of the basic requirements as the substrate material. TECs of candidate substrate materials were measured and compared with membrane materials in Figure 4.7. TECs of these Ni-based alloys were almost between LSCF58428 and BSCF5582 at the temperature below 900°C. At 1000°C TECs of Inconel 600 and Hastelloy X were slightly lower than that of LSCF58428. During the cooling process, if the TEC of substrate material is slightly higher than TEC of membrane material, it results in the compressive stress condition in the membrane layer, which is favorable for ceramic materials. It is another reason that LSCF58428 is an even better candidate membrane material than BSCF5582.

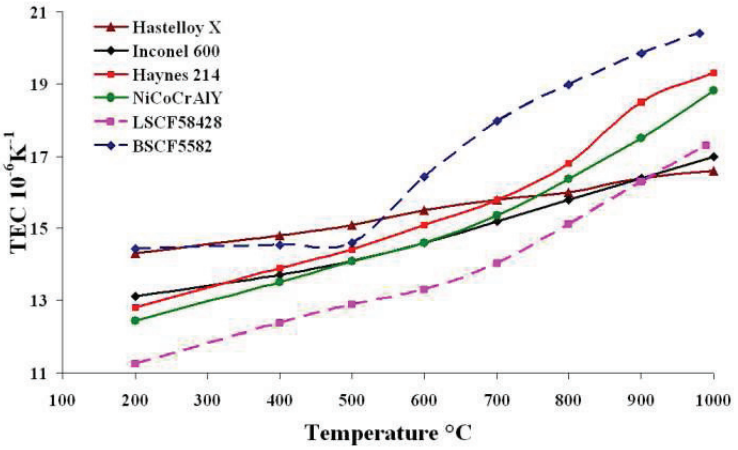

Figure 4.7: Thermal expansion coefficients of candidate substrate materials and membrane materials between 200°C and 1000°C

High temperature corrosion resistance in an oxidizing atmosphere is one important material property for the metallic substrate material. All Ni-based alloys were exposed at high temperatures in air in order to investigate the high temperature oxidation behavior. Figure 4.8 and Figure 4.9 give SEM images and EDS analyses of Hastelloy X and Inconel

600 exposed at 1200°C for 5h in air. Both materials showed similar behavior. As expected a chromia layer formed on the surface to protect the rest of material given in EDS spectrum. But compared to the amount of oxide in bulk materials from SEM images, Hastelloy X comprised much less oxide amount than Inconel 600. Therefore, Hastelloy X had a better oxidation resistance than Inconel 600.

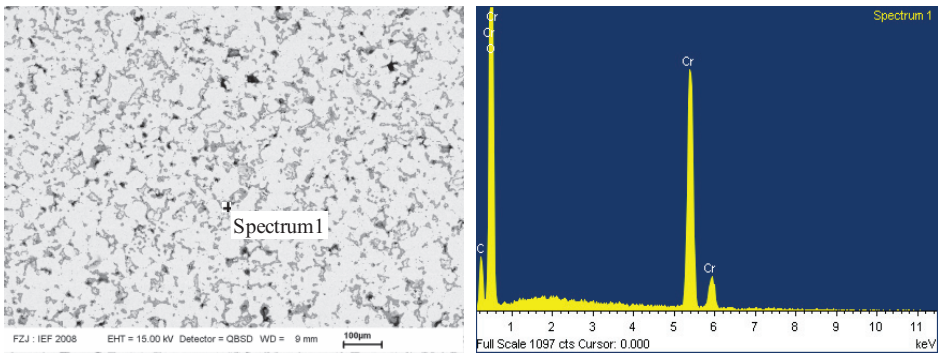

Figure 4.8: SEM image and EDS analysis of Hastelloy X exposed at 1200°C for 5h in air

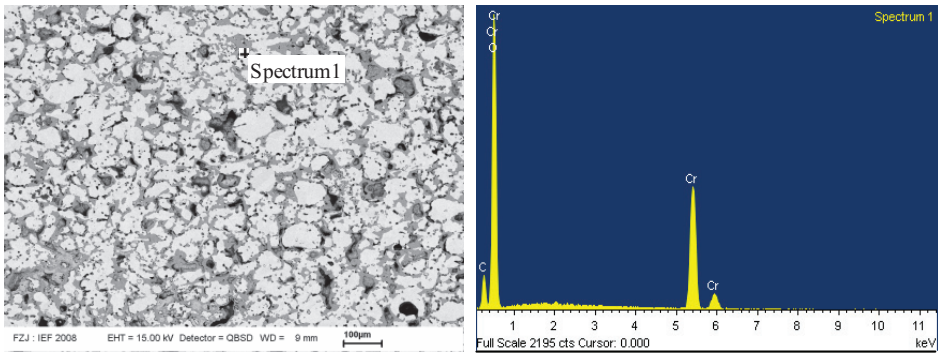

Figure 4.9: SEM image and EDS analysis of Inconel 600 exposed at 1200°C for 5h in air

Figure 4.10 gives SEM images and EDS analyses of Haynes 214 exposed at 1100°C for 5h in air. Based on chemical analyses, Haynes 214 had a 3.4 wt% aluminum content. Because of the quite low Al content, though alumina layer was found in the material (Spectrum 2 in Figure 4.10), the primary surface layer was a chromia layer (Spectrum 1 in Figure 4.10).

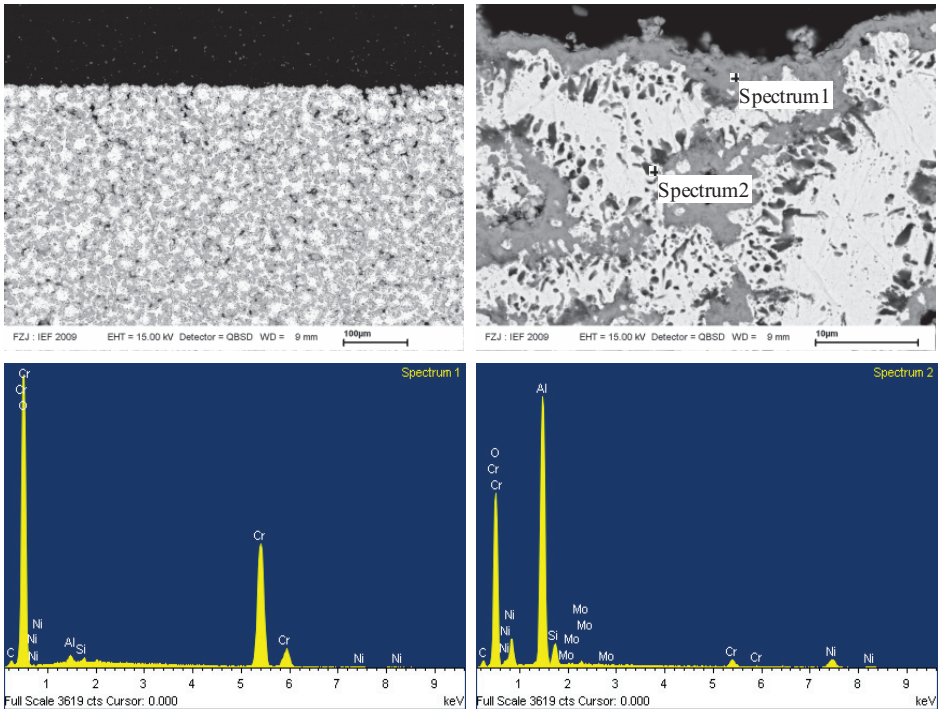

Figure 4.10: SEM images and EDS analyses of Haynes 214 exposed at 1100°C for 5h in air

Figure 4.11 gives SEM images and EDS analyses of NiCoCrAlY exposed at 1100°C for 5h in air. NiCoCrAlY comprised much more Al content than Haynes 214 and it showed the typical two-phase structure, γ-Ni phase and ß-NiAl phase. After exposure, the Al-rich ß phase was observable in Figure 4.11. Spectrum 1 gives element analyses for ß phase and spectrum 2 gives the element analyses for the other γ phase. The surface protection layer comprised primarily alumina shown in spectrum 3 in Figure 4.11. The surface layer

composition in Al-containing alloys strongly depends on exposure parameters and the exposed surface area besides the amount of Al content. If the Al content depletes, other elements like Cr start to oxidize continently.

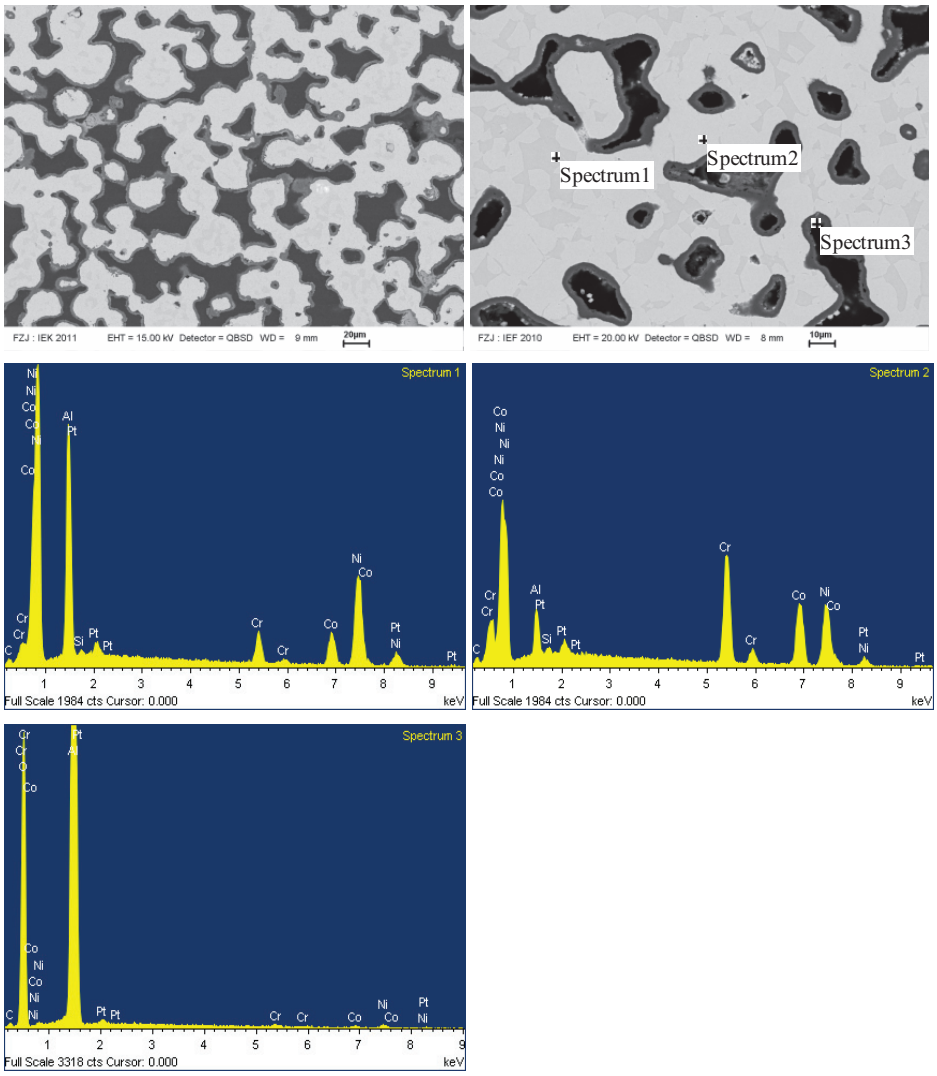

Figure 4.11: SEM images and EDS analyses of NiCoCrAlY exposed at 1100°C for 5h in air

4.2 Interaction of the membrane and substrate materials

For a multi-layer membrane structure the interaction between different chemical composition layers is necessary to be investigated. The interaction is strongly dependent on the process conditions. In this chapter the co-firing atmosphere is firstly investigated. Then interactions between perovskite materials and candidate substrate materials are investigated at high temperature under such an atmosphere.

4.2.1 Co-firing atmosphere

At high temperatures which are required to densify perovskite materials, an oxidizing atmosphere like air has been proven to be a tough co-firing environment for Ni-based alloys, especially when the substrate has quite large exposed surface area due to the porous structure. Therefore, other co-firing atmospheres are investigated. Figure 4.12 shows XRD patterns of LSCF58428 disks sintered at 1200°C for 5h in different atmospheres, i.e. air, high vacuum (10^{-5} mbar), and (4%H_2)/Ar. The disks had a known perovskite structure when sintered in air, as shown in Figure 4.12 III. After vacuum sintering, the material still showed perovskite structure reflexes (Figure 4.12 II) similar to sintered in air. However, reducing the oxygen partial pressure drastically ((4%H_2)/Ar) destroyed the perovskite structure and the phase decomposition occurred, as shown in Figure 4.12 I.

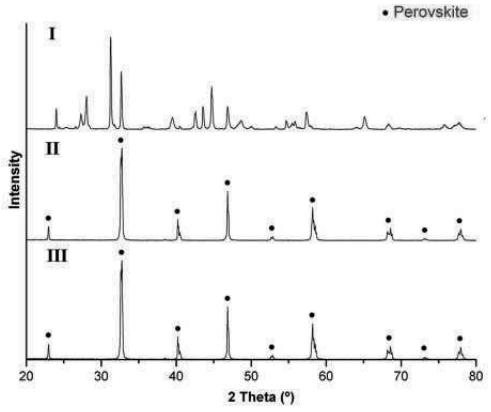

Figure 4.12: XRD patterns of LSCF58428 disks sintered at 1200°C in different atmospheres
I) H_2(4%)/Ar II)Vacuum III)Air

LSCF58428 was screen printed on NiCoCrAlY and co-fired at 1200°C for 5h in a vacuum of 10^{-5} mbar. Before screen printing, the NiCoCrAlY substrate was pre-oxidized at 1050ºC for 5h in air to achieve an alumina protection layer. Phase structures were investigated by XRD analysis. Multi-phase structures were found in the LSCF58428 layer and the perovskite phase decomposed to other phases (Figure 4.13 I). This layer was compared with other samples. LSCF58428 showed a pure perovskite structure when sintered alone in air and vacuum (Figure 4.13 II and IV, respectively). When LSCF58428 was co-fired with NiCoCrAlY in air, it also showed mainly a perovskite structure (Figure 4.13 III).

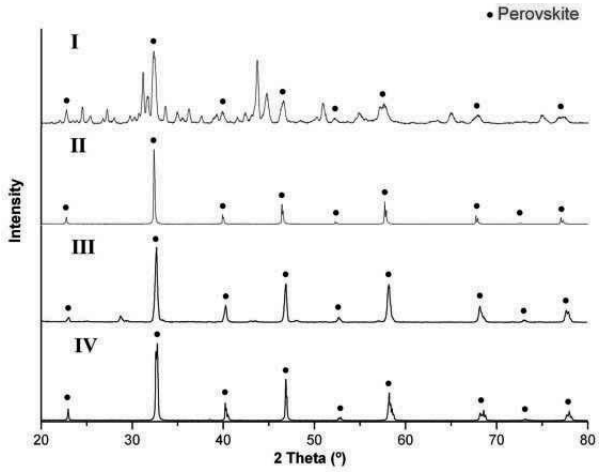

Figure 4.13: XRD patterns of LSCF58428 after heat treatment at 1200ºC for 5h
I) Co-fired with NiCoCrAlY in a vacuum II) Sintered alone in a vacuum
III) Co-fired with NiCoCrAlY in air IV) Sintered alone in air

Elements in NiCoCrAlY (Al, Cr, etc.) have quite a strong tendency to oxide formation. When firing in air, oxygen was permanently fed; in the case of firing in a vacuum, no oxygen resource was present. These elements consumed oxygen from the LSCF58428 leading to a decomposition of the perovskite structure. This reveals the need to co-fire in air.

4.2.2 Chromia scale alloys

Interactions between perovskite materials and Ni-based alloys are investigated in air. The perovskite material was screen printed on the Ni-based alloys. Figure 4.14 shows SEM images and EDS analyses of LSCF58428 screen-printed layer on Hastelloy X after co-firing at 1200°C for 5h in air. The surface layer of the Hastelloy X substrate with a thickness of approx. 2µm consisted mainly of Cr and O and minor amounts of Fe and Ni were found, which were attributed to the adjacent metallic phase due to the limited lateral resolution of EDS (spectrum 1). On top of this chromia layer, a reaction zone with a thickness of approx. 7µm formed with the LSCF58428 layer (spectrum 2). The original LSCF58428 layer with a thickness of roughly 30µm exhibited at least two phases in the back-scattered SEM image. La, Sr, Co, Fe and O with some amounts of Cr and Ni diffused from the substrate were detected all over the sample (spectrum 3-4). Figure 4.15 shows the same investigation with Inconel 600. Spectrum 1 and spectrum 2 located in the LSCF58428 layer, which consisted of elements diffused from the substrate and the LSCF58428 layer showed a multi-phase structure. It was revealed that interactions between Hastelloy X or Inconel 600 and LSCF58428 were quite strong and that it destroyed the single-phase perovskite layer. Based on SOFC research, chromia poisoning, e.g. via volatile $CrO_2(OH)_2$, is a well-known issue with a negative impact on the thermodynamic stability of perovskite cathodes [YOK06]. Therefore, Hastelloy X, Inconel 600 and all other chromia scale materials are not suitable substrate materials for perovskite membranes exhibited to high temperature in air.

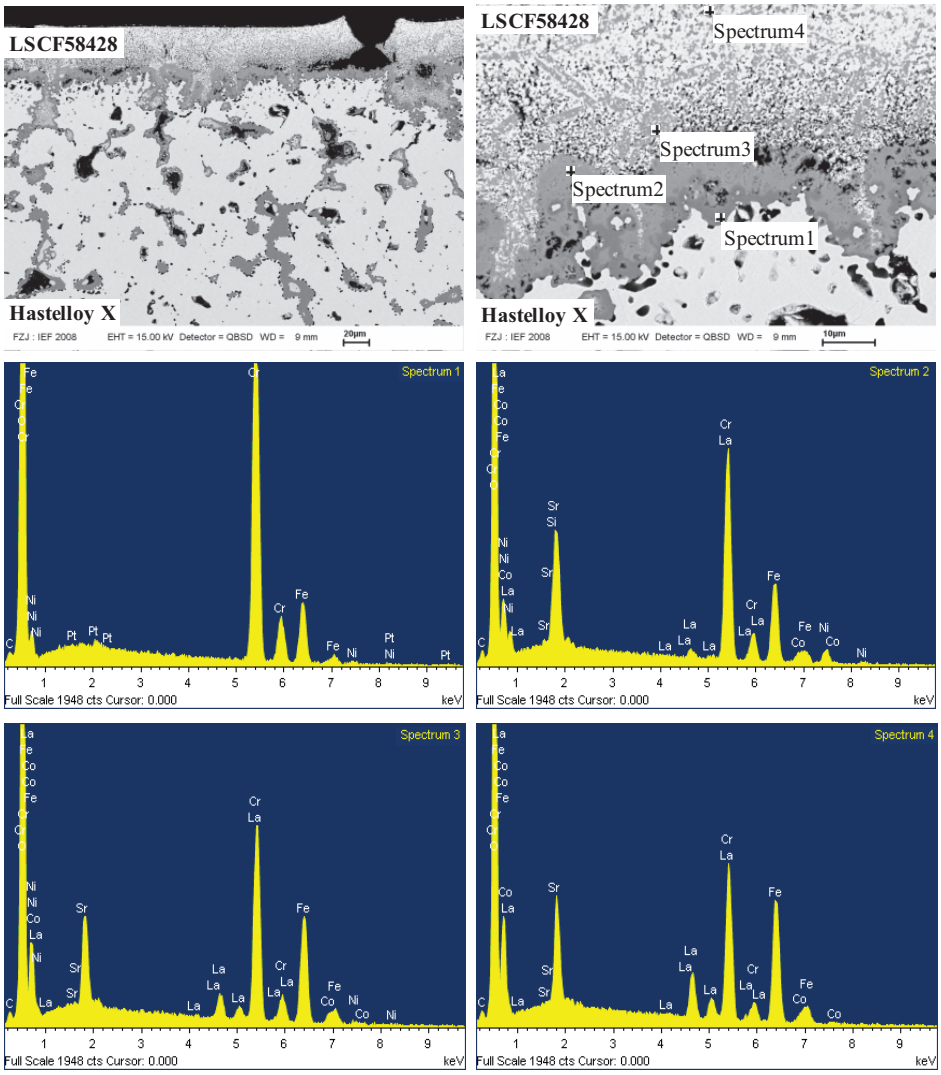

Figure 4.14: SEM images and EDS analyses of LSCF58428 screen printed layer on Hastelloy X after co-firing in air at 1200ºC for 5h

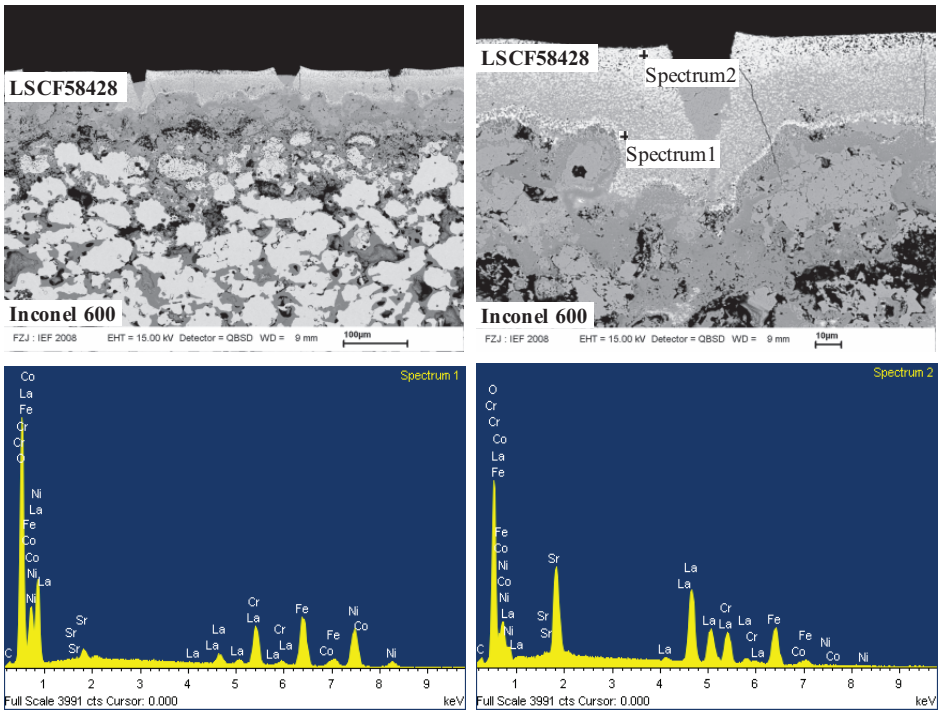

Figure 4.15: SEM images and EDS analyses of LSCF58428 screen printed layer on Inconel 600 after co-firing in air at 1200ºC for 5h

Figure 4.16 shows SEM images and EDS analyses of LSCF58428 screen-printed layer on Haynes 214 after co-firing at 1100°C for 5h in air. Similar to the Hastelloy X and Inconel 600 substrate, the surface layer with 1µm thickness of the Haynes 214 substrate consisted mainly of Cr and O (spectrum 1). The LSCF58428 layer of roughly 20µm was again not single-phase and consisted considerable amounts of Cr and Ni (spectrum 2 and spectrum 3). The surface-near region in the Haynes 214 substrate at the immediate interface consisted large amounts of Ni and Fe with minor amounts of Cr (spectrum 4) revealing that not only all Al but also most of the Cr was consumed by the formation of the oxide layer. Based on the above results and despite the fact that Haynes 214 has a certain Al content, Al was totally depleted in a short time when co-firing was carried out at 1100°C for 5h in air. It showed the same performance as classical chromia-scale alloys such as Hastelloy X and Inconel 600.

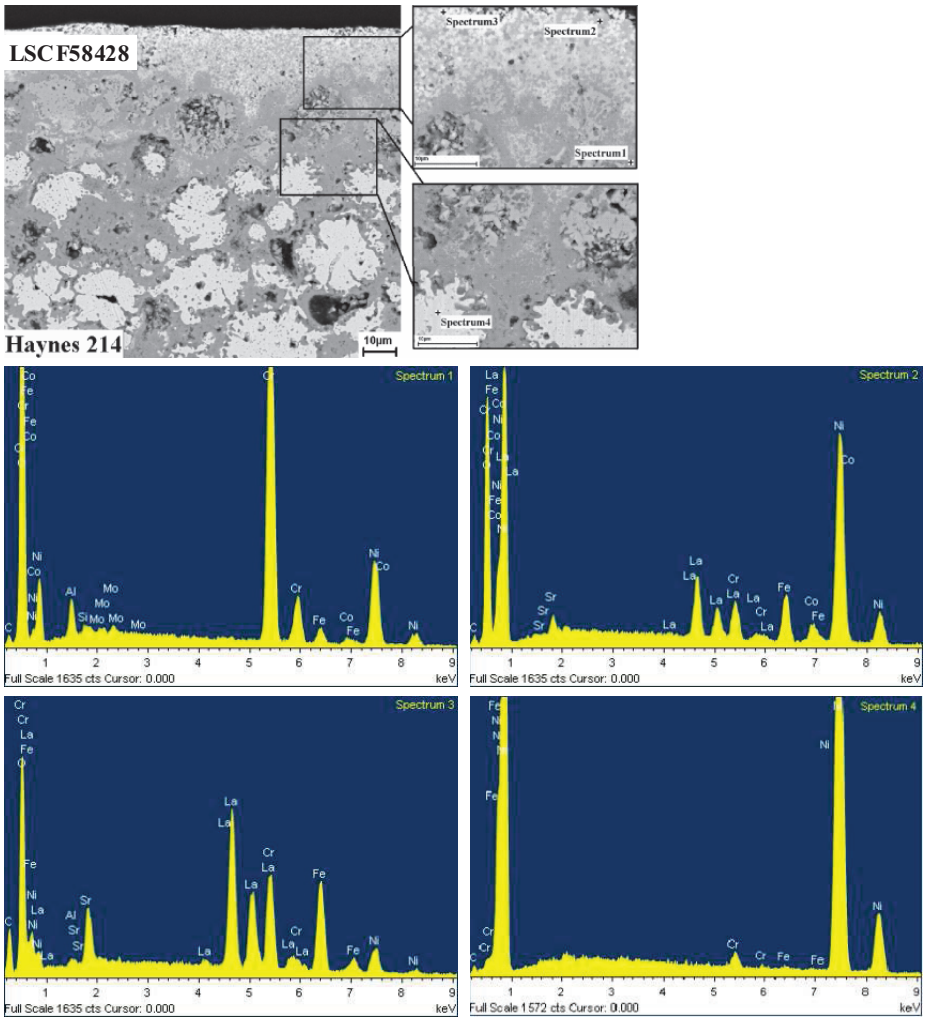

Figure 4.16: SEM images and EDS analyses of LSCF58428 screen printed layer on Haynes 214 after co-firing in air at 1100ºC for 5h

4.2.3 Alumina scale alloy

NiCoCrAlY is an alumina scale alloy, because of its high Al content (12.7%). Figure 4.17 shows SEM images and EDS analyses of LSCF58428 screen-printed layer on NiCoCrAlY after co-firing at 1200°C for 5h in air. The surface layer of the NiCoCrAlY substrate with a thickness of approx. 1µm consisted mainly of Al and O (spectrum 1), revealing the targeted alumina protection layer. On top of this layer, a reaction zone with a thickness of approx. 5µm formed with the LSCF58428 layer. It consisted of Sr, Al and O with minor amounts of Co (spectrum 2). The LSCF58428 layer of roughly 30µm consisted of La, Sr, Co, Fe and O with minor amounts of Al from the substrate (spectrum 3 and spectrum 4) and no second phase could be detected by the back-scattered SEM investigation.

Figure 4.18 shows SEM images and EDS analyses of BSCF5582 screen-printed layer on NiCoCrAlY after co-firing at 1120°C for 5h in air. The surface layer of the NiCoCrAlY substrate with a thickness of approx. 1µm consisted mainly of alumina with minor amounts of other elements, which are probably due to the limited lateral resolution of the EDS (spectrum 1). On top of this layer a double reaction zone were formed. A reaction zone consisted of Sr, Al and O plus minor amounts of Co was roughly 2µm thick (spectrum 2) and another reaction zone with a thickness of approx. 2µm consisted mainly of Ba, Sr, Al and O (spectrum 3). The BSCF5582 layer of approximately 30 µm consisted of Ba, Sr, Co and Fe (spectrum 4) while no element from NiCoCrAlY could be detected.

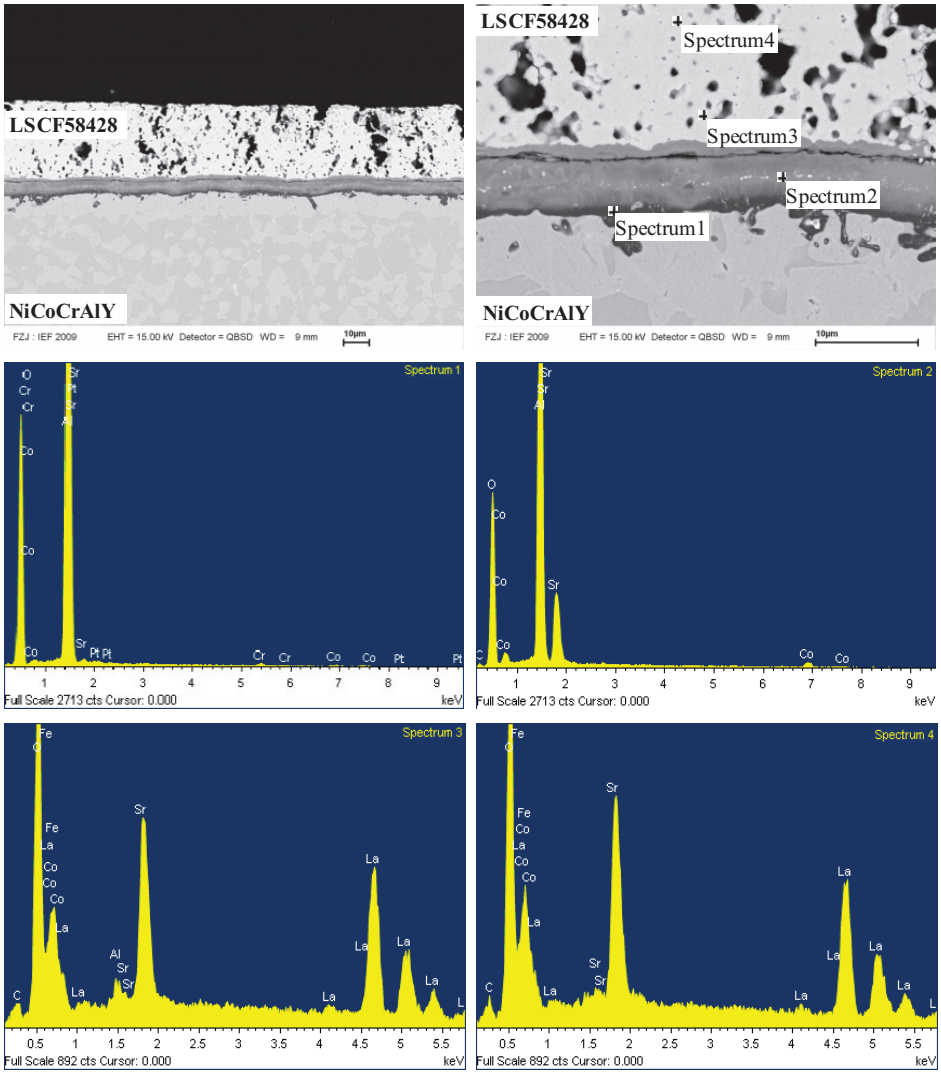

Figure 4.17: SEM images and EDS analyses of LSCF58428 screen printed layer on NiCoCrAlY after co-firing in air at 1200ºC for 5h

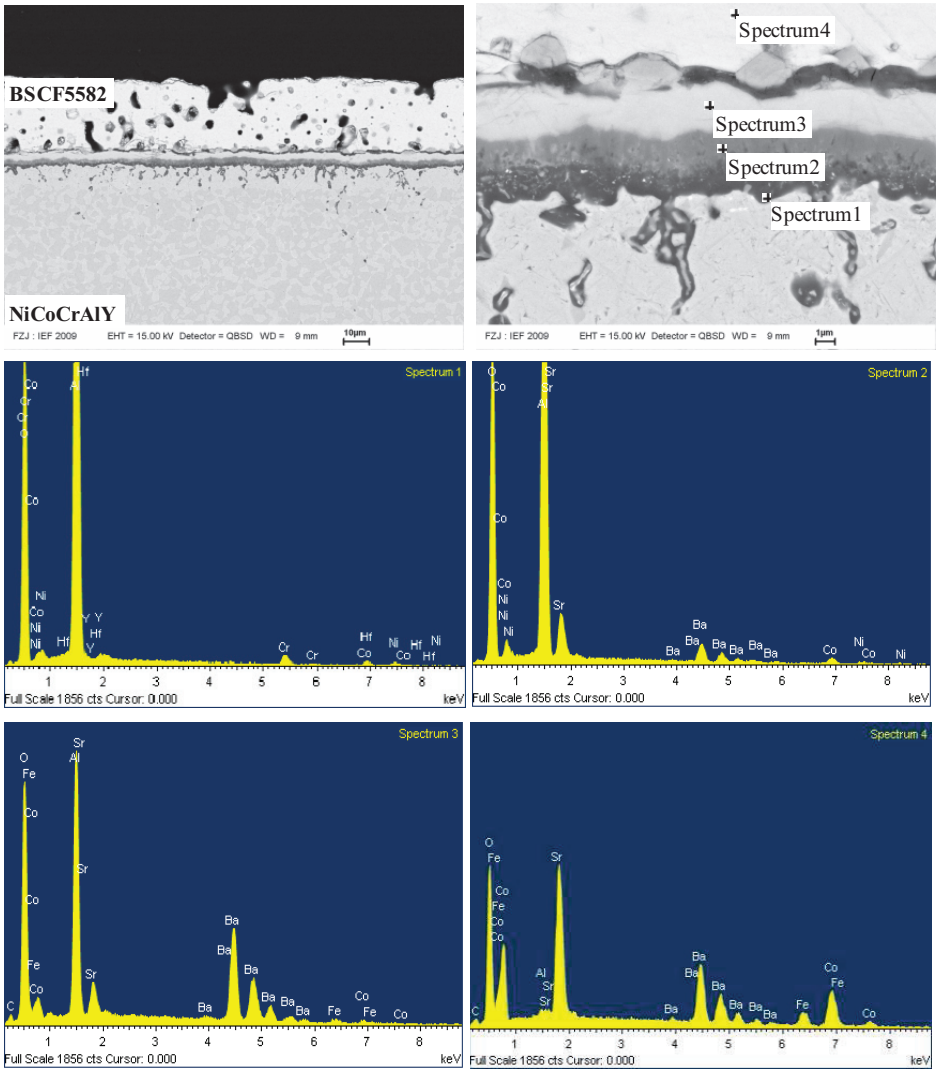

Figure 4.18: SEM images and EDS analyses of BSCF5582 screen printed layer on NiCoCrAlY after co-firing in air at 1120ºC for 5h

Phase compositions of the LSCF58428 layer with a NiCoCrAlY substrate and the BSCF5582 layer with a NiCoCrAlY substrate were investigated by XRD analysis after co-firing in air (Figure 4.19). They showed similar results, which were compared to

perovskite disks sintered alone in air (LSCF58428 at 1200°C for 5h and BSCF5582 at 1120°C for 5h). Four different phases could be detected in each case.

- The perovskite structure corresponded to LSCF58428 or BSCF5582.
- The monoclinic structure was attributed to the reaction zone. $SrAl_2O_4$ and $(Ba,Sr)Al_2O_4$ solid solution exhibit such a monoclinic structure at room temperature [FUK09, ITO77] and were consistent with EDS results.
- An additional trigonal phase could be identified, which was attributed to the alumina protection layer.
- The cubic structure belonged to the metallic phase in NiCoCrAlY.

No other phase was detected in the layer that would indicate severe decomposition and a subsequent loss in permeability.

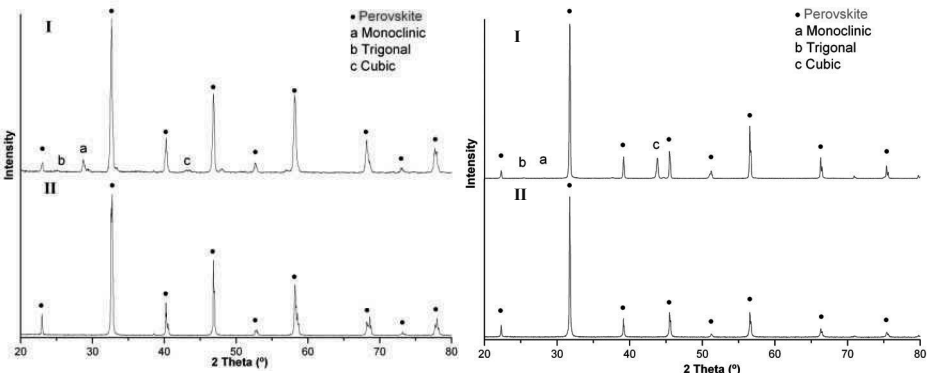

a) LSCF58428 b) BSCF5582

Figure 4.19: XRD patterns of LSCF58428 and BSCF5582 after high temperature heat treatment in air
I) Co-fired with NiCoCrAlY in air II) Sintered alone in air

Hence, NiCoCrAlY performed much better than Hastelloy X, Inconel 600 and Haynes 214. The alumina surface layer on NiCoCrAlY provided good protection against elemental diffusion (Ni and Cr) from NiCoCrAlY to perovskite materials. However, the impact of interdiffusion (Al into the perovskite membrane and Sr and Ba consumption for oxide formation) on the oxygen permeability has to be considered. Martynczuk et al. [MAR09] reported Al-doped $Ba_{0.5}Sr_{0.4}FeO_{3-\delta}$ (BSF). $Ba_{0.5}Sr_{0.5}Fe_{1-x}Al_xO_{3-\delta}$ shows the pure cubic perovskite phase in the range of x=0.09-0.1. The oxygen permeation increases with a rising Al content from 0 to 0.1 and decreases again for BSFA0.2 to values comparable to BSF. Ge et al. [GE07] investigated the A-site deficiency in BSCF5582. The A-site deficiency was found to have a negligible effect on the phase stability of BSCF5582 oxides under various oxygen partial pressure atmospheres. The A-site deficiency also led to increased permeation fluxes. For NiCoCrAlY-supported LSCF58428 or BSCF5582 layers, only small amounts of Al and Sr diffused. Thus, it can be expected that the oxygen permeation remains at a high level. Furthermore, a porous interlayer has to be introduced between the substrate and the membrane layer in order to bridge the highly porous substrate and the thin dense membrane layer. Thus, the reaction zone is hold in distance from the membrane surface. Mid-term exposure (350h) was carried out at 800°C in air after co-firing of the perovskite layer and the substrate. As shown in Figure 4.20, the reaction zone did not expand.

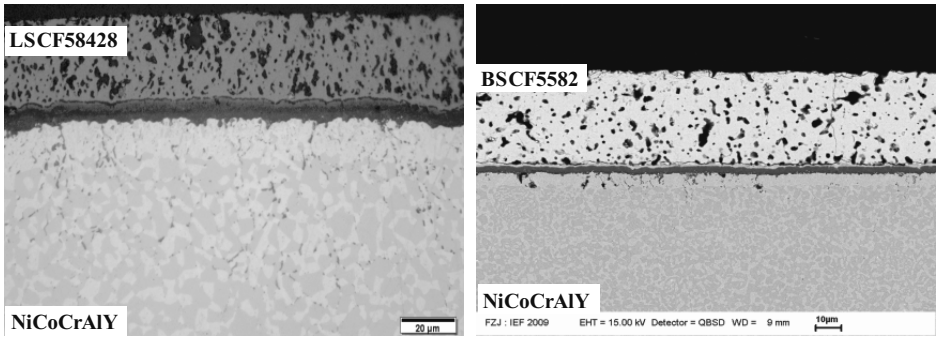

a) LSCF58428 b) BSCF5582

Figure 4.20: Cross section of screen printed layer on NiCoCrAlY after co-firing, then exposed at 800ºC for 350h in air

4.3 Porous NiCoCrAlY substrates

4.3.1 Substrate characterizations

Porous NiCoCrAlY substrates were manufactured by PLANSEE (PLANSEE SE, Reutte, Austria), which were sintered at different temperatures under the flowing H_2 atmosphere for 3h, i.e. 1150°C, 1200°C, 1225°C and 1250°C, which are named by NiCoCrAlY1150, NiCoCrAlY1200, NiCoCrAlY1225 and NiCoCrAlY1250. Figure 4.21 shows cross section microstructures of porous NiCoCrAlY substrates sintered at different temperatures. NiCoCrAlY1150 has just started the primary sintering behavior and most of particles still stayed spherically and NiCoCrAlY1200 has formed considerable sintering necks. NiCoCrAlY1225 and NiCoCrAlY1250 showed obvious sintering effects, but they still had open porous structure.

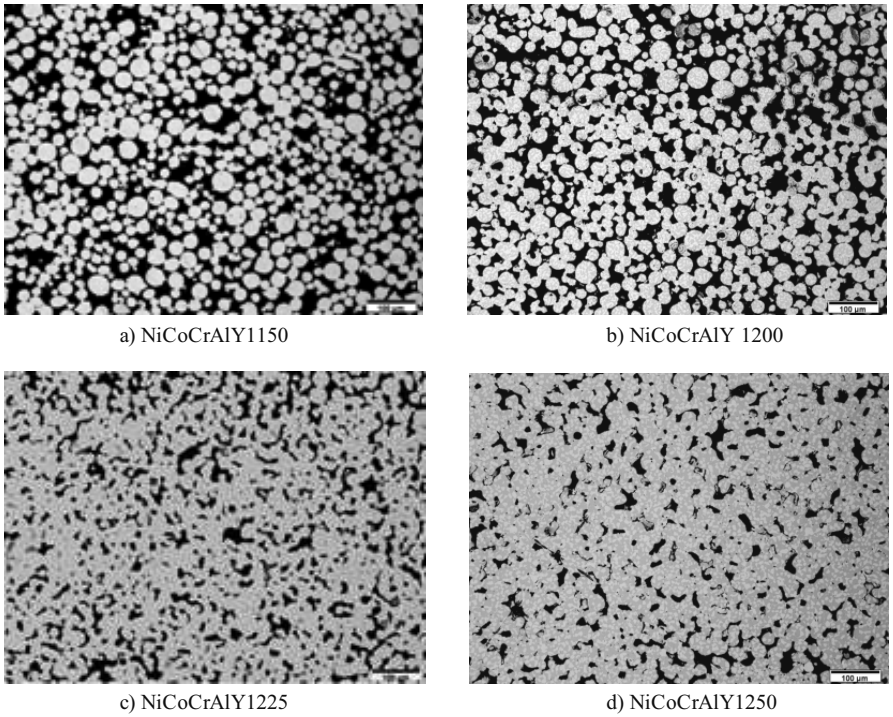

a) NiCoCrAlY1150 b) NiCoCrAlY 1200

c) NiCoCrAlY1225 d) NiCoCrAlY1250

Figure 4.21: Cross section microstructures of porous NiCoCrAlY substrates sintered at different temperatures

Table 4.4 gives mercury intrusion measurement results of porous NiCoCrAlY substrates. As the sintering temperature increased from 1150°C to 1250°C, the porosity of substrate decreased from 38.7% to 20.0%.

Table 4.4: Mercury intrusion measurement results of porous NiCoCrAlY substrates

Substrate	Sintering temperature (°C)	Porosity (%)
NiCoCrAlY1150	1150	38.7
NiCoCrAlY1200	1200	35.4
NiCoCrAlY1225	1225	25.6
NiCoCrAlY1250	1250	20.0

The gas flow permeability of porous NiCoCrAlY substrates was measured with nitrogen at room temperature. The results are given in Figure 4.22. NiCoCrAlY1150 showed extremely high nitrogen flow rate due to the low sintering effect. The nitrogen flow rate decreased when higher sintering temperatures were carried out. Flow rates of ceramic substrates reported by Betz [BET10] are given for comparison, which are considered to be sufficient as asymmetric membrane substrate. LSCH substrate was fabricated with the mixture of LSCF58428 and CGO by Tape Casting and LCM substrate was fabricated with the mixture of LSCF58428 and CGO by CoatMix. NiCoCrAlY1200 and NiCoCrAlY1225 showed similar flow rates as the given ceramic substrates. NiCoCrAlY1250 showed a very low flow rate which is insufficient as the porous substrate.

As the substrate of the asymmetric membrane structure, a sufficient gas flow permeability based on a reasonable open porosity is required. However, the large surface area due to the high porosity will lead to a poor corrosion resistance and a low mechanical strength. Therefore, appropriate sintering temperature for substrate fabrication plays an important role for the application.

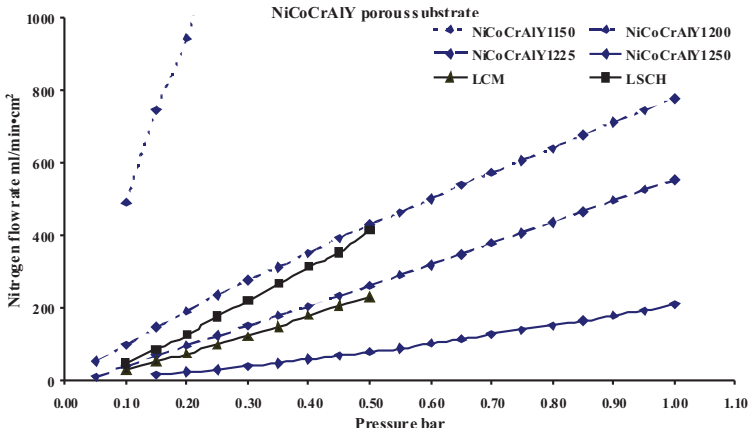

Figure 4.22: Nitrogen flow permeability of different substrates. LCM substrate was fabricated with the mixture of LSCF and CGO by CoatMix and LSCH substrate was fabricated with the mixture of LSCF and CGO by Tape Casting [BET10]

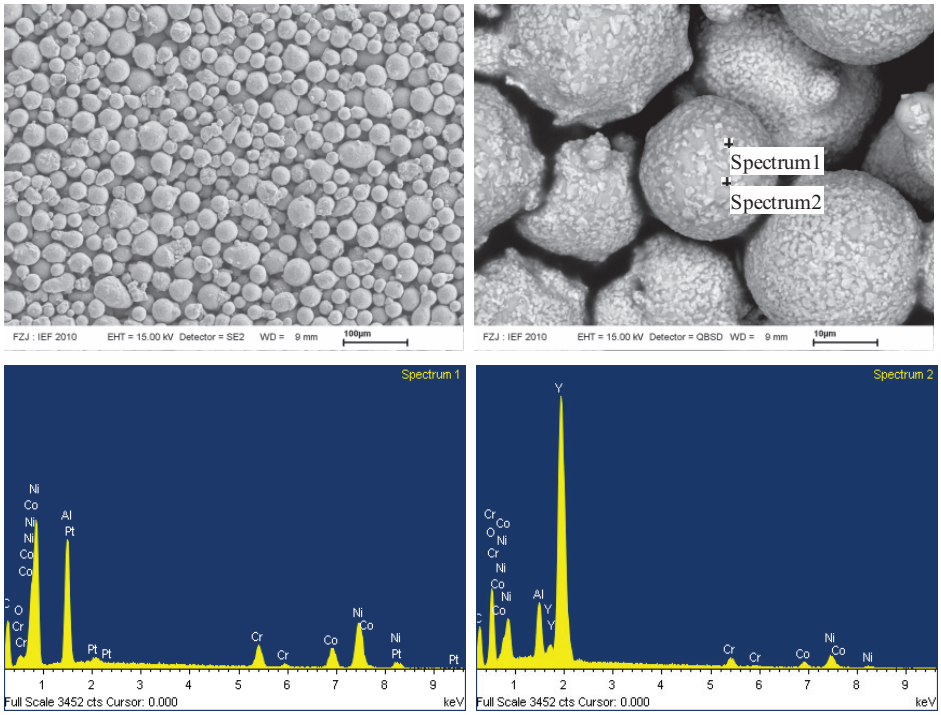

Figure 4.23: SEM images and EDS analyses on the surface of the porous NiCoCrAlY1150 substrate

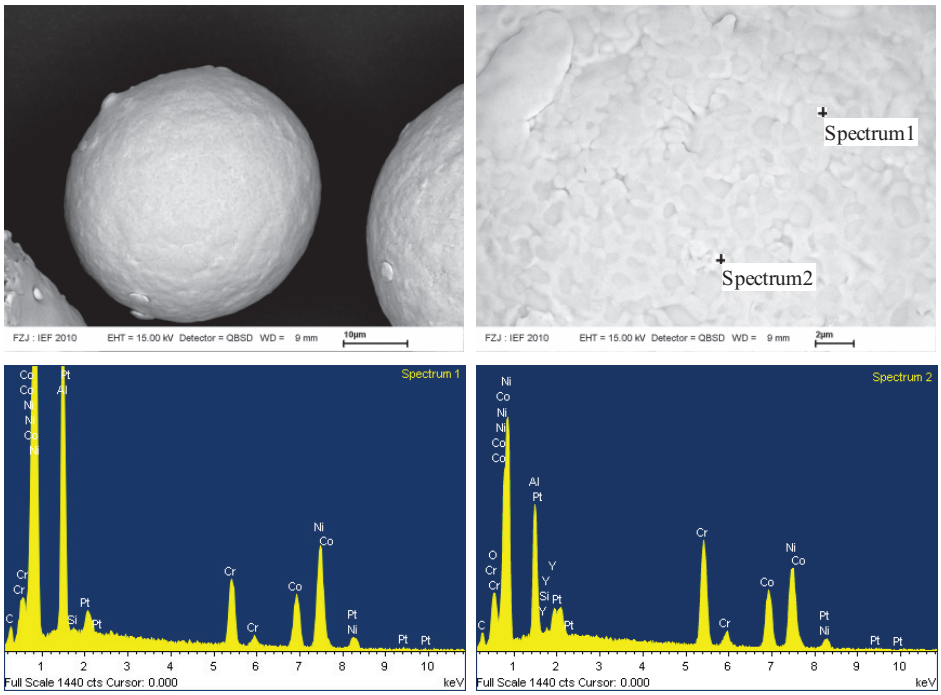

Figure 4.24: SEM images and EDS analyses of the NiCoCrAlY powder

Figure 4.23 shows SEM images and EDS analyses on the surface of the porous NiCoCrAlY1150 substrate. Alumina surface layer was found based on spectrum 1 and white islands rich of Y appeared based on spectrum 2. In order to find out the reasons of Y-rich phase appearance, the metallic powder applied for porous NiCoCrAlY substrate manufacture was investigated. Figure 4.24 shows SEM images and EDS analyses. From the surface morphology of the powder, the islands were not observable. In spectrum 1 and spectrum 2 the Y rich area has not been found. Therefore, the Y-rich phase resulted from the flowing H_2 atmosphere during substrate sintering. When H_2 was flowed into furnace continuously, small amounts of oxygen and water vapor with hydrogen was brought into the atmosphere slowly, which resulted in a certain P_{O_2}. Due to the very high affinity of Y to oxygen Y-rich phase formed. When Y is depleted or has not enough time to diffuse to the surface, aluminum starts to oxidize.

4.3.2 Oxidation behavior of the porous substrate in co-firing conditions

The oxidation resistance of NiCoCrAlY material is achieved by the formation of a thin Al_2O_3 layer on the surface. The Al in the Al-rich ß phase is consumed by Al_2O_3 formation on the surface, producing aluminum depletion zones that increase with time and temperature. When the ß phase is completely consumed and the Al concentration reaches a critical minimum other oxides like Cr_2O_3 and/or spinals may form besides the protective alumina, leading to internal oxidation. The time, when the ß phase is completely consumed is assumed as a material lifetime end [KRU04]. The oxidation resistance of a porous substrate is much lower than the bulk material due to the much higher exposed surface area. However, they have the same oxidation resistance mechanism.

The surface protection layer of NiCoCrAlY is called thermally growth oxide (TGO), which primarily consists of Al_2O_3. Beck [BEC08] gives the equation (Equation 4.1) for the description of TGO growth kinetics of NiCoCrAlY. d_{TGO} is the thickness of TGO and t is the exposure time. n is the oxidation exponent. C is the pre-factor and Q is the activation energy. R is the universal gas constant. T is the exposure temperature.

$$d_{TGO} = t^n \cdot C \cdot \exp\left(-\frac{Q}{RT}\right) \tag{4.1}$$

The thickness of TGO on the dense NiCoCrAlY compact was measured in this study from temperature 1050°C to 1200°C for 1 to 7 hours. Home-made dense NiCoCrAlY compacts were manufactured by loose powder sintering at 1200°C for 5h under (4%H_2)/Ar atmosphere and applied for the measurements.

Figure 4.25 shows the graphs based on the Equation 4.1 for each temperature and the measured values, which gives the TGO thickness corresponding to each exposure temperature and time. The value of activation energy Q was given by the literature [BEC08]. The chosen values for pre-factor C and oxidation exponent n in Equation 4.1 bring in the good fitting with the measured values. Table 4.5 gives the chosen values of pre-factor C, activation energy Q and the oxidation exponent n for each temperature. According to graphs, the thickness of TGO can be predicted by a given exposure temperature and time.

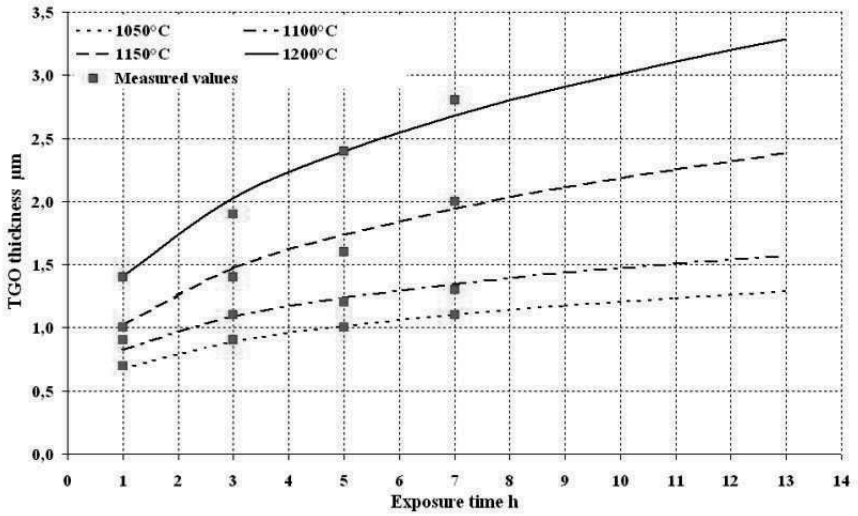

Figure 4.25: TGO thicknesses at various temperatures and time based on the Equation 4.1 and the measured values.

Table 4.5: The pre-factor C, activation energy Q and oxidation exponent n in Equation 4.1

Exposure temperature	n	C (µm/h^n)	Q (J/mol)*
1050°C	0.25	0.682	87.575
1100°C	0.25	0.835	87.575
1150°C	0.33	1.030	87.575
1200°C	0.33	1.420	87.575

* The value of Q is from [BEC08]

The growth of TGO with the exposure time leads to an Al depletion zone adjacent to the surface. If no aluminium content is assumed in the Al depletion, the thickness of the Al depletion zone can be calculated with the TGO thickness in Equation 4.2 and 4.3. Wt% is the weight percent of Al content in NiCoCrAlY (12.7%). M_{Al} and M_O are the atomic weight of Al (27.0 g/mol) and O (16.0 g/mol). d_{TGO} is the thickness of TGO. d_D is the thickness of the depletion zone. $\rho_{Al_2O_3}$ (4.0 g/cm^3) and ρ_{Ni} (7.9 g/cm^3 [DOL02]) are theoretical densities of alumina and NiCoCrAlY. d is the diameter of the sphere particle.

For a endless plate (dense compacts),

$$Wt\,\% = \left(\frac{2 \times M_{Al}}{2 \times M_{Al} + 3 \times M_O} \right) \bullet \frac{d_{TGO} \cdot \rho_{Al_2O_3}}{d_D \cdot \rho_{Ni}} \tag{4.2}$$

For a sphere particle,

$$Wt\,\% = \left(\frac{2 \times M_{Al}}{2 \times M_{Al} + 3 \times M_O} \right) \bullet \frac{4\pi \left(\frac{d}{2} \right)^2 \cdot d_{TGO} \cdot \rho_{Al_2O_3}}{\frac{4}{3}\pi \left(\frac{d}{2} \right)^3 \rho_{Ni}} \tag{4.3}$$

Dense NiCoCrAlY compacts carried out in the study are considered as endless plates. The Al depletion zone thickness of dense compacts after the exposure at various temperatures and time were measured, which was compared with calculated results based on Equation 4.2 in Figure 4.26. When the TGO thickness was smaller than 1.5µm, measured values fitted calculated values pretty well. But for the large TGO thickness measured values were higher than calculated values. In the calculation the entire Al content was assumed for the oxidation layer formation. However, even in the Al depletion zone some amounts of Al still exist. Therefore, larger Al depletion zone was created in the actual situation than the calculation due to the TGO growth. Porous NiCoCrAlY substrates for the asymmetric membrane structure were poorly sintered from the metallic powder, which could be assumed as the sphere particle model. Figure 4.27 shows the TGO thickness based on the calculation for a sphere particle, which gives the required particle size for the corresponding TGO thickness. Figure 4.28 gives the particle size distribution of the NiCoCrAlY powder. The particle size of d_{10}=20.5µm was applied for the estimation, which ensured that most of the particles were large than it, which corresponds to 1.6µm TGO thickness. Hence, the TGO thickness on the surface of the porous substrate should not exceed 1.6µm, otherwise the Al content in some regions of the material will be depleted. According to the Figure 4.25, if the temperature is 1150°C or even higher, the TGO will grow to 1.6µm in very short time (<4h). While the temperature is 1100°C or even lower, the TGO thickness will keep under 1.6µm in much longer time (>13h).

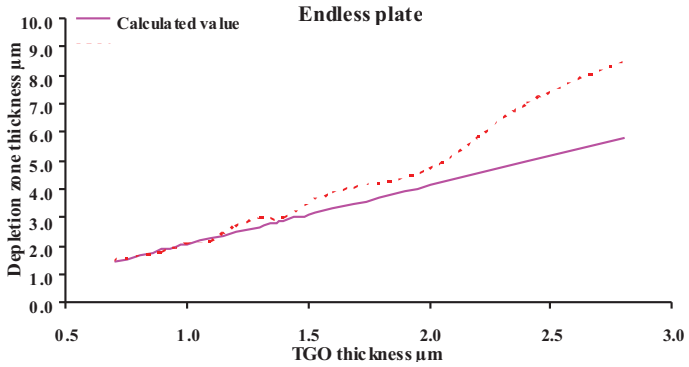

Figure 4.26: Depletion zone thickness based on the calculation (Equation 4.2) and measurements for endless plate

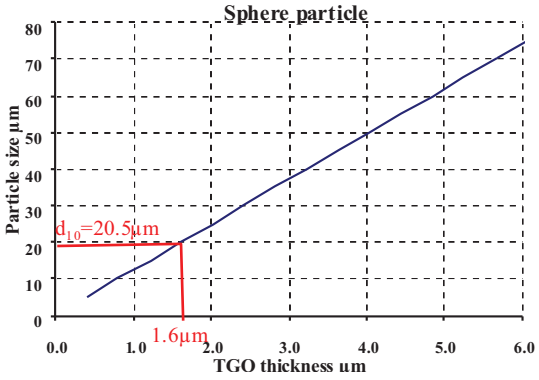

Figure 4.27: TGO thickness based on the calculation (Equation 4.3) for sphere particle

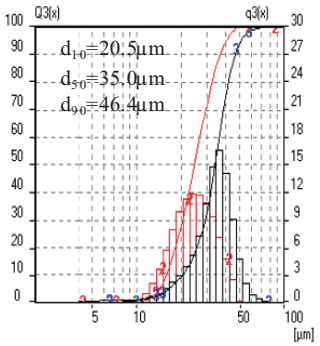

Figure 4.28: Particle size distribution of NiCoCrAlY powder

NiCoCrAlY1150 obtained a very poor mechanical strength due to the poor sintering effect. Therefore, higher sintering temperatures are needed, which lead to lower specific surface area and, hence, longer life time in co-firing conditions can be expected. NiCoCrAlY1225, which was sintered at 1225°C in H_2, was chosen as the substrate in the asymmetric membrane structure. The substrate was co-fired with coated interlayers together at high temperature in air. According to the above investigation, the co-firing temperature was chosen at 1100°C.

4.4 Interlayer development

The particle size distribution of the NiCoCrAlY powder is shown in Figure 4.28 revealing d_{10}=20.5µm, d_{50}=35.0µm and d_{90}=46.4µm. Surface pores of NiCoCrAlY1225 substrates are approximately 30µm-50µm analyzed by SEM. Therefore, the interlayer development on the substrate is necessary to provide a proper surface quality for the deposition of a dense thin film membrane layer. Screen printing is chosen as the coating technique.

4.4.1 Screen printing paste optimization

The interlayer was coated on the NiCoCrAlY1225 substrate by screen printing. The paste of screen printing plays an important role on the interlayer. Two kinds of solvent and binder combination (terpineol/ethylcellulose and BCA/Mowital SB 20H) were applied for the paste manufacture and in some cases the dispersant FX9086 was added. The combination of terpineol and ethylcellulose in screen printing paste has been reported for the LSCF58428 pastes [BÜC07]. However, the combination of BCA, Mowital SB 20H and FX 9086 with high specific surface area LSCF58428 powder showed better performance [SCH09b, SUR09]. The powder content in the paste was varied in order to find the best combination. The standard LSCF58428 powder was calcined at 900°C called 900LSCF58428. In order to reduce the specific surface area, LSCF58428 powder was further calcined at 1200°C, which is called 1200LSCF58428 powder. After ball milling, particle size distributions of both powders were measured shown in Figure 4.29 revealing similar distributions. However, Figure 4.30 shows that primary particles of 900LSCF58428 are much smaller and the surface area of the powder was reduced by high temperature calcination obviously, which is beneficial for obtaining the high green density paste, because it is easier to disperse. Specific surface areas of both powders were measured by BET. The 900LSCF58428 powder has 8.1m^2/g and 1200LSCF58428 powder has 5.4m^2/g. Table 4.6 and Table 4.7 show the mixture of manufactured pastes and weight percent of each component.

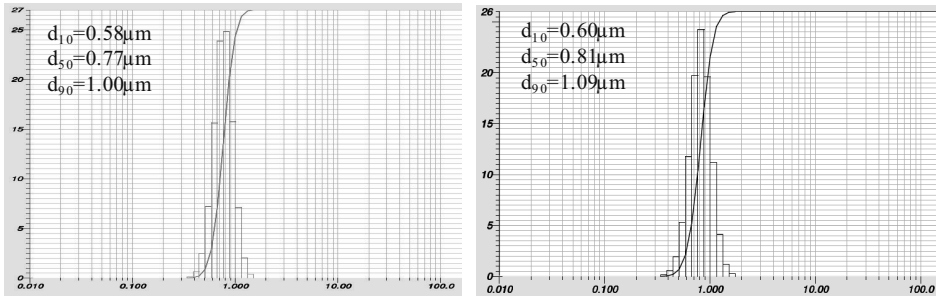

a) 900LSCF58428 powder b) 1200LSCF58428 powder

Figure 4.29: Particle size distributions of LSCF58428 powder after ball milling

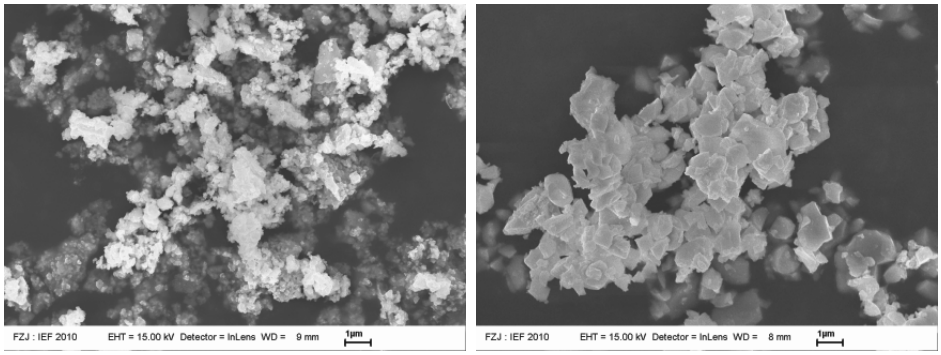

a) 900LSCF58428 powder b) 1200LSCF58428 powder

Figure 4.30: SEM images of LSCF58428 powder

Table 4.6: Mixture of screen printing pastes

Paste name	Ceramic Powder	Powder calcination T	Solvent	binder	Dispersant
900LSCF60%_T	900LSCF	900°C	terpineol	ethylcellulose	~
900LSCF60%_TF	900LSCF	900°C	terpineol	ethylcellulose	FX 9086
900LSCF60%_BF	900LSCF	900°C	BCA	Mowital SB 20H	FX 9086
900LSCF65%_BF	900LSCF	900°C	BCA	Mowital SB 20H	FX 9086
1200LSCF60%_T	1200LSCF	1200°C	terpineol	ethylcellulose	~
1200LSCF65%_BF	1200LSCF	1200°C	BCA	Mowital SB 20H	FX 9086
1200LSCF70%_BF	1200LSCF	1200°C	BCA	Mowital SB 20H	FX 9086
1200LSCF75%_BF	1200LSCF	1200°C	BCA	Mowital SB 20H	FX 9086

Table 4.7: Composition of screen printing pastes wt%

Paste name	Ceramic Powder	Solvent	Binder	Dispersant
900LSCF60%_T	60%	37.6%	2.4%	~
900LSCF60%_TF	60%	35.8%	2.4%	1.8%
900LSCF60%_BF	60%	35.8%	2.4%	1.8%
900LSCF65%_BF	65%	30.4%	2.6%	2.0%
1200LSCF60%_T	60%	37.6%	2.4%	~
1200LSCF65%_BF	65%	30.4%	2.6%	2.0%
1200LSCF70%_BF	70%	25.1%	2.8%	2.1%
1200LSCF75%_BF	75%	19.7%	3.0%	2.3%

Rheological behaviors of pastes were evaluated. Figure 4.31 shows viscosities of pastes made from 900LSCF58428 powder at 20°C (screen printing was carried out at room temperature) and 60°C (the drying temperature for the screen printed layer). For the high surface area powder 900LSCF58428 the dispersant reduced the viscosity of the terpineol-based paste significantly at 60°C and low shear rates correspond to the drying conditions. However, using BCA as the solvent is even more effective also at 20°C and high shear rates correspond to the printing process. The viscosity remained at a low level even when the powder content is increased from 60% to 65%.

Figure 4.32 shows the trends for the low surface area powder 1200LSCF58428. Similar to 900LSCF58428 BCA-based pastes showed lower viscosity though higher powder content, i.e. 65% and 70%. However, a further increase in the powder content again led to an increase in the viscosity.

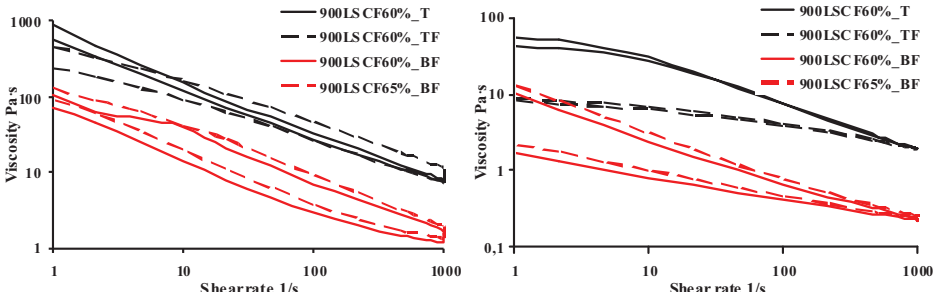

a) at 20°C b) at 60°C

Figure 4.31: Viscosities of the manufactured pastes made from 900LSCF58428 powder

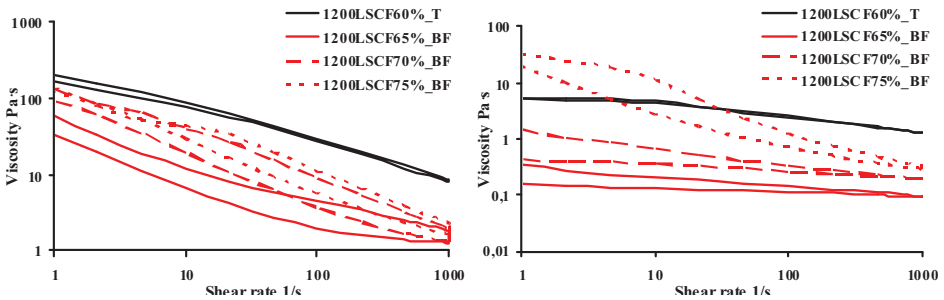

a) at 20°C b) at 60°C

Figure 4.32: Viscosities of manufactured pastes made from 1200LSCF58428 powder

Flow limits of manufactured pastes were additionally measured. Materials flow only after the shear stress becomes equal or bigger than the flow limit. During the screen printing, the paste is squeezed through a sieve and exerted by a shear stress. The layer surface showed the structure of the sieve. If the flow limit of paste is very low, the screen printed paste can recover from the structure of the sieve by itself leading to a smooth surface. If the flow limit is relatively high, the structure of sieve will remain on the layer surface. Surface quality of screen printed layer is another important property. The high roughness of the surface leads to a high risk of defects, which should be avoided.

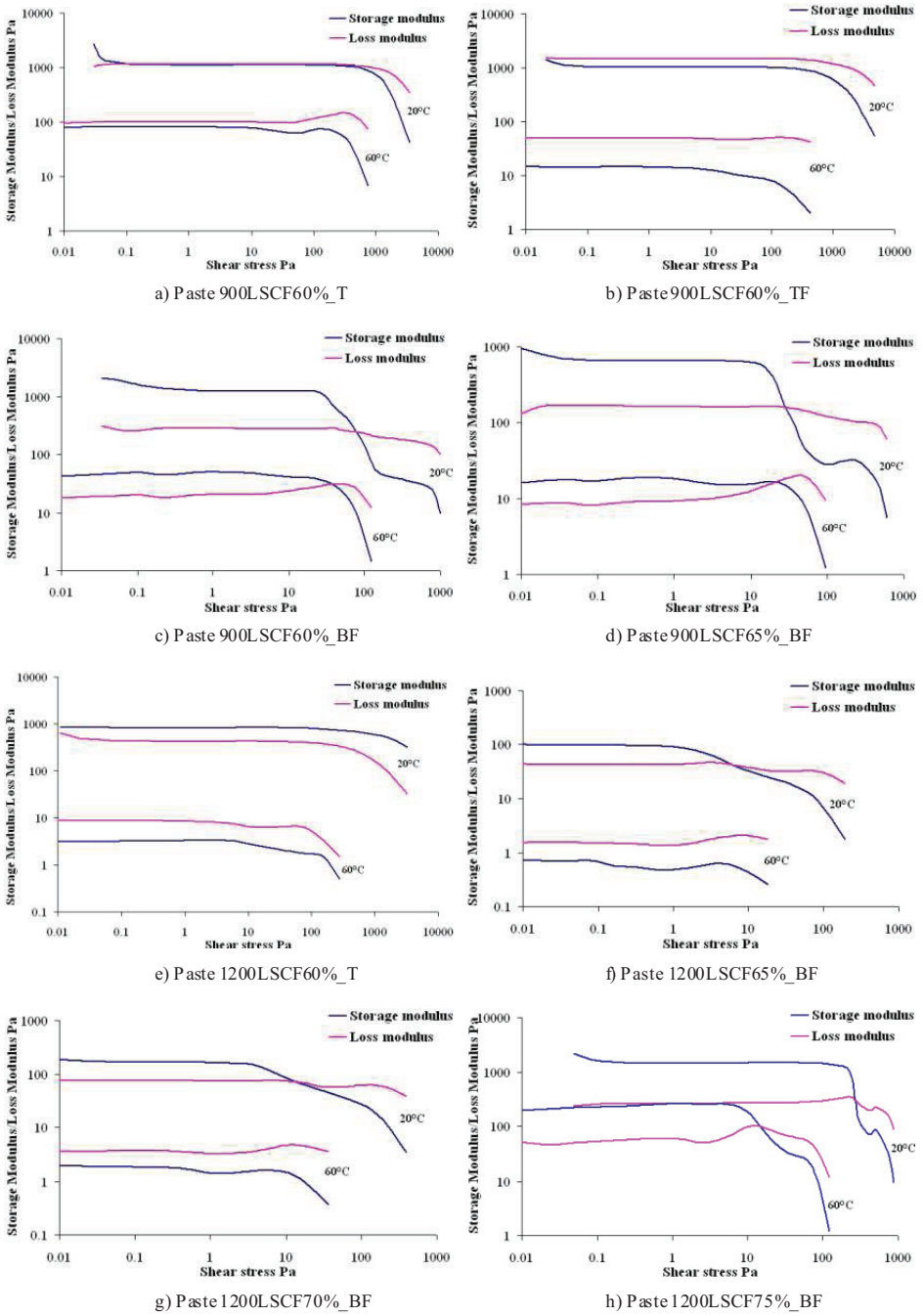

a) Paste 900LSCF60%_T

b) Paste 900LSCF60%_TF

c) Paste 900LSCF60%_BF

d) Paste 900LSCF65%_BF

e) Paste 1200LSCF60%_T

f) Paste 1200LSCF65%_BF

g) Paste 1200LSCF70%_BF

h) Paste 1200LSCF75%_BF

Figure 4.33: Storage modules and loss modules of manufactured pastes

Figure 4.33 shows storage modules and loss modules of manufactured pastes. Storage modulus indicates the stress energy temporarily stored during the deformation and loss modulus indicates the energy which has been used to initiate flow (Chapter3.4.9). The intersection of storage modulus and loss modulus is the flow limit of the paste. Paste 900LSCF60%_T and 900LSCF60%_TF showed flow limits at 20°C, but they didn't occur at 60°C. For pastes 900LSCF60%_BF and 900LSCF65%_BF, flow limits occurred at both temperatures. Pastes made from the low specific surface area powder 1200LSCF58428, 1200LSCF60%_T, 1200LSCF65%_BF and 1200LSCF70%_BF, didn't show flow limits at 60°C. But 1200LSCF75%_BF again showed flow limits at 20°C and 60°C. When the paste doesn't have flow limit at 60°C, it means that the layer surface can recover from the structure of the sieve during drying at 60°C, which is the desired situation.

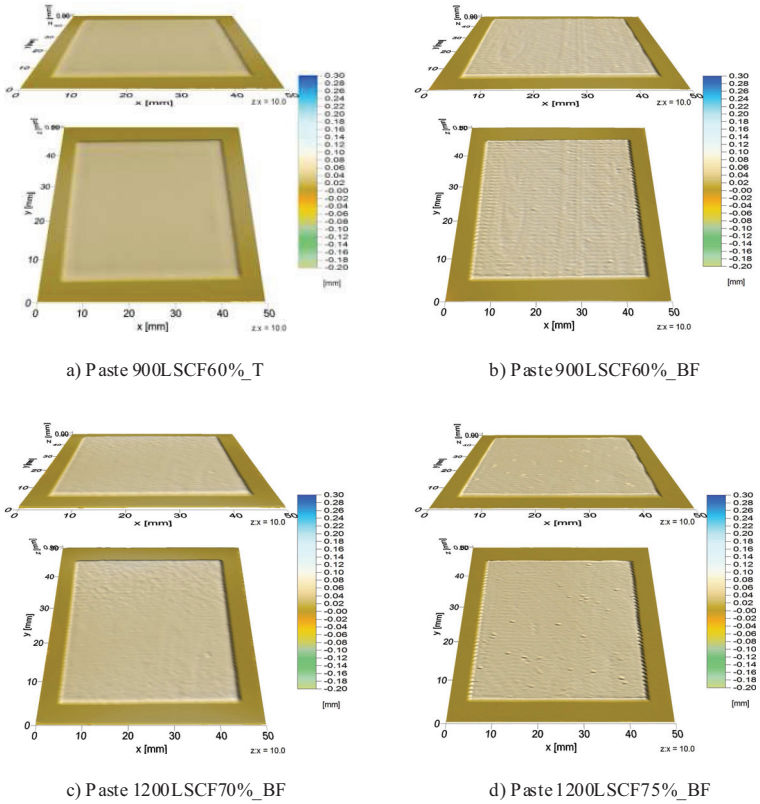

a) Paste 900LSCF60%_T

b) Paste 900LSCF60%_BF

c) Paste 1200LSCF70%_BF

d) Paste 1200LSCF75%_BF

Figure 4.34: Surface topographies of the screen printed layer with different pastes after drying at 60°C

The surface topographies of different pastes (Figure 4.34) were investigated, which were firstly screen printed on a polished steel substrate and dried at 60°C. Paste 900LSCF60%_T and 1200LSCF70%_BF showed the smooth surface after drying and paste 900LSCF60%_BF and 1200LSCF75%_BF didn't recover from the structure of the sieve, which is in agreement with flow limit measurements. Therefore, two pastes made from the high specific surface area powder, 900LSCF60%_T and 900LSCF60%_TF, and three pastes made from the low specific surface area powder, i.e. 1200LSCF60%_T, 1200LSCF65%_BF and 1200LSCF70%_BF, avoided the occurrence of the flow limit at 60°C.

Green densities of the screen printed layer with different pastes were measured. Values are given in Table 4.8. For pastes made from the low specific surface area powder terpineol-based paste using the dispersant showed the highest green density. In contrast, for pastes made from the low specific surface area powder BCA-based pastes obtained higher green densities. The green density increased as the ceramic powder content increased until 70% obtaining a maximum value of 61.6% of the theoretical density. A further increase of the powder content reduced again the green density, which is due to the sharp increase in the viscosity and the occurrence of a flow limit as shown in Figure 4.32 and 4.33h.

Table 4.8: Green densities of manufactured pastes

Paste name	Powder content	Solvents	binder	Dispersant	Green density/ theoretical density
900LSCF60%_T	60%	terpineol	ethylcellulose	~	51.7%
900LSCF60%_TF	60%	terpineol	ethylcellulose	FX 9086	56.8%
900LSCF60%_BF	60%	BCA	Mowital SB 20H	FX 9086	48.9%
900LSCF65%_BF	65%	BCA	Mowital SB 20H	FX 9086	50.6%
1200LSCF60%_T	60%	terpineol	ethylcellulose	~	58.2%
1200LSCF65%_BF	65%	BCA	Mowital SB 20H	FX 9086	60.5%
1200LSCF70%_BF	70%	BCA	Mowital SB 20H	FX 9086	61.6%
1200LSCF75%_BF	75%	BCA	Mowital SB 20H	FX 9086	53.8%

According to rheological investigations and green density measurements of manufactured pastes, paste 900LSCF60%_TF had a relative low viscosity, avoided the flow limit at 60°C and showed the highest green density among pastes made from the high specific surface area powder. Similarly, paste 1200LSCF70%_BF showed the best performance among pastes made from the low specific surface area powder. Both pastes are applied for the interlayer development.

Figure 4.35 shows microstructures of the free-stand screen printed layer with paste 900LSCF60%_TF and paste 1200LSCF70%_BF after the heat treatment at pre-defined firing conditions 1100°C for 5h. The screen printed layer with paste 900LSCF60%_TF showed a denser structure than the layer with paste 1200LSCF70%_BF. This is due to a reduced sintering activity caused by the high temperature calcination. The combination of a high green density and a low sintered density leads to a very low shrinkage rate. This is favorable because it reduces the shrinkage mismatch with the non-shrinking metallic substrate lowering the risk of a crack formation.

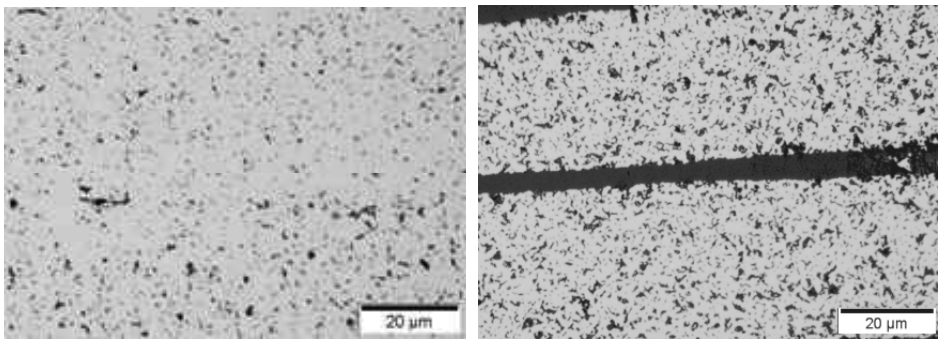

a) Paste 900LSCF60%_TF b) Paste 1200LSCF70%_BF

Figure 4.35: Microstructures of the free-stand screen printed layer after heat treatment at 1100°C for 5h

4.4.2 Interlayer fabrication

The interlayer was coated by screen printing on the porous NiCoCrAlY1225 substrate. The high green density screen printing paste can reduce the internal stress which is brought from the shrinkage mismatch of the interlayer and the substrate during co-firing. Paste 1200LSCF70%_BF had a green density of 61.6% of theoretical density, which was screen printed on NiCoCrAlY1225 and co-fired at 1100°C for 5h. It was compared with paste 900LSCF60%_TF, which had a green density of 56.8% of theoretical density and a higher sintering density than paste 1200LSCF70%_BF. Figure 4.36 shows surface images of screen printed layer after the co-firing in air. The cracks appeared on the surface, but the higher green density paste reduced the size of cracks from ~15µm to ~3µm. Although the cracks have not been removed, the surface quality is appropriate for coating a second interlayer. Figure 4.37 shows the surface and cross section images of the 1200LSCF58428 first interlayer after co-firing at 1100°C for 5h in air in more detail. The layer was firstly screen printed with a wet layer thickness (WLT) 100µm sieve and dried at 60°C. Then it was screen printed again with a WLT 19µm sieve. Finally it was co-fired at 1100°C for 5h in air. Because pores on the surface of the substrate were very large (30-50µm), the first screen printed paste was almost completely infiltrated into pores. The second coating was necessary to form the integrated layer.

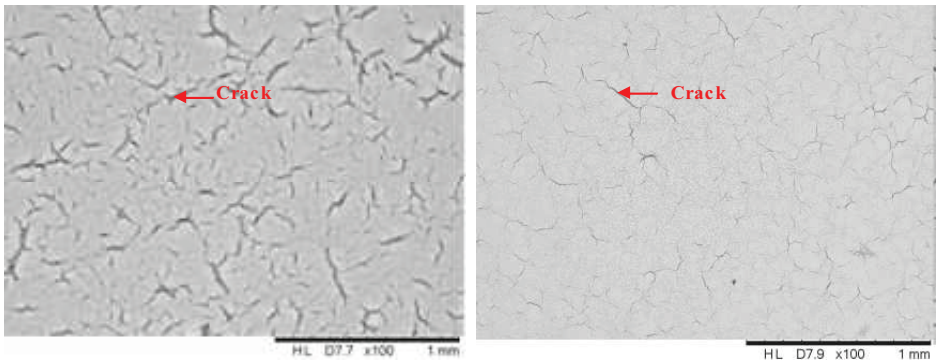

a) Paste 900LSCF60%_TF b) Paste 1200LSCF70%_BF

Figure 4.36: Surface images of the screen printed layer coated with different pastes and co-fired at 1100°C for 5h in air

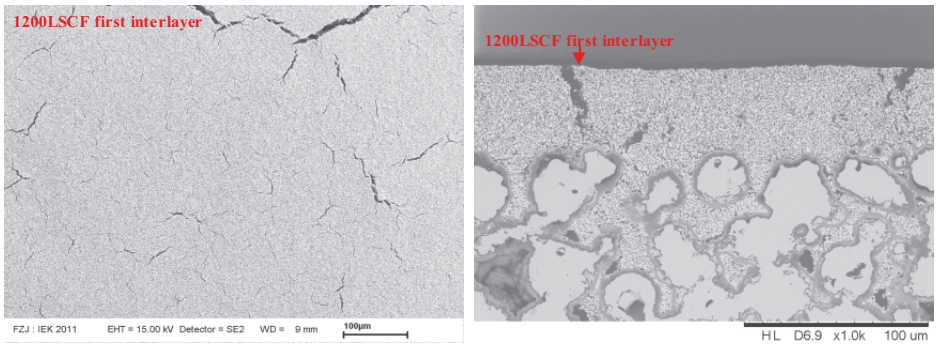

a) Surface image b) Cross section image

Figure 4.37: SEM images of the1200LSCF58428 first interlayer after co-firing at 1100°C for 5h in air

Paste 900LSCF60%_TF was screen printed on the 1200LSCF58428 first interlayer with a WLT 43µm sieve as the second interlayer then co-fired again at 1100°C for 5h in air. Figure 4.38 shows SEM images of the sample with both interlayers on the substrate. Figure 4.38a and b give surface images with different magnifications. Figure 4.38c and d give cross section images. On surface images and cross section images cracks have not been found in the second interlayer, but the 900LSCF58428 second interlayer still had a large porosity. In Figure 4.38c the border between two interlayers was obvious and it was seen that the crack from the first interlayer was covered by the second interlayer.

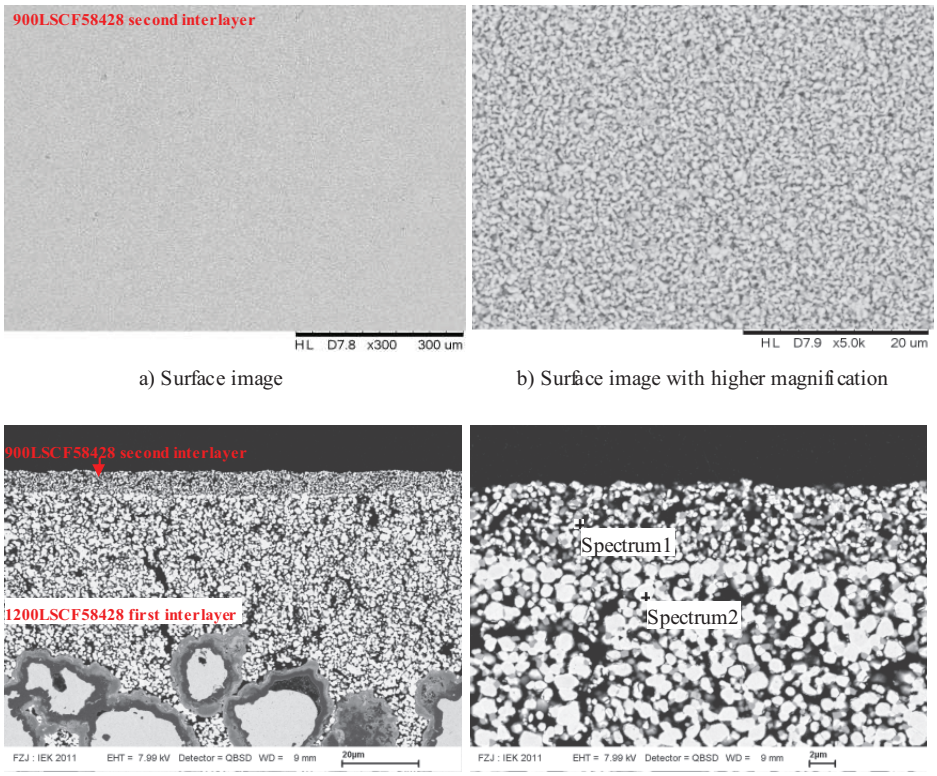

a) Surface image

b) Surface image with higher magnification

c) Cross section image

d) Cross section image with higher magnification

Figure 4.38: SEM images of the 900LSCF58428 second interlayer coated with paste 900LSCF60%_T after co-firing at 1100°C for 5h in air

For comparison, paste 1200LSCF70%_BF was screen printed on the 1200LSCF58428 first interlayer with a WLT 43µm sieve as the second interlayer then co-fired again at 1100°C for 5h in air. Figure 4.39 shows SEM images of the sample with both interlayers on the substrate. Figure 4.39a and b give surface images with different magnifications. Figure 4.39c and d give cross section images. On surface images and cross section images cracks have not been found in the second interlayer, but it also comprised large amounts of pores. Figure 4.39d shows the higher magnification of the 1200LSCF58428 second interlayer. Though the free-stand layer made from paste 900LSCF60%_TF showed a

denser structure than the layer made from paste 1200LSCF70%_BF (Figure 4.35), the substrate strongly hindered the sintering behavior of the screen printed layer during the co-firing. After the co-firing with the substrate together, both layers showed almost the same performance.

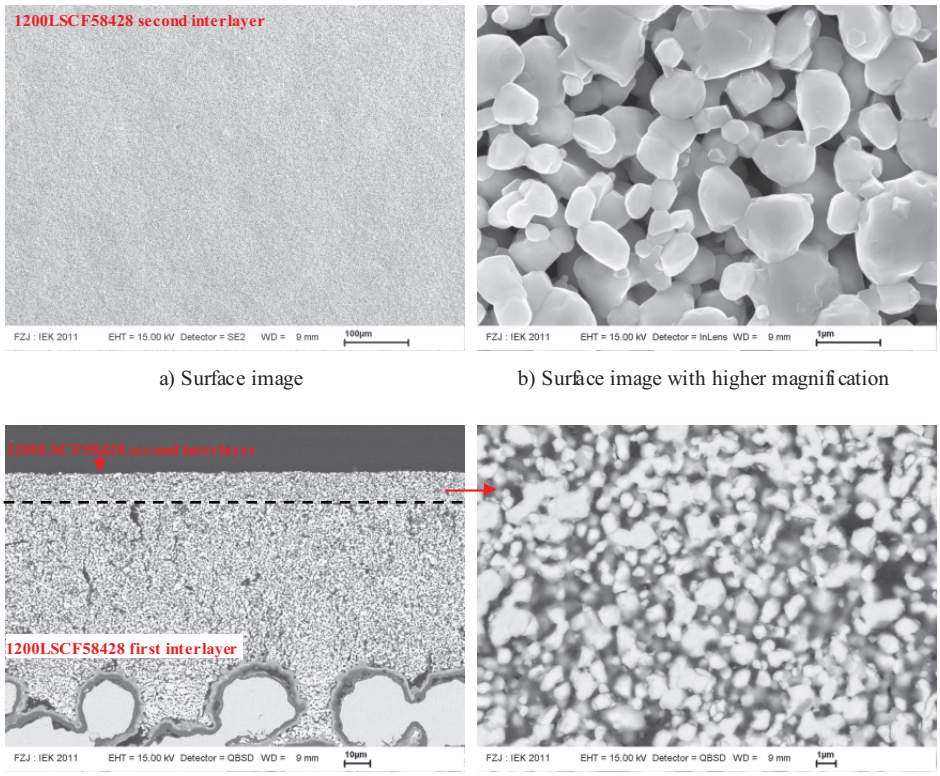

a) Surface image

b) Surface image with higher magnification

c) Cross section image

d) Cross section image with higher magnification

Figure 4.39: SEM images of the 1200LSCF58428 second interlayer coated with paste 1200LSCF70%_BF after co-firing at 1100°C for 5h in air

The LSCF58428 second interlayer showed a crack-free but porous structure. The top layer deposition technique (PVD) is very sensitive to the surface pore size. Surface pore size distributions of the 900LSCF58428 and 1200LSCF58428 second interlayer were

characterized. The confocal laser microscopy (VK-9710K, KEYENCE, Japan) was carried out to scan the area (Figure 4.40) and the software SPIP 5.1.3. was used to measure the distribution of pore size shown in Figure 4.41. Pores always have irregular shapes and the skeleton length describes the possible longest length in pores. 900LSCF58428 and 1200LSCF58428 layer showed the similar surface pore size distribution. Most of surface pores in both layers were around 1-2µm.

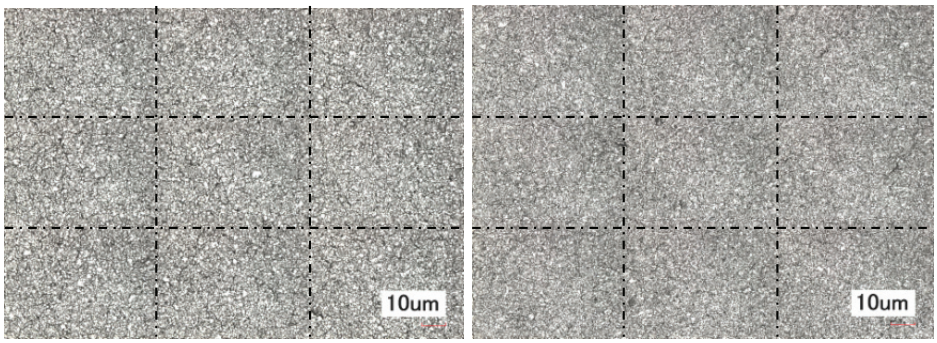

a) 900LSCF58428 second interlayer b) 1200LSCF58428 second interlayer

Figure 4.40: Surface scanning for the pore size distribution measurements

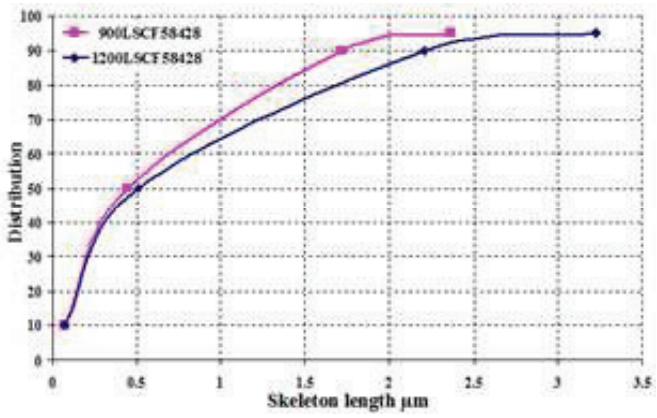

Figure 4.41: Surface pore size distributions of the 900LSCF58428 and 1200LSCF58428 second interlayer

According to above results, though the first interlayer comprised still some cracks, it significantly improved the surface quality and the surface pore size has been reduced from 30-50µm in the substrate to few µm in the first interlayer. The LSCF58428 second interlayers (900LSCF58428 second interlayer or 1200LSCF58428 second interlayer) showed a crack-free but still porous structure. Surface pore sizes in the second interlayer were around 1-2µm. Cracks and the porous structure in the first interlayer helped the second interlayer to release the internal stress due to the shrinkage mismatch during the co-firing.

4.5 Top layer deposition

As described in chapter 4.4 two interlayers were coated on the porous NiCoCrAlY1225 substrate by screen printing. The first interlayer was screen printed by paste 1200LSCF70%_BF made from the low specific surface area powder, which comprised segmentation cracks. Paste 1200LSCF70%_BF or paste 900LSCF60%_TF were screen printed on the first interlayer as the second interlayer. Both of second interlayers showed a crack-free structure, but they were still porous. In order to obtain the desired oxygen separation function another gas-tight top layer is required. The top layer was deposited by physical vapor deposition (PVD) technology, i.e. magnetron sputtering. The schematic picture of the multi-layer membrane structure is shown in Figure 4.42.

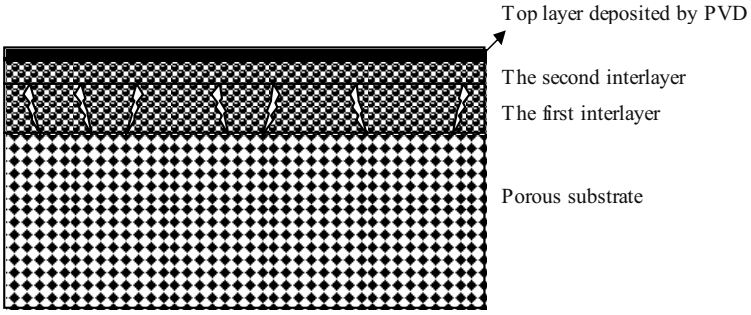

Figure 4.42: Schematic picture of the multi-layer membrane structure

$La_{0.58}Sr_{0.4}Co_{0.2}Fe_{0.8}O_{3-\delta}$ (LSCF58428) powder was used as the target for the deposition of the top layer. The PVD layer was coated on both types of second interlayer, i.e. 900LSCF58428 and 1200LSCF58428. Figure 4.43 shows SEM images and EDS analyses of LSCF58428 PVD layer on the 900LSCF58428 second interlayer. Figure 4.43a and b show the surface and cross section images. The LSCF58428 PVD layer with a thickness of 3.8µm had a columnar structure. Although it showed a relatively dense structure, some tiny pores could be observed on the surface and cross section images. Leakage tests were carried out by air and it had a leakage rate in the range of 2.2×10^{-1}mbar·l/s·cm^2 to $4.5\times10^{-}$

^{1}mbar·l/s·cm^{2}. Figure 4.43c and d give the EDS analysis results. Spectrum 1 and spectrum 2 consisted of only La, Sr, Co, Fe and O and no second phase could be detected by the back-scattered SEM investigation revealing that the perovskite phase was stable.

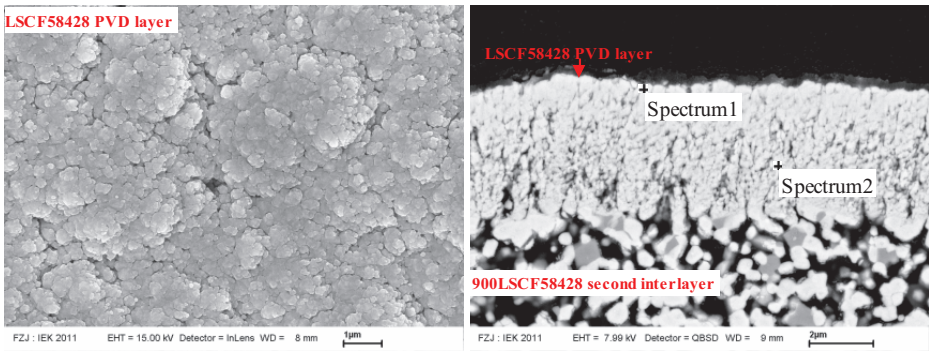

a) Surface image b) Cross section image

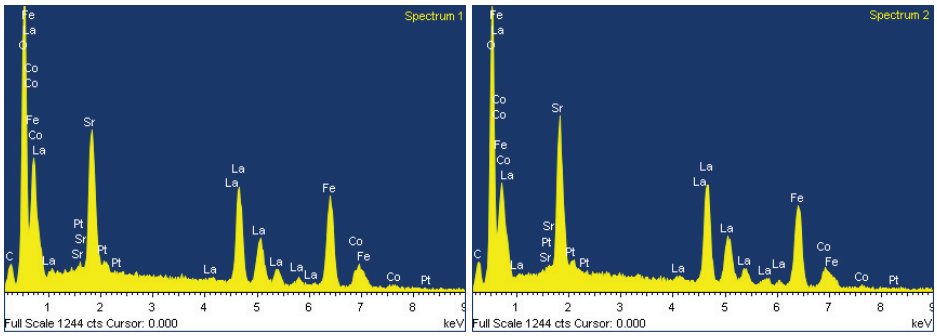

c) Spectrum1 d) Spectrum2

Figure 4.43: SEM images and EDS analyses of LSCF58428 PVD layer on the 900LSCF58428 second interlayer

Figure 4.44 shows SEM images of LSCF58428 PVD layer on the 1200LSCF58428 second interlayer. Figure 4.44a and b show the surface and cross section images. They showed almost the same performance as the layer coated on the 900LSCF58428 second interlayer and it had also the comparable leakage rate in the range of 2.0×10^{-1}mbar·l/s·cm^{2} to 3.2×10^{-1}mbar·l/s·cm^{2}.

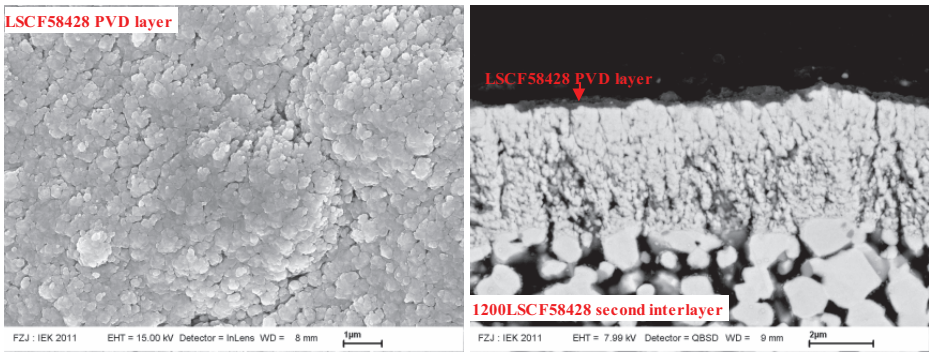

a) Surface image b) Cross section image

Figure 4.44: SEM images of LSCF58428 PVD layer on the 1200LSCF58428 second interlayer

Figure 4.45 shows the SEM image of a fabricated asymmetric membrane structure. The porous NiCoCrAlY with approx. 1mm thickness was applied as the substrate and the 1200LSCF58428 first interlayer was screen printed on the substrate, then co-fired at 1100°C for 5h in air with a thickness of approx. 50µm. The 900LSCF58428 second interlayer was screen printed on the fired first interlayer and co-fired at 1100°C again. This layer was approx.10µm thick. Finally the LSCF58428 top layer was deposited by PVD on the second interlayer with a thickness of 3.8µm. The sample with 1200LSCF58428 second interlayer had the similar structure. Though the leakage rate of such a structure is still pretty high ($2\text{-}4\times10^{-1}$mbar·l/s·cm^2), it has already been much improved compared to the sample only with the second interlayer which are unmeasurable (extremely high leakage) during leakage tests. In order to improve gas-tightness PVD technology for the perovskite deposition should be further developed in the future, e.g. by using reactive magnetron sputtering and/or applying a bias assistance. Similar interlayer structures are successful coated using PVD techniques in solid oxide fuel cell development. In addition, further interlayer development using different techniques, e.g. Sol-Gel, or development of a nanoparticle-based screen printing paste could be preceded.

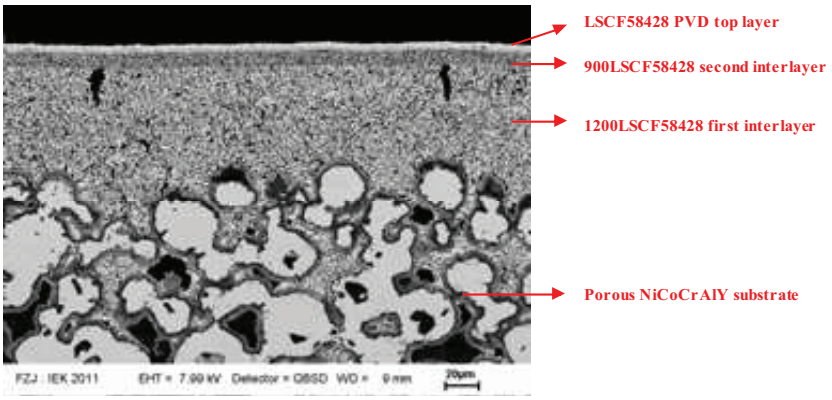

Figure 4.45: SEM image of a fabricated asymmetric membrane structure

5. Summary and Conclusions

Asymmetric membrane structure with a thin film oxygen transport membrane and porous metallic substrate has an attractive potential in the application of O_2/N_2 gas separation membrane for the future membrane-based fossil fuel power plant. In this study a multi-layer asymmetric membrane structure with a perovskite top layer, two porous interlayers and a porous Ni-based alloy substrate has been developed.

Four perovskite materials were studied as candidate membrane materials, i.e. $La_{0.58}Sr_{0.4}Co_{0.2}Fe_{0.8}O_{3-\delta}$ (LSCF58428), $La_{0.58}Sr_{0.4}Co_{0.8}Fe_{0.2}O_{3-\delta}$ (LSCF58482), $La_{02}Sr_{0.8}Co_{0.8}Fe_{0.2}O_{3-\delta}$ (LSCF2882) and $Ba_{0.5}Sr_{0.5}Co_{0.8}Fe_{0.2}O_{3-\delta}$ (BSCF5582). Different material properties of these perovskite materials were measured and compared. LSCF58428 was considered as the standard material for the comparison. When Co content was elevated as LSCF58482, it showed the similar permeation flux as LSCF58428, but it had a higher densification temperature and a higher TEC. If Sr content and Co content were elevated as LSCF2882, a higher permeation flux was obtained as well as a higher TEC. Though the standard composition LSCF58428 had a lower permeation flux than LSCF2882, LSCF2882 had a much higher TEC than candidate substrate materials Ni-based alloys ($16\text{-}19\times10^{-6}\cdot K^{-1}$), which is unacceptable for a multi-layer structure. BSCF5582 had a higher permeation flux than all the three LSCF as can be expected from literatures and it had a slightly higher TEC than candidate substrate materials. But the chemical stability at high temperature under CO_2-containing atmosphere should be considered.

Four different Ni-based alloys were studied as substrate candidate materials in the asymmetric membrane structure. The chromia-scale alloys (Hastelloy X and Inconel 600) caused Cr poisoning of the membrane layer material LSCF58428 during high-temperature co-firing in air. Therefore, chromia-scale materials were deemed unsuitable for use as a substrate material for perovskite membrane. Haynes 214 with a low Al content (3.4 wt%) showed a similar performance due to the depletion of Al when it was co-fired with a LSCF58428 membrane layer at a high temperature in air. NiCoCrAlY with a high Al content (12.7 wt%) was found to be the most promising substrate material. It showed good

chemical compatibility with perovskite materials at high temperatures. LSCF58428 and BSCF5582 membrane layer kept their perovskite structures after co-firing with NiCoCrAlY, and the alumina surface layer on NiCoCrAlY performed well against elemental diffusion (Ni and Cr) from NiCoCrAlY to the membrane materials. However, limited reaction zones occurred between alkaline earth in the perovskites and the alumina-based surface layer on NiCoCrAlY, which has to be considered. Porous interlayers were introduced between the substrate and the membrane in order to bridge the highly porous substrate and the thin dense membrane layer. Thus, the reaction zone was hold in distance from the membrane surface. The reaction zone was found to be stable in mid-term annealing at 800°C in air. Hence, it is not expected that this reaction will prevent the application of this alloy as the substrate in an asymmetric membrane structure. Different co-firing atmospheres, i.e. air, vacuum, and H_2(4%)/Ar were investigated. Air was found to be the only suitable atmosphere, because the perovskite structures, and thus the oxygen permeability, were lost during co-firing in the other atmospheres.

Porous NiCoCrAlY substrates were manufactured by PLANSEE (PLANSEE SE, Reutte, Austria), which were sintered at different temperatures under pure H_2 for 3h, i.e. 1150°C, 1200°C, 1225°C and 1250°C. Porous NiCoCrAlY substrate sintered at 1225°C showed sufficient gas flow permeability based on the reasonable open porosity, which resulted in appropriate corrosion resistance and mechanical properties. It was chosen as the porous substrate in the asymmetric membrane structure. Based on the oxidation behavior investigations of dense NiCoCrAlY compact, the temperature for co-firing of the porous substrate and the interlayer was limited to 1100°C.

The interlayers were developed on the porous substrate. The interlayers were coated by screen printing and the screen printing paste was optimized by various solvent, binder and dispersant combinations and various ceramic powder contents. One paste made from the low specific surface area LSCF58428 powder and one paste made from the high specific surface area LSCF58428 were chosen for coating interlayers after evaluation based on measurement of rheological behavior, printing properties and green density. Two interlayers were coated on the porous substrate. The 1200LSCF58428 first interlayer was screen printed on the substrate, then co-fired at 1100°C for 5h in air with a thickness of

approx. 50µm. The first interlayer significantly improved the surface quality and the surface pore size has been reduced from 30-50µm on the substrate to several micrometers, though it comprised still some cracks. Two different LSCF58428 second interlayers were screen printed on the fired first interlayer and co-fired at 1100°C again. Both second interlayers were 10µm thick and showed crack-free and porous structure. Most of surface pores were around 1-2µm.

A top membrane layer was deposited by physical vapor deposition technology, i.e. magnetron sputtering, with the $La_{0.58}Sr_{0.4}Co_{0.2}Fe_{0.8}O_{3-\delta}$ (LSCF58428) target on the crack-free second interlayer. Both PVD layers had a thickness of 3.8µm and a columnar structure. From EDS analyses, no element beside La, Sr, Co and Fe has been detected in the PVD layer. Thus, a multi-layer asymmetric membrane structure with one PVD LSCF58428 top layer and two screen printed LSCF58428 interlayers on the porous NiCoCrAlY substrate was developed. The membrane structure had the leakage rate in the range of 2.0×10^{-1}mbar·l/s·cm^2 to 4.5×10^{-1}mbar·l/s·cm^2, which is considerable but still too high for the application. In order to improve gas-tightness PVD technology for the perovskite deposition should be further developed in the future, e.g. by using reactive magnetron sputtering and/or applying a bias assistance. Similar interlayer structures are successful coated using PVD techniques in solid oxide fuel cell development. In addition, further interlayer development using different techniques, e.g. Sol-Gel, or development of a nanoparticle-based screen printing paste could be preceded. It can be summarized that a stable metal-perovskite-composite could successfully be developed. This acts as a basis for further development of a novel gas-tight metal supported oxygen transport membrane structure.

Reference

[ARN07] M. Arnold, H. Wang and A. Feldhoff, Influence of CO_2 on the oxygen permeation performance and the microstructure of perovskite-type $Ba_{0.5}Sr_{0.5}Co_{0.8}Fe_{0.2}O_{3-\delta}$ membranes, Journal of Membrane Science 293 (2007) 44–52

[BAU11] S. Baumann, J. M. Serra, M. P. Lobera, S. Escolástico, F. Schulze-Küppers and W. A. Meulenberg, Ultrahigh Oxygen Permeation Flux through Supported $Ba_{0.5}Sr_{0.5}Co_{0.8}Fe_{0.2}O_{3-\delta}$ Membranes, Journal of Membrane Science, Volume 377, Issue 1-2, 15 July 2011, Pages 198-205

[BEC08] T. Beck, R. Herzog, O. Trunova, M. Offermann, R.W. Steinbrech and L. Singheiser, Damage mechanisms and lifetime behaviour of plasma-sprayed thermal barrier coating systems for gas turbines – Part II: Modeling, Surface & Coatings Technology 202 (2008) 5901-5908

[BER06] K.A. Berchtold, J.S. Young, K.W. Dudeck, J. Acquaviva, F. Onorato and S.D. Hopkins, Novel Polymeric-Metallic Composite Membranes for CO_2 Separations at Elevated Temperatures, Fifth Annual Conference on Carbon Capture & Sequestration, Alexandria, Virginia (2006)

[BET09] M. Betz, Doctoral dissertation- Herstellung und Charakterisierung von sauerstoffionenleitenden Dünnschichtmembranstrukturen, Forschungs-zentrum Jülich GmbH, (2009)

[BET10] M. Betz, S. Baumann, F. Schulze-Küppers, W.A. Meulenberg, D. Stöver, Supported oxygen trans-port membranes for oxyfuel power plants. Advances in Science and Technology Vol 72 (2010) 93-98.

[BHA00] A.S. Bhalla, R. Guo and R. Roy, The perovskite structure – a review of its role in ceramic science and technology, Mater. Res. Innovat. 4 (2000) 3

[BHA03] H.K.D.H. Bhadeshia, Nickel Based Superalloys (2003). http://www.msm.cam.

ac.uk/phase-trans/2003/Superalloys /superalloys. html.

[BOU94] H.J.M. Bouwmeester, H. Kruidhof and A.J. Burggraaf, Importance of the surface exchange kinetics as rate limiting step in oxygen permeation through mixed-conducting oxides, Solid State Ionics 72 (1994) 185-194

[BOU96] H.J.M. Bouwmeester and A.J. Burggraaf, Dense ceramic membranes for oxygen separation, in: A.J. Burggraaf, L. Cot (Eds.), Fundamentals of Inorganic Membrane Science and Technology, Elsevier Science B.V., Amsterdam, (1996) p. 483

[BOW00] R. Bowman, Superalloys: A Primer and History (2000). http://www.tms.org/meetings/specialty/superalloys2000/superalloyshistory.html

[BÜC07] O. Büchler, J.M. Serra, W.A. Meulenberg , D. Sebold and H.P. Buchkremer, Preparation and properties of thin $La_{1-x}Sr_xCo_{1-y}Fe_yO_{3-\delta}$ perovskitic membranes supported on tailored ceramic substrates, Solid State Ionics 178 (2007) 91–99

[CAO94] G.Z. Cao, Electrical conductivity and oxygen semipermeability of terbia and yttria stabilized zirconia, J. Appl. Electrochem 24 (1994), p. 1222

[CAR92] S. Carter, A. Selcuk, J. Chater, R.J. Kajda, J.A. Kilner and B.C.H. Steele, Oxygen transport in selected nonstoichiometric perovskite-structure oxides, Solid State Ionics (1992) 53–56, 597–605

[CHA08] X. Chang, C. Zhang, X. Dong, C. Yang, W. Jin, N. Xu N. Experimental and modeling study of oxygen permeation modes for asymmetric mixed-conducting membranes. J. Membrane Sci. 322 (2008) 429-435

[CHE03] J.C.C. Chen, H. Chen, R. Prasad and G. Whichard, Plasma sprayed oxygen transport membrane coatings, US Patent 6,638,575 (2003)

[COO08] L. Cooper, S. Benhaddad, A. Wood and D.G. Ivey, The effect of surface treatment on the oxidation of ferritic stainless steels used for solid oxide fuel cell interconnects, Journal of Power Sources Volume 184, Issue 1 (2008) Pages 220-228

[CZY10] M. Czyperek , P. Zapp, H.J.M. Bouwmeester, M. Modigell, K. Ebert, I. Voigt, W.A. Meulenberg, L. Singheiser and D. Stöver, Gas separation membranes for zero-emission fossil power plants: MEM-BRAIN, Journal of Membrane Science 359 (2010) 149–159

[DAL09] B.T. Dalslet, M. Søgaard, H.J.M. Bouwmeester and P.V. Hendriksen, Defect chemistry and oxygen transport of $(La_{0.6}Sr_{0.4-x}M_x)_{0.99}Co_{0.2}Fe_{0.8}O_{3-\delta}$, M=Ca (x=0.05, 0.1), Ba (x=0.1, 0.2), Sr Part I: Defect chemistry, Solid State Ionics 180 (2009) 1173–1182

[DIL05] D.J. Dillon, R.S. Panesar, R.A. Wall, R.J. Allam, V. White, J. Gibbins and M.R. Haines, Oxy-combustion processes for CO_2 capture from advanced supercritical PF and NGCC power plant, Greenhouse Gas Control Technol. 7 (2005) 211–220

[DOL02] A. Dolatabadi, J. Mostaghimi and V. Pershin, Effect of a cylindrical shroud on particle conditions in high velocity oxy-fuel spray process, Science and Technology of Advanced Materials 3 (2002) 245–255

[ENG10] S. Engels, F. Beggel, M. Modigell and H. Stadler, Simulation of a membrane unit for oxyfuel power plants under consideration of realistic BSCF membrane properties, Journal of Membrane Science 359 (2010) 93–101

[EZU03] E. O. Ezugwu, J. Bonneya and Y. Yamane, An overview of the machinability of aeroengine alloys, Journal of Materials Processing Technology 134 (2003) 233-253

[FIG08] J.D. Figueroa, T. Fout, S. Plasynski, H. McIlvried and R.D. Srivastava, Advances in CO_2 capture technology-The U.S. Department of Energy's Carbon Sequestration Program, Int. J. Greenhouse Gas Controll 2 (2008) 9–20

[FTI93] C. Ftikos, S. Carter and B.C.H. Steele, Mixed electronic/ionic conductivity of the solid solution $La_{(1-x)}Sr_xCo_{(1-y)}Ni_yO_{3-\delta}$ (x: 0.4, 0.5, 0.6 and y: 0.2, 0.4, 0.6), J. Eur. Ceram. Soc., (1993) 12, 79–86

[FUK09] K.Fukuda and K.Fukushima, Crystal structure of hexagonal of $SrAl_2O_4$ at 1073K, Journal of Solid State Chemistry 178 (2009) 2709-2714

[GE07] L. Ge, W. Zhou, R. Ran, S. Liu, Z. Shao, W. Jin and N. Xu, Properties and performance of A-site deficient $(Ba_{0.5}Sr_{0.5})_{1-x}Co_{0.8}Fe_{0.2}O_{3-\delta}$ for oxygen permeating membrane, Journal of Membrane Science 306 (2007) 318–328

[GEL97] P.J. Gellings and H.J.M. Bouwmeester, The CRC handbook of solid state electrochemistry, Boca Raton: CRC Press (1997)

[GES10] T. V. Gestel, , D. Sebold, F. Hauler, W.A. Meulenberg and H.P. Buchkremer, Potentialities of microporous membranes for H_2/CO_2 separation in future fossil fuel power plants: Evaluation of SiO_2, ZrO_2, Y_2O_3–ZrO_2 and TiO_2–ZrO_2 sol–gel membranes, Journal of Membrane Science 359 (2010) 64–79

[GOL26] V. M. Goldschmidt, Geochemische Verteilungsgesetze der Elemente – Die Gesetze der Krystallochemie. Akad. Oslo (1926)

[HAA01] M. Haar, Mixed-conducting perovskite membranes for oxygen separation towards the development of a supported thin-film membrane, Enschede (2001)

[HAS10] S. Hashimoto, Y. Fukuda, M. Kuhn, K. Sato, K. Yashiro and J. Mizusaki, Oxygen nonstoichiometry and thermo-chemical stability of $La_{0.6}Sr_{0.4}Co_{1-y}Fe_yO_{3-\delta}$ (y = 0.2, 0.4, 0.6, 0.8) , Solid State Ionics 181 (2010) 1713–1719

[HAU10] F. Hauler, Doctoral dissertation- Herstellung und Charakterisierung von Keramik- und metallgestützten Membranschichten für die CO_2-Abtrennung in fossilen Kraftwerken, Forschungszentrum Jülich GmbH (2010)

[HEN00] P.V. Hendriksen, P.H. Larsen, M. Mogensen, F.W. Poulsen and K. Wiik, Prospects and problems of dense oxygen permeable membranes, Catalysis Today 56 (2000) 283–295

[HOB97] A. Hobby, Screen printing for the industrial user, March (1997)

[HON10] W. K. Hong and G. M. Choi, Oxygen permeation of BSCF membrane with varying thickness and surface coating, Journal of Membrane Science 346 (2010) 353–360

[IEA04] IEA. Prospects for CO_2 capture and storage, Energy technology analysis, France: OECD/IEA; (2004)

[ISH88] T. Ishigaki, S. Yamauchi, K. Kishio, J. Mizusaki and K. Fueki, Diffusion of oxide ion vacancies in perovskite-type oxides, J. Solid State Chem., (1988) 73, 179–187

[ITO77] S. Ito, S. Banno, K. Suzuki, and M. Inagaki, Phase transitions in $SrAl_2O_4$, Zeits. Phys. Chem., 105 (1977)173-178

[JIN01] W. Jin, S. Li, P. Huang, N. Xu and J. Shi, Preparation of an asymmetric perovskite-type membrane and its oxygen permeability, Journal of Membrane Science 185 (2001) 237–243

[JOH07] C. Johns, M.S. Islam and J.R. Groza, Physical and chemical vapor deposition processes, In: J.R. Groza, J.F. Shackelford, E.J. Lavernia and M.T. Powers (Editors), Materials processing handbook, CRC Press (2007) p. 8-9

[JUD01] R.R. Judkins and B.L. Bischoff, Development of Microporous Inorganic Membranes for Separation and Purification of Hydrogen, http://www.ornl.gov /~webworks/ cppr/y2001/pres/120833.pdf

[KHA00] V.V. Kharton, A.V. Kovalevsky, A.P. Viskup, F.M. Figueiredo, J.R. Frade, A.A. Yaremchenko and E.N. Naumovich, Faradaic efficiency and oxygen permeability of $Sr_{0.97}Ti_{0.60}Fe_{0.40}O_{3-\delta}$ perovskite, Solid State Ionics 128 (2000) 117

[KIL00] J.A. Kilner, Fast oxygen transport in acceptor doped oxides, Solid State Ionics 129 (2000) 13–23

[KOS99] G.C. Kostogloudis and C. Ftikos, Properties of A-site-deficient $La_{0.6}Sr_{0.4}Co_{0.2}Fe_{0.8}O_{3-\delta}$-based perovskite oxides, Solid State Ionics 126 (1999) 143

[KRU04] P. Krukovsky, V. Kolarik, K. Tadlya, A. Rybnikov, I. Kryukov, N. Mojaiskaya and M. Juez-Lorenzo, Lifetime prediction for MCrAlY coatings by means of inverse problem solution (IPS), Surface and Coatings Technology 177 –178 (2004) 32–36

[LAN99] J.A. Lane, S.J. Benson, D. Waller and J.A. Kilner, Oxygen transport in $La_{0.58}Sr_{0.4}Co_{0.2}Fe_{0.8}O_{3-\delta}$, Solid State Ionics 121 (1999) 201–208

[LI99] S. Li, W. Jin, N. Xu and J. Shi, Synthesis and oxygen permeation properties of $La_{0.2}Sr_{0.8}Co_{0.2}Fe_{0.8}O_{3-\delta}$ membranes, Solid State Ionics 124 (1999) 161–170

[LIN94] Y.S. Lin, W. Wang and J. Han, Oxygen permeation through thin mixed-conducting solid oxide membranes, AIChE J. 40 (5) (1994), p. 786

[LIU03] Y. Liu and L. Hong, Fabrication and characterization of (Pd/Ag)–$La_{0.2}Sr_{0.8}CoO_{3-\delta}$ composite membrane on porous asymmetric substrates, Journal of Membrane Science 224 (2003) 137–150

[LIU06] Y. Liu, X. Tan, and K. Li, Mixed Conducting Ceramics for Catalytic Membrane Processing, Catalysis Reviews, 48:145–198, (2006)

[MAR09] J. Martynczuk, F. Liang, M. Arnold, V. Sepelak and A. Feldhoff, Aluminum-Doped Perovskites as High-Performance Oxygen Permeation Materials, Chem. Mater. 21 (2009) 1586–1594

[MCI06] S.McIntosh, J. F. Vente, W.G. Haije, D.H.A. Blank and H.J.M. Bouwmeester, Phase stability and oxygen non-stoichiometry of $SrCo_{0.8}Fe_{0.2}O_{3-\delta}$ measured by in situ neutron diffraction , Solid State Ionics 177 (2006) 833–842

[MID04] H. Middletona, S. Diethelmb, R. Ihringerb, D. Larrain, J. Sfeir and J. V. Herleb, Co-casting and co-sintering of porous MgO support plates with thin dense perovskite layers of $LaSrFeCoO_3$, Journal of the European Ceramic Society 24 (2004) 1083–1086

[OBR09] K.C.O Brien, G. Krishnan and K.A. Berchtold, Towards a pilot-scale membrane system for pre-combustion CO_2 separation, Energy Procedia 1 (2009) 287-294

[PEC67] M.P. Pechini, Method of preparing lead and alkaline earth titanates and niobates and coating method using to form a capacitor. US-Patent No. 3,330,697 July, 11th (1967)

[PEI95] S. Pei, M.S. Kleefisch, T.P. Kobylinski, J. Faber, C.A. Udovich, V. Zhangmccoy, B. Dabrowski, U. Balachandran, R.L. Mieville and R.B. Poeppel, Failure mechanisms of ceramic membrane reactors in partial oxidation of methane to synthesis gas, Catalysis Letters 30 (1995) 201–212

[PET00] A. Petric, P. Huang, F. Tietz, Evaluation of La–Sr–Co–Fe–O perovskites for solid oxide fuel cells and gas separation membranes, Solid State Ionics 135 (2000) 719–725

[PFA09] I. Pfaff and A. Kather, Comparative thermodynamic analysis and integration issues of CCS steam power plants based on oxy-combustion with cryogenic or membrane based air separation, Energy Procedia 1 (2009) 495–502

[SCH98] G. Schramm, A Practical approach to rheology and rheometry, (1998) $_{0.2}$

[SCH09a] D. Schlehuber, E. Wessel, L. Singheiser and T. Markus, Determination of Diffusion Coefficients of Oxygen Vacancies in $La_{0.58}Sr_{0.4}Co_{0.2}Fe_{0.8}O_{3-\delta}$ Perovskite Type Oxides, Defect and Diffusion Forum (2009) 551-554

[SCH09b] C. Schulz, Diploma thesis of Elektrolytpasten für oxidkeramische Brennstoffzellen (SOFC) mit nanoskaligem Zirkoniumdioxid, (2009)

[SCH10] D. Schlehuber, E. Wessel, L. Singheiser and T. Markus, Long-term operation of a $La_{0.58}Sr_{0.4}Co_{0.2}Fe_{0.8}O_{3-\delta}$ –membrane for oxygen separation, Journal of Membrane Science 351 (2010) 16–20

[SCO02] S.P. Scott, D. Mantzavinos, A. Hartley, M. Sahibzada and I.S. Metcalfe, Reactivity of LSCF perovskites, Solid State Ionics 152 (2002) 777–781

[SEO08] D. Seo, K. Ogawa, Y. Suzuki, K. Ichimura, T. Shoji and S. Murata, Comparative study on oxidation behaviour of selected MCrAlY coatings by elemental concentration profile analysis, Applied Surface Science 255 (2008) 2581–2590

[SEB07] V. Sebastián, I. Kumakiri, R. Bredesen and M. Menéndez, Zeolite membrane for CO_2 removal: Operating at high pressure, Journal of Membrane Science 292 (2007) 92–97

[SHA00] Z.P. Shao, W.S. Yang, Y. Cong, H. Dong, J.H. Tong and G.X. Xiong, Investigation on the permeation behaviour and stability of a $Ba_{0.5}Sr_{0.5}Co_{0.8}Fe_{0.2}O_{3-\delta}$ oxygen membrane, J. Membr. Sci. 172 (2000) 177

[SHA01] Z. Shao, G. Xiong , H. Dong, W. Yang and L. Lin, Synthesis, oxygen permeation study and membrane performance of a $Ba_{0.5}Sr_{0.5}Co_{0.8}Fe_{0.2}O_{3-\delta}$ oxygen permeable dense ceramic reactor for partial oxidation of methane to syngas, Separation and Purification Technology 25 (2001) 97–116

[SIN05] J. Singh and D. E. Wolfe, Review Nano- and macro-structured component fabrication by electron beam-physical vapor deposition (EB-PVD), Journal of Materials Science 40 (2005) 1– 26

[SIR06] J. Sirman, The evolution of Materials and Architecture for Oxygen Transport Membranes. In: F. Sammells, M.V. Mundschau (Editors), Nonporous inorganic membranes for chemical processing, WILEY-VCH (2006) p. 168-192

[STE95] J.W. Stevenson, P.E. Hallman, T.R. Armstrong and L.A. Chick, Sintering behaviour of doped lanthanum and yttrium manganite, J. Am. Ceram. Soc. 78 (1995) 507

[STE96] J.W. Stevenson, I. Armstrong, R. D. Carneim, L.Pederson, and W. J. Weber, Electrochemical Properties of Mixed Conducting Perovskites $La_{1-x}M_xCo_{1-y}Fe_yO_{3-\delta}$ (M = Sr, Ba, Ca), J. Electrochem. Soc., Vol. 143, No.9, September (1996)

[STR09] L.Strömberg, G. Lindgren, J. Jacoby, Update on Vattenfall's 30 MWth Oxyfuel Pilot Plant in Schwarze Pumpe, Energy Procedia 1 (2009) 581-589

[SUB08] M. Subanovic, D. Sebold, R. Vassen, E. Wessel, D. Naumenko, L. Singheiser and W. J. Quadakkers, Effect of manufacturing related parameters on oxidation properties of MCrAlY-bondcoats, Materials and Corrosion No. 6 (2008) 59

[SUN08] J. Sunarso, S. Baumann, J.M. Serra,W.A. Meulenberg, S. Liu, Y.S. Lin and J.C. Diniz da Costa, Mixed ionic–electronic conducting (MIEC) ceramic-based membranes for oxygen separation, Journal of Membrane Science 320 (2008) 13–41

[SUR09] J. Surendran, Diploma thesis of Manufacturing of Nanostructured Cathodes for Oxygen Transport Membrane (2009)

[TAS98] C. Tsai, A. G. Dixon, Y. H. Ma, W.R. Moser and M.R. Pascucci, Dense Perovskite, $La_{1-x}A^*_xFe_{1-y}Co_yO_{3-\delta}$ (A* = Ba, Sr, Ca), Membrane Synthesis, Applications, and Characterization, J. Am. Ceram. Soc., 81 [6] (1998)1437–44

[TER85] Y. Teraoka, H.M. Zhang, S. Furukawa and N. Yamazoe, Oxygen permeation through perovskite-type oxides, Chem. Lett.(1985)1743

[TER88a] Y. Teraoka, H. M. Zhang, K. Okamoto, and N. Yamazoe, Mixed Ionic-Electronic Conductivity of $La_{1-x}Sr_xCo_{1-y}Fe_yO_{3-\delta}$ Perovskite-Type Oxides, Mater. Res. Bull., 23, (1988) 51–58

[TER88b] Y. Teraoka, T. Nobunaga and N. Yamazoe, Effect of cation substitution on the oxygen semipermeability of perovskite oxide, Chem. Lett (1988) 503

[TER02] Y. Teraoka, Y. Honbe, J. Ishii, H. Furukawa and I. Moriguchi, Catalytic effects in oxygen permeation through mixed-conductive LSCF perovskite membranes, Solid State Ionics 152– 153 (2002) 681– 687

[THI09] R. Thiruvenkatachari, S. Su, H. An and X. X. Yu, Post combustion CO_2 capture by carbon fibre monolithic adsorbents, Progress in Energy and Combustion Science 35 (2009) 438–455

[THO06] A. Thomas, M. El-Wahabi, J.M. Cabrera and J.M. Prado, High temperature deformation of Inconel 718, Journal of Materials Processing Technology 177 (2006) 469–472

[THU04] A.Thursfield and I.S. Metcalfe, The use of dense mixed ionic and electronic conducting membranes for chemical production, Journal of Material Chemistry, 14 (2004) 2475-2485

[ULL00] H. Ullmann , N. Trofimenko, F. Tietz, D. Stöver and A. Ahmad-Khanlou, Correlation between thermal expansion and oxide ion transport in mixed conducting perovskite-type oxides for SOFC cathodes, Solid State Ionics 138 (2000) 79–90

[VEN06] J.F. Vente, W.G. Haije and Z. S. Rak, Performance of functional perovskite membranes for oxygen production, Journal of Membrane Science 276 (2006) 178–184

[WAG75] C. Wagner, Equations for transport in solid oxides and sulfides of transition metals, Progress in solid state chemistry 10 (1975) Nr. 1, 3-16

[WAN11] B. Wang, B. Zydorczak, D. Poulidi, I.S. Metcalfe and K. Li, A further investigation of the kinetic demixing/decomposition of $La_{0.6}Sr_{0.4}Co_{0.2}Fe_{0.8}O_{3-\delta}$ oxygen separation membranes, Journal of Membrane Science 369 (2011) 526–535

[WAT08] K. Watanabe, M. Yuasa, T. Kida, K. Shimanoe, Y. Teraoka, N. Yamazoe. Preparation of oxygen evolution layer/$La_{0.6}Ca_{0.4}CoO_3$ dense membrane/porous support asymmetric structure for high-performance oxygen permeation. Solid State Ionics 179 (2008) 1377–1381.

[WEI11] C. Weiler, Diploma thesis of Herstellung von Elektrodenstrukturen für Hochtemperatur-Brennstoffzellen mittels physikalischer Gasphasen-abscheidung, (2011)

[XU98] S.J. Xu and W.J. Thomson, Stability of $La_{0.6}Sr_{0.4}Co_{0.2}Fe_{0.8}O_{3-\delta}$ perovskite membranes in reducing and nonreducing environments, Industrial & Engineering Chemistry Research 37 (1998) 1290–1299

[YAN06] Z. Yang, G.G. Xia and J. W. Stevenson, Evaluation of Ni–Cr-base alloys for SOFC interconnect applications, Journal of Power Sources 160 (2006) 1104–1110

[YIN06] X. Yin, L. Hong and Z. Liu, Oxygen permeation through the LSCO-80/CeO_2 asymmetric tubular membrane reactor, Journal of Membrane Science 268 (2006) 2–12

[YIN07] Q. Yin and Y.S. Lin, Beneficial effect of order–disorder phase transition on oxygen sorption properties of perovskite-type oxides, Solid State Ionics 178 (2007) 83

[YOK06] H. Yokokawa, T. Horita, N. Sakai, K. Yamaji, M.E. Brito, Y.P. Xiong and H. Kishimoto, Thermodynamic considerations on Cr poisoning in SOFC cathodes, Solid State Ionics 177 (2006) 3193–3198

[ZEN51] C. Zener, Interaction between the d-shells in the transition metals. II. Ferromagnetic compounds of manganese with perovskite structure. In: Physical review 82 (1951), Nr. 3, P. 403-405

[ZHA08] L. Zhao, E. Riensche, R. Menzer, L. Blum and D. Stolten, A parametric study of CO_2/N_2 gas separation membrane processes for post-combustion capture, Journal of Membrane Science 325 (2008) 284–294

List of figures

List of tables

List of abbreviations

BCA	(2-(2-Butoxyethoxy)ethyl acetate, 99.2+%)
BSCF5582	$Ba_{0.5}Sr_{0.5}Co_{0.8}Fe_{0.2}O_{3-\delta}$
BSF	$Ba_{0.5}Sr_{0.4}FeO_{3-\delta}$
CCS	Carbon capture and storage
CGO	$Ce_{0.8}Gd_{0.2}O_{1.9}$
DC	Direct current
EDS	Energy-dispersive X-ray spectroscopy
ICP-OES	Inductively coupled plasma-optical emission spectrometer
LCM	Substrate fabricated with the mixture of LSCF58428 and CGO by CoatMix
LSCF	$La_{1-x}Sr_xCo_{1-y}Fe_yO_{3-\delta}$
LSCF2828	$La_{0.2}Sr_{0.8}Co_{0.2}Fe_{0.8}O_{3-\delta}$
LSCF2882	$La_{0.2}Sr_{0.8}Co_{0.8}Fe_{0.2}O_{3-\delta}$
LSCF58428	$La_{0.58}Sr_{0.4}Co_{0.2}Fe_{0.8}O_{3-\delta}$
LSCF58482	$La_{0.58}Sr_{0.4}Co_{0.8}Fe_{0.2}O_{3-\delta}$
LSCF6428	$La_{0.6}Sr_{0.4}Co_{0.2}Fe_{0.8}O_{3-\delta}$
LSCFM	$La_{0.2}Sr_{0.8}Cr_{0.2}Fe_{0.79}Mg_{0.01}O_{3-\delta}$
LSCH	Substrate fabricated with the mixture of LSCF58428 and CGO by Tape Casting
LSCO-80	(Pd/Ag)-$La_{0.2}Sr_{0.8}CoO_{3-\delta}$
MIEC	Mixed ionic and electronic conductivities
NiCoCrAlY1150	NiCoCrAlY substrate sintered at 1150°C
NiCoCrAlY1200	NiCoCrAlY substrate sintered at 1200°C
NiCoCrAlY1225	NiCoCrAlY substrate sintered at 1225°C
NiCoCrAlY1250	NiCoCrAlY substrate sintered at 1250°C
PVD	Physical vapor deposition
SCF82	$SrCo_{0.8}Fe_{0.2}O_{3-\delta}$
SEM	Scanning electron microscopy
SOFC	Solid oxide fuel cell

TEC	Thermal expansion coefficient
TGO	Thermally growth oxide
WLT	Wet layer thickness
XRD	X-ray diffraction
ZCH	Central Division of Analytical Chemistry (ZCH) Forschungszentrum Jülich
900LSCF58428	$La_{0.58}Sr_{0.4}Co_{0.2}Fe_{0.8}O_{3-\delta}$ powder calcined at 900°C
1200LSCF58428	$La_{0.58}Sr_{0.4}Co_{0.2}Fe_{0.8}O_{3-\delta}$ powder calcined at 1200°C

Acknowledgement

This Ph.D work has been done at Forschungszentrum Jülich in the institute of Energy and Climate Research (IEK-1: Materials Synthesis and Processing) with the funding support of Helmholtz Association of German Research Centers (Initiative and Networking Fund), under the Helmholtz Alliance MEM-BRAIN.

I would like to thank the head of the institute Prof. Dr. rer. nat. Detlev Stöver as my Doctor Father for the supervision of my work.

I thank Prof. Dr. Robert Vaßen from the institute of Energy and Climate Research (IEK-1: Materials Synthesis and Processing) as the co-referee of my doctoral dissertation.

I thank Prof. Dr. rer. nat. Rainer Telle from the Institut für Gesteinshüttenkunde at RWTH Aachen as the co-referee of my doctoral dissertation.

I give my thanks to Prof. Dr.-Ing. V. Scherer from the Department of Energy Plant Technology in Faculty of Mechanical Engineering at Ruhr-Universität Bochum as the chairman of examination commission.

I would like to give my earnest thanks to my supervisor Dr. Stefan Baumann. During the last 3 years he provided me masterly guidance with immense patience. I also thank him for his fruitful discussion, for his helps for the accomplishment of the dissertation and for his constant encouragement. I would like to thank my group leader Dr. Wilhelm Albert Meulenberg. He always provided kindly helps when I met different kinds of problems during my work. I thank other colleagues in the membrane group for their helps, cooperation and support, Falk, Hyo-Jeong, Jan, Janka, Mariya, Michael, Stefan and Wolfgang.

I would like to thank Werner Herzhof for his helps of screen printing and Dr. Robert Mücke for his helps of the layer analysis and fruitful discussion. I thank Dr. Doris Sebold for the SEM investigation, Mark Kappertz for the sample preparation, Marie-Theres Gerhards for the thermal analysis, Dr. Werner Fischer and Mirko Ziegner for the XRD investigation, Sigrid Schwartz-Lückge for BET and Hg intrusion investigation, Hiltrud Moitroux for the photograph and Nicole Adels and Andrea Hilgers for the particle size measurements. I thank Dr. Sven Uhlenbruck and Frank Vondahlen for the PVD

deposition. I thank Vicky Rostin, Stefan Weitz, Hannelore Rüther, Marlene Pionke and Marianne Meyer for the organization and administration. I would like to thank Dr. Buchkremer and Prof. Vaßsen for the advice and remarks during my quarterly reports.

I would like to thank my Chinese colleagues especially, Dr. Qianli Ma, Dr. Li Meng, Dr. Feng Han and Linnan Du for their supports of scientific discussion and private life.

I give my thanks to external colleagues, Matthias Rüttinger, Prof. Dr.-Ing. Willem J. Quadakkers and Central Division of Analytical Chemistry (ZCH) Forschungszentrum Jülich.

I take this occasion to thank my wife Yuting Huang and my parents who always stood beside me and for their support.

Curriculum Vitae

Personal Information

Name: Ye Xing
Gender: Male
Date of birth: 28.08.1983
Place of birth: Henan
Nationality: Chinese

Education

07.2008-06.2011	Ph.D. Candidate, Mechanical engineering, "Development of Mixed Ionic Electronic Conducting Thin Film Membranes on Metallic Supports", Institute of energy and climate research - IEK-1, Materials synthesis and processing, Forschungszentrum Jülich
10.2005-03.2008	Master Degree, Metallurgical Engineering, RWTH Aachen
09.2001-07.2005	Bachelor Degree, Material Science and engineering, University of Science and Technology Beijing, China

1. **Einsatz von multispektralen Satellitenbilddaten in der Wasserhaushalts- und Stoffstrommodellierung – dargestellt am Beispiel des Rureinzugsgebietes**
   von C. Montzka (2008), XX, 238 Seiten
   ISBN: 978-3-89336-508-1

2. **Ozone Production in the Atmosphere Simulation Chamber SAPHIR**
   by C. A. Richter (2008), XIV, 147 pages
   ISBN: 978-3-89336-513-5

3. **Entwicklung neuer Schutz- und Kontaktierungsschichten für Hochtemperatur-Brennstoffzellen**
   von T. Kiefer (2008), 138 Seiten
   ISBN: 978-3-89336-514-2

4. **Optimierung der Reflektivität keramischer Wärmedämmschichten aus Yttrium-teilstabilisiertem Zirkoniumdioxid für den Einsatz auf metallischen Komponenten in Gasturbinen**
   von A. Stuke (2008), X, 201 Seiten
   ISBN: 978-3-89336-515-9

5. **Lichtstreuende Oberflächen, Schichten und Schichtsysteme zur Verbesserung der Lichteinkopplung in Silizium-Dünnschichtsolarzellen**
   von M. Berginski (2008), XV, 171 Seiten
   ISBN: 978-3-89336-516-6

6. **Politikszenarien für den Klimaschutz IV – Szenarien bis 2030**
   hrsg.von P. Markewitz, F. Chr. Matthes (2008), 376 Seiten
   ISBN 978-3-89336-518-0

7. **Untersuchungen zum Verschmutzungsverhalten rheinischer Braunkohlen in Kohledampferzeugern**
   von A. Schlüter (2008), 164 Seiten
   ISBN 978-3-89336-524-1

8. **Inorganic Microporous Membranes for Gas Separation in Fossil Fuel Power Plants**
   by G. van der Donk (2008), VI, 120 pages
   ISBN: 978-3-89336-525-8

9. **Sinterung von Zirkoniumdioxid-Elektrolyten im Mehrlagenverbund der oxidkeramischen Brennstoffzelle (SOFC)**
   von R. Mücke (2008), VI, 165 Seiten
   ISBN: 978-3-89336-529-6

10. **Safety Considerations on Liquid Hydrogen**
    by K. Verfondern (2008), VIII, 167 pages
    ISBN: 978-3-89336-530-2

11. **Kerosinreformierung für Luftfahrtanwendungen**
von R. C. Samsun (2008), VII, 218 Seiten
ISBN: 978-3-89336-531-9

12. **Der 4. Deutsche Wasserstoff Congress 2008 – Tagungsband**
hrsg. von D. Stolten, B. Emonts, Th. Grube (2008), 269 Seiten
ISBN: 978-3-89336-533-3

13. **Organic matter in Late Devonian sediments as an indicator for environmental changes**
by M. Kloppisch (2008), XII, 188 pages
ISBN: 978-3-89336-534-0

14. **Entschwefelung von Mitteldestillaten für die Anwendung in mobilen Brennstoffzellen-Systemen**
von J. Latz (2008), XII, 215 Seiten
ISBN: 978-3-89336-535-7

15. **RED-IMPACT**
Impact of Partitioning, Transmutation and Waste Reduction Technologies on the Final Nuclear Waste Disposal
SYNTHESIS REPORT
ed. by W. von Lensa, R. Nabbi, M. Rossbach (2008), 178 pages
ISBN 978-3-89336-538-8

16. **Ferritic Steel Interconnectors and their Interactions with Ni Base Anodes in Solid Oxide Fuel Cells (SOFC)**
by J. H. Froitzheim (2008), 169 pages
ISBN: 978-3-89336-540-1

17. **Integrated Modelling of Nutrients in Selected River Basins of Turkey**
Results of a bilateral German-Turkish Research Project
project coord. M. Karpuzcu, F. Wendland (2008), XVI, 183 pages
ISBN: 978-3-89336-541-8

18. **Isotopengeochemische Studien zur klimatischen Ausprägung der Jüngeren Dryas in terrestrischen Archiven Eurasiens**
von J. Parplies (2008), XI, 155 Seiten, Anh.
ISBN: 978-3-89336-542-5

19. **Untersuchungen zur Klimavariabilität auf dem Tibetischen Plateau - Ein Beitrag auf der Basis stabiler Kohlenstoff- und Sauerstoffisotope in Jahrringen von Bäumen waldgrenznaher Standorte**
von J. Griessinger (2008), XIII, 172 Seiten
ISBN: 978-3-89336-544-9

20. **Neutron-Irradiation + Helium Hardening & Embrittlement Modeling of 9%Cr-Steels in an Engineering Perspective (HELENA)**
by R. Chaouadi (2008), VIII, 139 pages
ISBN: 978-3-89336-545-6

21. **in Bearbeitung**

22. **Verbundvorhaben APAWAGS (AOEV und Wassergenerierung) – Teilprojekt: Brennstoffreformierung – Schlussbericht**
von R. Peters, R. C. Samsun, J. Pasel, Z. Porš, D. Stolten (2008), VI, 106 Seiten
ISBN: 978-3-89336-547-0

23. **FREEVAL**
Evaluation of a Fire Radiative Power Product derived from Meteosat 8/9 and Identification of Operational User Needs
Final Report
project coord. M. Schultz, M. Wooster (2008), 139 pages
ISBN: 978-3-89336-549-4

24. **Untersuchungen zum Alkaliverhalten unter Oxycoal-Bedingungen**
von C. Weber (2008), VII, 143, XII Seiten
ISBN: 978-3-89336-551-7

25. **Grundlegende Untersuchungen zur Freisetzung von Spurstoffen, Heißgaschemie, Korrosionsbeständigkeit keramischer Werkstoffe und Alkalirückhaltung in der Druckkohlenstaubfeuerung**
von M. Müller (2008), 207 Seiten
ISBN: 978-3-89336-552-4

26. **Analytik von ozoninduzierten phenolischen Sekundärmetaboliten in *Nicotiana tabacum* L. cv Bel W3 mittels LC-MS**
von I. Koch (2008), III, V, 153 Seiten
ISBN 978-3-89336-553-1

27. **IEF-3 Report 2009. Grundlagenforschung für die Anwendung**
(2009), ca. 230 Seiten
ISBN: 978-3-89336-554-8

28. **Influence of Composition and Processing in the Oxidation Behavior of MCrAlY-Coatings for TBC Applications**
by J. Toscano (2009), 168 pages
ISBN: 978-3-89336-556-2

29. **Modellgestützte Analyse signifikanter Phosphorbelastungen in hessischen Oberflächengewässern aus diffusen und punktuellen Quellen**
von B. Tetzlaff (2009), 149 Seiten
ISBN: 978-3-89336-557-9

30. **Nickelreaktivlot / Oxidkeramik – Fügungen als elektrisch isolierende Dichtungskonzepte für Hochtemperatur-Brennstoffzellen-Stacks**
von S. Zügner (2009), 136 Seiten
ISBN: 978-3-89336-558-6

31. **Langzeitbeobachtung der Dosisbelastung der Bevölkerung in radioaktiv kontaminierten Gebieten Weißrusslands – Korma-Studie**
von H. Dederichs, J. Pillath, B. Heuel-Fabianek, P. Hill, R. Lennartz (2009), Getr. Pag.
ISBN: 978-3-89336-532-3

32. **Herstellung von Hochtemperatur-Brennstoffzellen über physikalische Gasphasenabscheidung**
von N. Jordán Escalona (2009), 148 Seiten
ISBN: 978-3-89336-532-3

33. **Real-time Digital Control of Plasma Position and Shape on the TEXTOR Tokamak**
by M. Mitri (2009), IV, 128 pages
ISBN: 978-3-89336-567-8

34. **Freisetzung und Einbindung von Alkalimetallverbindungen in kohlebefeuerten Kombikraftwerken**
von M. Müller (2009), 155 Seiten
ISBN: 978-3-89336-568-5

35. **Kosten von Brennstoffzellensystemen auf Massenbasis in Abhängigkeit von der Absatzmenge**
von J. Werhahn (2009), 242 Seiten
ISBN: 978-3-89336-569-2

36. **Einfluss von Reoxidationszyklen auf die Betriebsfestigkeit von anodengestützten Festoxid-Brennstoffzellen**
von M. Ettler (2009), 138 Seiten
ISBN: 978-3-89336-570-8

37. **Großflächige Plasmaabscheidung von mikrokristallinem Silizium für mikromorphe Dünnschichtsolarmodule**
von T. Kilper (2009), XVII, 154 Seiten
ISBN: 978-3-89336-572-2

38. **Generalized detailed balance theory of solar cells**
by T. Kirchartz (2009), IV, 198 pages
ISBN: 978-3-89336-573-9

39. **The Influence of the Dynamic Ergodic Divertor on the Radial Electric Field at the Tokamak TEXTOR**
von J. W. Coenen (2009), xii, 122, XXVI pages
ISBN: 978-3-89336-574-6

40. **Sicherheitstechnik im Wandel Nuklearer Systeme**
von K. Nünighoff (2009), viii, 215 Seiten
ISBN: 978-3-89336-578-4

41. **Pulvermetallurgie hochporöser NiTi-Legierungen für Implanat- und Dämpfungsanwendungen**
von M. Köhl (2009), XVII, 199 Seiten
ISBN: 978-3-89336-580-7

42. **Einfluss der Bondcoatzusammensetzung und Herstellungsparameter auf die Lebensdauer von Wärmedämmschichten bei zyklischer Temperaturbelastung**
von M. Subanovic (2009), 188, VI Seiten
ISBN: 978-3-89336-582-1

43. **Oxygen Permeation and Thermo-Chemical Stability of Oxygen Permeation Membrane Materials for the Oxyfuel Process**
by A. J. Ellett (2009), 176 pages
ISBN: 978-3-89336-581-4

44. **Korrosion von polykristallinem Aluminiumoxid (PCA) durch Metalljodidschmelzen sowie deren Benetzungseigenschaften**
von S. C. Fischer (2009), 148 Seiten
ISBN: 978-3-89336-584-5

45. **IEF-3 Report 2009. Basic Research for Applications**
(2009), 217 Seiten
ISBN: 978-3-89336-585-2

46. **Verbundvorhaben ELBASYS (Elektrische Basissysteme in einem CFK-Rumpf) - Teilprojekt: Brennstoffzellenabgase zur Tankinertisierung - Schlussbericht**
von R. Peters, J. Latz, J. Pasel, R. C. Samsun, D. Stolten
(2009), xi, 202 Seiten
ISBN: 978-3-89336-587-6

47. **Aging of ^{14}C-labeled Atrazine Residues in Soil: Location, Characterization and Biological Accessibility**
by N. D. Jablonowski (2009), IX, 104 pages
ISBN: 978-3-89336-588-3

48. **Entwicklung eines energetischen Sanierungsmodells für den europäischen Wohngebäudesektor unter dem Aspekt der Erstellung von Szenarien für Energie- und CO_2 - Einsparpotenziale bis 2030**
von P. Hansen (2009), XXII, 281 Seiten
ISBN: 978-3-89336-590-6

49. **Reduktion der Chromfreisetzung aus metallischen Interkonnektoren für Hochtemperaturbrennstofzellen durch Schutzschichtsysteme**
von R. Trebbels (2009), iii, 135 Seiten
ISBN: 978-3-89336-591-3

50. **Bruchmechanische Untersuchung von Metall / Keramik-Verbundsystemen für die Anwendung in der Hochtemperaturbrennstoffzelle**
von B. Kuhn (2009), 118 Seiten
ISBN: 978-3-89336-592-0

51. **Wasserstoff-Emissionen und ihre Auswirkungen auf den arktischen Ozonverlust**
Risikoanalyse einer globalen Wasserstoffwirtschaft
von T. Feck (2009), 180 Seiten
ISBN: 978-3-89336-593-7

52. **Development of a new Online Method for Compound Specific Measurements of Organic Aerosols**
by T. Hohaus (2009), 156 pages
ISBN: 978-3-89336-596-8

53. **Entwicklung einer FPGA basierten Ansteuerungselektronik für Justageeinheiten im Michelson Interferometer**
von H. Nöldgen (2009), 121 Seiten
ISBN: 978-3-89336-599-9

54. **Observation – and model – based study of the extratropical UT/LS**
by A. Kunz (2010), xii, 120, xii pages
ISBN: 978-3-89336-603-3

55. **Herstellung polykristalliner Szintillatoren für die Positronen-Emissions-Tomographie (PET)**
von S. K. Karim (2010), VIII, 154 Seiten
ISBN: 978-3-89336-610-1

56. **Kombination eines Gebäudekondensators mit H2-Rekombinatorelementen in Leichwasserreaktoren**
von S. Kelm (2010), vii, 119 Seiten
ISBN: 978-3-89336-611-8

57. **Plant Leaf Motion Estimation Using A 5D Affine Optical Flow Model**
by T. Schuchert (2010), X, 143 pages
ISBN: 978-3-89336-613-2

58. **Tracer-tracer relations as a tool for research on polar ozone loss**
by R. Müller (2010), 116 pages
ISBN: 978-3-89336-614-9

59. **Sorption of polycyclic aromatic hydrocarbon (PAH) to Yangtze River sediments and their components**
by J. Zhang (2010), X, 109 pages
ISBN: 978-3-89336-616-3

60. **Weltweite Innovationen bei der Entwicklung von CCS-Technologien und Möglichkeiten der Nutzung und des Recyclings von CO_2**
Studie im Auftrag des BMWi
von W. Kuckshinrichs et al. (2010), X, 139 Seiten
ISBN: 978-3-89336-617-0

61. **Herstellung und Charakterisierung von sauerstoffionenleitenden Dünnschichtmembranstrukturen**
von M. Betz (2010), XII, 112 Seiten
ISBN: 978-3-89336-618-7

62. **Politikszenarien für den Klimaschutz V – auf dem Weg zum Strukturwandel, Treibhausgas-Emissionsszenarien bis zum Jahr 2030**
hrsg. von P. Hansen, F. Chr. Matthes (2010), 276 Seiten
ISBN: 978-3-89336-619-4

63. **Charakterisierung Biogener Sekundärer Organischer Aerosole mit Statistischen Methoden**
von C. Spindler (2010), iv, 163 Seiten
ISBN: 978-3-89336-622-4

64. **Stabile Algorithmen für die Magnetotomographie an Brennstoffzellen**
von M. Wannert (2010), ix, 119 Seiten
ISBN: 978-3-89336-623-1

65. **Sauerstofftransport und Degradationsverhalten von Hochtemperaturmembranen für CO2-freie Kraftwerke**
von D. Schlehuber (2010), VII, 139 Seiten
ISBN: 978-3-89336-630-9

66. **Entwicklung und Herstellung von foliengegossenen, anodengestützten Festoxidbrennstoffzellen**
von W. Schafbauer (2010), VI, 164 Seiten
ISBN: 978-3-89336-631-6

67. **Disposal strategy of proton irradiated mercury from high power spallation sources**
by S. Chiriki (2010), xiv, 124 pages
ISBN: 978-3-89336-632-3

68. **Oxides with polyatomic anions considered as new electrolyte materials for solid oxide fuel cells (SOFCs)**
by O. H. Bin Hassan (2010), vii, 121 pages
ISBN: 978-3-89336-633-0

69. **Von der Komponente zum Stack: Entwicklung und Auslegung von HT-PEFC-Stacks der 5 kW-Klasse**
von A. Bendzulla (2010), IX, 203 Seiten
ISBN: 978-3-89336-634-7

70. **Satellitengestützte Schwerewellenmessungen in der Atmosphäre und Perspektiven einer zukünftigen ESA Mission (PREMIER)**
von S. Höfer (2010), 81 Seiten
ISBN: 978-3-89336-637-8

71. **Untersuchungen der Verhältnisse stabiler Kohlenstoffisotope in atmosphärisch relevanten VOC in Simulations- und Feldexperimenten**
von H. Spahn (2010), IV, 210 Seiten
ISBN: 978-3-89336-638-5

72. **Entwicklung und Charakterisierung eines metallischen Substrats für nanostrukturierte keramische Gastrennmembranen**
von K. Brands (2010), vii, 137 Seiten
ISBN: 978-3-89336-640-8

73. **Hybridisierung und Regelung eines mobilen Direktmethanol-Brennstoffzellen-Systems**
von J. Chr. Wilhelm (2010), 220 Seiten
ISBN: 978-3-89336-642-2

74. **Charakterisierung perowskitischer Hochtemperaturmembranen zur Sauerstoffbereitstellung für fossil gefeuerte Kraftwerksprozesse**
von S.A. Möbius (2010) III, 208 Seiten
ISBN: 978-3-89336-643-9

75. **Characterization of natural porous media by NMR and MRI techniques: High and low magnetic field studies for estimation of hydraulic properties**
by L.-R. Stingaciu (2010), 96 pages
ISBN: 978-3-89336-645-3

76. **Hydrological Characterization of a Forest Soil Using Electrical Resistivity Tomography**
by Chr. Oberdörster (2010), XXI, 151 pages
ISBN: 978-3-89336-647-7

77. **Ableitung von atomarem Sauerstoff und Wasserstoff aus Satellitendaten und deren Abhängigkeit vom solaren Zyklus**
von C. Lehmann (2010), 127 Seiten
ISBN: 978-3-89336-649-1

78. **18th World Hydrogen Energy Conference 2010 – WHEC2010 Proceedings**
Speeches and Plenary Talks
ed. by D. Stolten, B. Emonts (2010)
ISBN: 978-3-89336-658-3

78-1. **18th World Hydrogen Energy Conference 2010 – WHEC2010 Proceedings**
Parallel Sessions Book 1:
Fuel Cell Basics / Fuel Infrastructures
ed. by D. Stolten, T. Grube (2010), ca. 460 pages
ISBN: 978-3-89336-651-4

78-2. **18th World Hydrogen Energy Conference 2010 – WHEC2010 Proceedings**
Parallel Sessions Book 2:
Hydrogen Production Technologies – Part 1
ed. by D. Stolten, T. Grube (2010), ca. 400 pages
ISBN: 978-3-89336-652-1

78-3. **18th World Hydrogen Energy Conference 2010 – WHEC2010 Proceedings**
Parallel Sessions Book 3:
Hydrogen Production Technologies – Part 2
ed. by D. Stolten, T. Grube (2010), ca. 640 pages
ISBN: 978-3-89336-653-8

78-4. **18th World Hydrogen Energy Conference 2010 – WHEC2010 Proceedings**
Parallel Sessions Book 4:
Storage Systems / Policy Perspectives, Initiatives and Cooperations
ed. by D. Stolten, T. Grube (2010), ca. 500 pages
ISBN: 978-3-89336-654-5

78-5. **18th World Hydrogen Energy Conference 2010 – WHEC2010 Proceedings**
Parallel Sessions Book 5:
Stategic Analysis / Safety Issues / Existing and Emerging Markets
ed. by D. Stolten, T. Grube (2010), ca. 530 pages
ISBN: 978-3-89336-655-2

78-6. **18th World Hydrogen Energy Conference 2010 – WHEC2010 Proceedings**
Parallel Sessions Book 6:
Stationary Applications / Transportation Applications
ed. by D. Stolten, T. Grube (2010), ca. 330 pages
ISBN: 978-3-89336-656-9

78 Set (complete book series)

18th World Hydrogen Energy Conference 2010 – WHEC2010 Proceedings
ed. by D. Stolten, T. Grube, B. Emonts (2010)
ISBN: 978-3-89336-657-6

79. **Ultrafast voltex core dynamics investigated by finite-element micromagnetic simulations**
by S. Gliga (2010), vi, 144 pages
ISBN: 978-3-89336-660-6

80. **Herstellung und Charakterisierung von keramik- und metallgestützten Membranschichten für die CO_2-Abtrennung in fossilen Kraftwerken**
von F. Hauler (2010), XVIII, 178 Seiten
ISBN: 978-3-89336-662-0

81. **Experiments and numerical studies on transport of sulfadiazine in soil columns**
by M. Unold (2010), xvi, 115 pages
ISBN: 978-3-89336-663-7

82. **Prompt-Gamma-Neutronen-Aktivierungs-Analyse zur zerstörungsfreien Charakterisierung radioaktiver Abfälle**
von J.P.H. Kettler (2010), iv, 205 Seiten
ISBN: 978-3-89336-665-1

83. **Transportparameter dünner geträgerter Kathodenschichten der oxidkeramischen Brennstoffzelle**
von C. Wedershoven (2010), vi, 137 Seiten
ISBN: 978-3-89336-666-8

84. **Charakterisierung der Quellverteilung von Feinstaub und Stickoxiden in ländlichem und städtischem Gebiet**
von S. Urban (2010), vi, 211 Seiten
ISBN: 978-3-89336-669-9

85. **Optics of Nanostructured Thin-Film Silicon Solar Cells**
by C. Haase (2010), 150 pages
ISBN: 978-3-89336-671-2

86. **Entwicklung einer Isolationsschicht für einen Leichtbau-SOFC-Stack**
von R. Berhane (2010), X, 162 Seiten
ISBN: 978-3-89336-672-9

87. **Hydrogen recycling and transport in the helical divertor of TEXTOR**
by M. Clever (2010), x, 172 pages
ISBN: 978-3-89336-673-6

88. **Räumlich differenzierte Quantifizierung der N- und P-Einträge in Grundwasser und Oberflächengewässer in Nordrhein-Westfalen unter besonderer Berücksichtigung diffuser landwirtschaftlicher Quellen**
von F. Wendland et. al. (2010), xii, 216 Seiten
ISBN: 978-3-89336-674-3

89. **Oxidationskinetik innovativer Kohlenstoffmaterialien hinsichtlich schwerer Lufteinbruchstörfälle in HTR´s und Graphitentsorgung oder Aufarbeitung**
von B. Schlögl (2010), ix, 117 Seiten
ISBN: 978-3-89336-676-7

90. **Chemische Heißgasreinigung bei Biomassenvergasungsprozessen**
von M. Stemmler (2010), xv, 196 Seiten
ISBN: 978-3-89336-678-1

91. **Untersuchung und Optimierung der Serienverschaltung von Silizium-Dünnschicht-Solarmodulen**
von S. Haas (2010), ii, 202 Seiten
ISBN: 978-3-89336-680-4

92. **Non-invasive monitoring of water and solute fluxes in a cropped soil**
by S. Garré (2010), xxiv, 133 pages
ISBN: 978-3-89336-681-1

93. **Improved hydrogen sorption kinetics in wet ball milled Mg hydrides**
by L. Meng (2011), II, 119 pages
ISBN: 978-3-89336-687-3

94. **Materials for Advanced Power Engineering 2010**
ed. by J. Lecomte-Beckers, Q. Contrepois, T. Beck and B. Kuhn
(2010), 1327 pages
ISBN: 978-3-89336-685-9

95. **2D cross-hole MMR – Survey design and sensitivity analysis for cross-hole applications of the magnetometric resistivity**
by D. Fielitz (2011), xvi, 123 pages
ISBN: 978-3-89336-689-7

96. **Untersuchungen zur Oberflächenspannung von Kohleschlacken unter Vergasungsbedingungen**
von T. Melchior (2011), xvii, 270 Seiten
ISBN: 978-3-89336-690-3

97. **Secondary Organic Aerosols: Chemical Aging, Hygroscopicity, and Cloud Droplet Activation**
by A. Buchholz (2011), xiv, 134 pages
ISBN: 978-3-89336-691-0

98. **Chrom-bezogene Degradation von Festoxid-Brennstoffzellen**
von A. Neumann (2011), xvi, 218 Seiten
ISBN: 978-3-89336-692-7

99. **Amorphous and microcrystalline silicon applied in very thin tandem solar cells**
by S. Schicho (2011), XII, 190 pages
ISBN: 978-3-89336-693-4

100. **Sol-gel and nano-suspension electrolyte layers for high performance solid oxide fuel cells**
by F. Han (2011), iv, 131 pages
ISBN: 978-3-89336-694-1

101. **Impact of different vertical transport representations on simulating processes in the tropical tropopause layer (TTL)**
by F. Plöger (2011), vi, 104 pages
ISBN: 978-3-89336-695-8

102. **Untersuchung optischer Nanostrukturen für die Photovoltaik mit Nahfeldmikroskopie**
von T. Beckers (2011), xiii, 128 Seiten
ISBN: 978-3-89336-696-5

103. **Impact of contamination on hydrogenated amorphous silicon thin films & solar cells**
by J. Wördenweber (2011), XIV, 138 pages
ISBN: 978-3-89336-697-2

104. **Water and Organic Nitrate Detection in an AMS: Laboratory Characterization and Application to Ambient Measurements**
by A. Mensah (2011), XI, 111 pages
ISBN: 978-3-89336-698-9

105. **Entwicklung eines neuen Konzepts zur Steuerung der thermischen Ausdehnung von glaskeramischen Verbundwerkstoffen mit angepasster Fließfähigkeit am Beispiel der Hochtemperatur-Brennstoffzelle**
von E. Wanko (2011), xi, 134 Seiten
ISBN: 978-3-89336-705-4

106. **Tomographic reconstruction of atmospheric volumes from infrared limb-imager measurements**
by J. Ungermann (2011), xiv, 153 pages
ISBN: 978-3-89336-708-5

107. **Synthese und Identifizierung von substituierten Mg-Al-Cl Doppelhydroxidverbindungen mit Schwerpunkt IR-Spektroskopie**
von B. Hansen (2011), XII, 121 Seiten
ISBN: 978-3-89336-709-2

108. **Analysis of spatial soil moisture dynamics using wireless sensor networks**
by U. Rosenbaum (2011), xxii, 120 pages
ISBN: 978-3-89336-710-8

109. **Optimierung von APS-ZrO2-Wärmedämmschichten durch Variation der Kriechfestigkeit und der Grenzflächenrauhigkeit**
von M. E. Schweda (2011), 168 Seiten
ISBN: 978-3-89336-711-5

110. **Sorption of a branched nonylphenol isomer and perfluorooctanoic acid on geosorbents and carbon nanotubes**
by C. Li (2011), X, 102 pages
ISBN: 978-3-89336-716-0

111. **Electron Transport in the Plasma Edge with Rotating Resonant Magnetic Perturbations at the TEXTOR Tokamak**
by H. Stoschus (2011), iv, 113 pages
ISBN: 978-3-89336-718-4

112. **Diffusion and Flow Investigations in Natural Porous Media by Nuclear Magnetic Resonance**
by N. Spindler (2011), viii, 144 pages
ISBN: 978-3-89336-719-1

113. **Entwicklung und Erprobung des Hygrometer for Atmospheric Investigations**
von T. Klostermann (2011), IV, 118 Seiten
ISBN: 978-3-89336-723-8

114. **Application of functional gene arrays for monitoring influences of plant/seasons on bacterial functions and community structures in constructed wetlands (Bitterfeld, Germany)**
by J. Ning (2011), xiv, 157 pages
ISBN: 978-3-89336-724-5

115. **Wasseraustrag aus den Kathodenkanälen von Direkt-Methanol-Brennstoffzellen**
von A. Schröder (2011), VII, 228 Seiten
ISBN: 978-3-89336-727-6

116. **CITYZEN Climate Impact Studies**
ed. by M. Schultz (2011), 45 pages
ISBN: 978-3-89336-729-0

117. **Software Tools zum interoperablen Austausch und zur Visualisierung von Geodatensätzen über das Internet**
von M. Schultz, M. Decker, S. Lührs (2011), iv, 156 Seiten
ISBN: 978-3-89336-730-6

118. **Optimierung eines Leichtbaudesigns für ein SOFC-Brennstoffzellenstack**
von T. Nguyen-Xuan (2011), III, 154 Seiten
ISBN: 978-3-89336-732-0

119. **Institute of Energy and Climate Research IEK-6:**
Nuclear Waste Management & Reactor Safety Report 2009/2010
Material Science for Nuclear Waste Management
ed. by M. Klinkenberg, S. Neumeier, D. Bosbach (2011), 242 pages
ISBN: 978-3-89336-735-1

120. **Fate of the Antibiotic Sulfadiazine in Yangtze River Sediments: Transformation, Sorption and Transport**
by N. Meng (2011), XII, 111 pages
ISBN: 978-3-89336-736-8

121. **Thermodynamische Eigenschaften gasförmiger und kondensierter Verbindungen für Hochtemperaturanwendungen**
von T. Markus (2011), II, 131 Seiten
ISBN: 978-3-89336-728-3

122. **Ein neues LIF-Instrument für flugzeug- und bodengebundene Messungen von OH- und HO_2-Radikalen in der Troposphäre**
von S. Broch (2011), IV, 160 Seiten
ISBN: 978-3-89336-742-9

123. **Processes in the Yangtze River System - Experiences and Perspectives**
Workshop-Proceedings
ed. by S. Küpper, G. Subklew, R.-D. Wilken (2011), 83 pages
ISBN: 978-3-89336-744-3

124. **Thermo-Mechanical Properties of Mixed Ion-Electron Conducting Membrane Materials**
by B. Huang (2011), 130 pages
ISBN: 978-3-89336-746-7

125. **Growth, Etching, and Stability of Sputtered ZnO:Al for Thin-Film Silicon Solar Cells**
by J. I. Owen (2011), xv, 192 pages
ISBN: 978-3-89336-749-8

126. **Entwicklung geträgerter $Ba_{0,5}Sr_{0,5}Co_{0,8}Fe_{0,2}O_{3-\delta}$ Sauerstoff-Permeationsmembranen**
von F. Schulze-Küppers (2011), ii, 119 Seiten
ISBN: 978-3-89336-752-8

127. **Development of the 2-Component-Injection Moulding for Metal Powders**
by A. P. Cysne Barbosa (2011), XIV, 150 pages
ISBN: 978-3-89336-753-5

128. **Performance of Tungsten-Based Materials and Components under ITER and DEMO Relevant Steady-State Thermal Loads**
by G. H. Ritz (2011), X, 128 pages
ISBN: 978-3-89336-755-9

129. **Experimentelle Bestimmung und numerische Simulation von Viskositäten in Schlackesystemen unter Vergasungsbedingungen**
von T. Nentwig (2011), 156 Seiten
ISBN: 978-3-89336-756-6

130. **Development of Thin Film Oxygen Transport Membranes on Metallic Supports**
by Y. Xing (2012), iv, 117 pages
ISBN: 978-3-89336-765-8

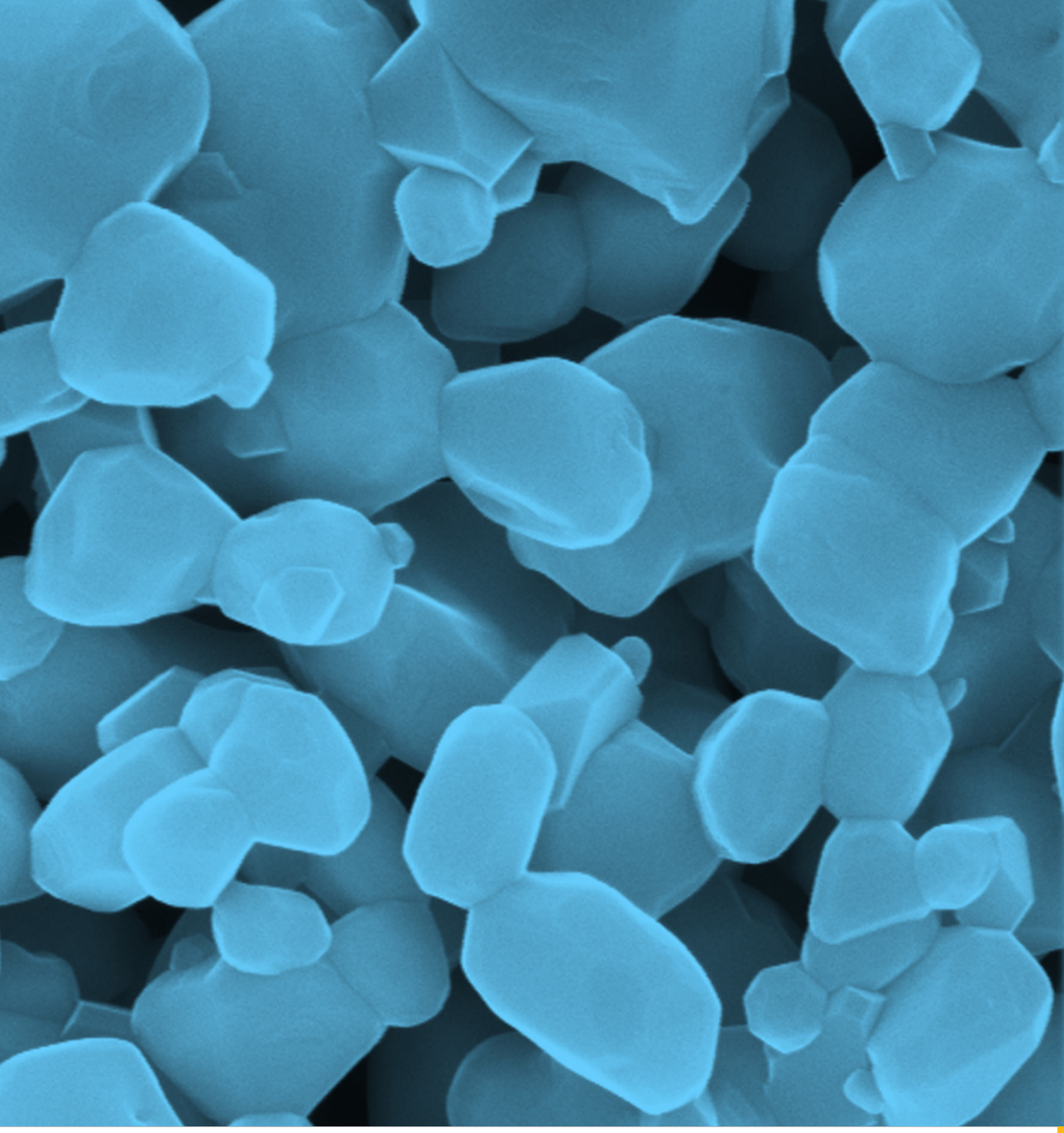

Energie & Umwelt / Energy & Environment
Band / Volume 130
ISBN 978-3-89336-765-8

JÜLICH
FORSCHUNGSZENTRUM